UCL DEPARTMENT OF MATHEMATICS

Spin-down in the absence of reflected waves

Kamran Pentland

September 2019

Dissertation submitted in partial fulfillment of the MSc Mathematical
Modelling, UCL.

Supervised by:

Professor Edward Johnson, Department of Mathematics, UCL.

Acknowledgements

Firstly I would like to thank my supervisor, Professor Johnson, for introducing me to the exciting world of geophysical fluid dynamics and for providing extremely helpful guidance throughout this project. I would also like to thank my family and friends who have helped me throughout the year and for reminding me that it is good to take a break from studying now and then. Finally I would like to thank both of my parents for the financial and emotional support they have provided me for the past 24 years, without which I would certainly not be where I am today.

Abstract

The linear spin-down of a homogeneous incompressible viscous fluid filling closed containers in the half cone, half cylinder and rectangular geometries with sloping topographies are studied. The half cone spin-down dynamics are motivated by the three-dimensional simulations and experimental results published in [22]. We reproduce, confirm and discuss some of the results from [22], deriving the topographic wave equation in order to set up more simple initial boundary value problems for the linear spin-down. The resulting two-dimensional eigenvalue and time-dependent problems are solved using numerical spectral methods in MATLAB [21][29]. Numerical results accurately reproduce the transient fluid dynamics detailed in [22] via simulations of the mass transport, vertical vorticity, vertical velocity and energy decay. It is found that, regardless of the container geometry, if the depth goes to zero anywhere, the system energy becomes unbounded and no discrete set of oscillatory modes can be found, contrary to the reasons given in [22]. Waves reflected in the inviscid problems no longer do so once viscosity is included and it is found that spin-down also occurs 3-4 times faster in the rectangular and half cone geometries when the slope of the topography is doubled. All results are determined using minimal computational resources and are easily reproduced for the linear spin-up case.

Contents

List of Figures

List of Tables

Chapter 1

Introduction

This project is divided into three interlinked chapters to solve the linear spin-down problem in a rotating half cone (first detailed by Li et al. in [22]) and a rectangular container with sloping bottom. In Chapter 1 we provide the motivation and aims for the project. Chapter 2 illustrates the inviscid spin-down problem in the half cone geometry and details the key methods required to solve it, as well as the other problems in later chapters. Chapter 3 delves into the case of a rectangular container with linearly sloping bottom and discusses how the dynamics are closely linked with that of the half cone. Finally in Chapter 4 we deal with the full viscous problem in the half cone and discuss the conclusions of this work in Chapter 5.

1.1 Motivation and Aims

A spin-down problem in rotating fluid dynamics is one concerned with understanding the transient behaviour of a fluid within a closed container following a small but permanent decrease in the angular velocity of the container $\mathbf{\Omega_0}$, to $\mathbf{\Omega_1} := (1-\epsilon)\mathbf{\Omega_0}$ for some $0 < \epsilon \ll 1$. The new angular velocity is maintained whilst the fluid undergoes some form of unknown transient behaviour and the process ends once the fluid reverts back to rotating uniformly at the new velocity $\mathbf{\Omega_1}$. Similarly defined are spin-up problems where the same dynamics are considered, however the rotation rate is increased from $\mathbf{\Omega_0}$ to some $\mathbf{\Omega_1} := (1+\epsilon)\mathbf{\Omega_0}$ [22].

The Rossby number, $Ro = (\Omega_1 - \Omega_0)/\Omega_1$, is an essential parameter that measures the relative change in rotation rate for a system [9]. A positive $Ro > 0$ yields spin-up and negative $Ro < 0$ yields spin-down. Small changes in angular velocity ($|Ro| \leq 0.1$) are named 'linear' spin-up/down problems and are well understood in certain geometries. Larger changes ($|Ro| \to 1$) are referred to as 'nonlinear' spin-up/down problems. Nonlinear spin-up involves studying the dynamics of a system spun-up from rest whilst nonlinear spin-down is defined similarly, corresponding to spin-down to rest. These are much more difficult to analyse using analytical methods and so numerical methods are often employed to understand the dynamics.

Understanding how a rotating fluid evolves following an adjustment in its rotation rate represents an important process that arises frequently in astrophysical, geophysical and industrial systems. The transient behaviour between the initial spin-down and final rigid body rotation is important to understand as it involves the time-dependent motion of a diffusive (if viscosity is included) and dispersive mechanical system [14].

This type of problem is by no means new in rotating fluid dynamics and to describe the basic concepts we discuss a famous problem involving a similar process. During the early 20th century, Einstein discussed the solution to the *Tea Leaf Paradox*, in [38], where tea leaves 'spun-up' from rest collect and settle centrally at the bottom of a cup instead of being forced to the edges by centrifugal forces (see Figure 1.1). Once the spoon is removed, the fluid slows down at the lower and lateral boundaries due to viscous effects and a pressure gradient is created, sucking flow inwards at the bottom, thus pulling the leaves into the centre. Once there, centripetal forces dominate the inertial forces and the flow is pulled up to the surface and pushed radially outward to satisfy continuity. However the tea leaves are too heavy to lift and therefore settle at the bottom of the cup. Whilst not strictly demonstrating spin-up, as the container is fixed and the liquid is spun as opposed to the container rotating, it provides a simple example of the formation of boundary layers (strictly Ekman layers) and the damping of fluid flow that we will observe in later chapters.

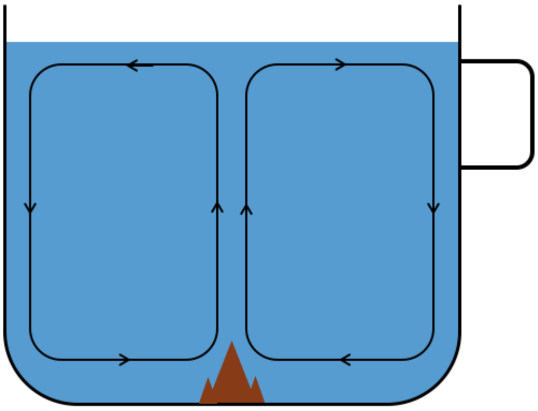

Figure 1.1: Schematic of mass transport streamlines in the tea cup.

To provide some motivation for the study of this motion we can discuss a few practical applications. In 1948 Bondi and Lyttleton [4] discussed the astrophysical impact of a spin-down process in their paper on secular retardation within the Earth's core. The Earth's core can be well approximated as a spherical geometry with a rigid lid (i.e. the Earth's crust) that is rotated at a single angular velocity. They discuss the spin-down effect caused by tidal friction, a lunar phenomenon that slows the rigid crust whilst the molten core rotates at the original angular velocity. These viscous effects are modelled in order to help determine the composition and dynamics of the molten fluid within the inaccessible interior of the Earth.

One application of the process in a geophysical context was described by Anderson and Gill in their paper, [2], on coastal upwelling in stratified oceans and by Pedlosky and

Greenspan, [25], in the wind-driven open ocean. Anderson and Gill examine the effect of a sudden wind stress applied to an initially stratified, motionless ocean. This is an excellent example of a non-linear spin-up from rest process and they go on to discuss the impact this has on boundary layer formation on western coastlines, planetary waves and coastal upwelling. Amberg and Ungarish also develop an important application in physical chemistry in their paper on the centrifugal separation of a fluid-particle mixture [1].

The classical work in this field was carried out in 1963 by Greenspan and Howard when they published their fundamental analysis, [14], that discusses the linear spin-up in general axisymmetric containers in the small Rossby number limit ($Ro \to 0$). By linearising the Navier-Stokes equations they determined[1], for $E \ll 1$, the distinct time taken for homogeneous incompressible fluids to reach spin-up, $E^{-1/2}\Omega_1^{-1}$. Small Ekman numbers imply the existence of very thin regions of fluid, where tangential velocity is adjusted to the value at the wall through viscosity, called *boundary layers* [13]. In this problem Greenspan and Howard found that spin-up generates Ekman layers at the horizontal boundaries, which have outward radial flow caused by centrifugal forces, see Figure 1.2. The interior fluid is essentially inviscid and is therefore sucked into the Ekman layers to be spun-up to the final angular velocity before being pushed back into the interior of the container.

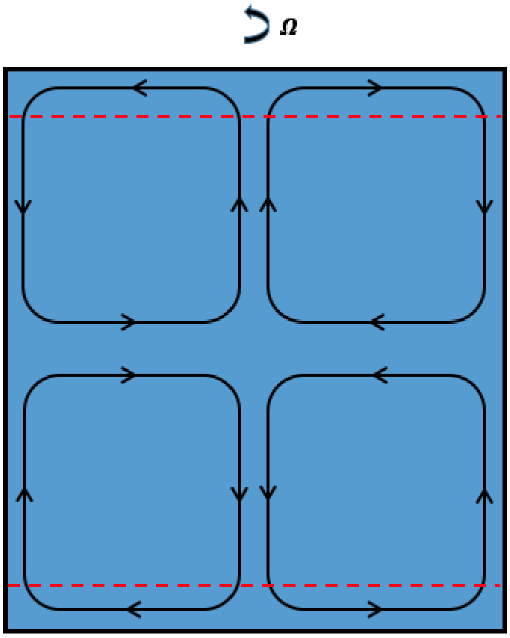

Figure 1.2: Meridional plane view of mass transport streamlines (solid lines) and the two horizontal Ekman layers in an axisymmetric container (dashed lines) - reproduced from [9].

In [36], Wedemeyer considered the other end of the scale at $Ro = 1$. This situation corresponds to a spin-up from rest process where dynamics become much more unstable. As numerical methods were being developed during the 1970s, the Navier-Stokes equations could now be resolved numerically and the results of the previous decade were confirmed and modified in papers presented by Weidman [37] and Watkins and Hussey

---

[1] $E = \frac{\nu}{\Omega_1 L^2}$ is defined as the *Ekman Number*, the ratio of viscous to Coriolis forces in a given fluid where ν is the kinematic viscosity, Ω_1 the final angular velocity and L the typical length scale of the container.

[35]. Work has been carried out using series expansions in Ro to try and link the linear and nonlinear theory however it has yet to produce the results of Greenspan or Wedemyer in the limit of $Ro \to 0$ and $Ro \to 1$ respectively [24].

Geometry	**Authors**	**Reference**
Axisymmetric		
Cylindrical	Greenspan and Howard (1963) Wedemeyer (1964) Weidman (1975) Watkins and Hussey (1977) van de Konijnenberg, van Heijst (1995)	[14] [36] [37] [35] [32]
Spheroids	Bryan (1889) Bondi and Lyttleton (1948) Zhang et al. (2000) Zhang, Liao and Earnshaw (2003)	[6] [4] [39] [40]
Non-Axisymmetric		
Rectangular	van Heijst, Davies and Davis (1990) van de Konijnenberg et al. (1993) van Heijst, Maas and Williams (1993) van de Konijnenberg, van Heijst (1996) van Heijst (1989)	[34] [30] [16] [31] [15]
Sliced Cylinder	Pedlosky and Greenspan (1966)	[25]
Annulus	van Heijst (1989)	[15]
Half Circle	van Heijst (1989)	[15]
Half Cone	Li et al. (2012)	[22]
Topography and/or Obstructions	van Heijst (1989) van de Konijnenberg et al. (1996) Burmann and Noir (2018)	[15] [33] [7]
Reviews	Benton and Clark (1974) Duck and Foster (2001) Park and Hyun (2007)	[3] [9] [24]

Table 1.1: A brief summary of previous work carried out on spin-up/down problems.

Whereas these early studies focus solely on dynamics in axisymmetric containers, more recent study has been focused on developing theory for more complex geometries as well as containers with topography and obstructions. Non-axisymmetric containers do not exhibit symmetry about the rotation axis and usually have either a non-symmetric cross section, for example, a pentagonal section, or non-axisymmetric depth variations. A brief summary of some of the problems that have been studied so far is provided in Table 1.1. Efforts to tackle more realistic scenarios have also been considered by including the effects of stratification, free surfaces and compressibility (see review papers in Table 1.1). The rectangular case will be of particular interest to this study as it will contain strikingly similar dynamics to those found in the half cone (see Chapter 3).

The focus of this project will be to reproduce a portion of the analysis carried out by Li et al. in their paper: *Spin-up and spin-down in a half cone: A pathological situation or not?* [22]. Their work details the physical evolution of an incompressible viscous fluid in a closed rapidly rotating half cone following both linear and non-linear spin-up and spin-down. We focus purely on the linear spin-down case however the spin-up case can easily be determined by altering the initial condition in Section 2.7.

Their goal was to determine whether or not the dynamics of the half cone system are fundamentally different from the linear theory of spin-up/down in general axisymmetric containers, detailed by Greenspan and Howard [14]. The aim was to understand how the initial vorticity generated from the spin-up/down propagates and over what time scale it is then damped away, returning the system to rigid body rotation. They argue that the reason no discrete set of oscillatory modes can exist is due to the presence of the vertex at the base of the half cone.

In order to generate their results they conducted both numerical simulations and laboratory experiments. The numerical simulations were carried out solving the fully non-linear Navier-Stokes equations with a three dimensional finite element code on the Shanghai supercomputer. These simulations were then compared with results obtained from a physical setup of the experiment that used a 3D printed half cone, a Particle Image Velocimetry system and a camera mounted above the rotating plate in order to capture images of the horizontal light sheets generated by the laser at different vertical heights (see Figure 1.3).

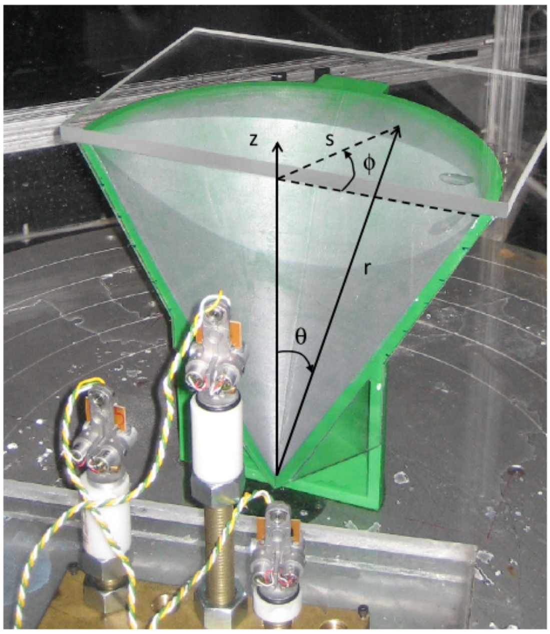

Figure 1.3: The half cone experimental set up used in [22, Fig.1].

The authors discovered that the dynamics are dominated by the topographic effects of the half cone and the initial fluid vortex generated propagates into the 'westward' corner (see Figure 2.1b) of the cone for both spin-up and down problems. Following this they state that viscous boundary layer effects on the cone bottom dominate the dissipation of vorticity and the system returns to a state of rigid body rotation over time scale $\mathcal{O}(E^{-1/2})$. They concluded that the "fluid dynamics...is not fundamentally different from that in a container with small topography" [22].

This specific setup is important as it sits apart from other geometries that have been studied and looked at in much detail. The non-axisymmetric structure of the container implies there are no closed geostrophic contours[2] which means that the linear theory detailed in [13] and [14] cannot be used to solve the problem. This motivates the search for more simple, alternative methods to determine the behaviour of the transient fluid flow.

Instead of computing full three-dimensional simulations, we reproduce and confirm the results of the linear spin-down problem in a half cone found by Li et al. using two-dimensional methods. We also argue that the reason that no discrete set of normal modes can exist has nothing to do with the half cone geometry of the container and hence its vertex. Instead we argue that because the depth of the container (half cone or rectangular) goes to zero on some part of the boundary, the energy is no longer bounded, hence no discrete modes can be identified. We also look for anything that may be different to the vertical vorticity evolution and energy decay results identified in [22]. We do this by deriving and then solving the topographic wave equation, a well studied equation in oceanographic settings that requires the container be subject to the *shallow water assumption*. This approach allows us to use extensively studied theory and reduce the computational requirements of the problem drastically.

First we consider spin-down in the inviscid half cone and detail the analytical and numerical methodology required to solve the initial boundary value problems posed throughout this study. We also observe the reflected waves referred to in this paper's title and discuss how their absence arises as a result of the inclusion of viscosity. In Chapter 3 we consider spin-down in a rectangular container with linearly sloping bottom to determine whether the transient dynamics are drastically affected by the geometry of the container or its topography and to identify similarities with the half cone case. In Chapter 4 we use all of this information to calculate the streamline patterns, vertical vorticity, vertical velocity and energy decay relations for the viscous spin-down in a half cone whilst comparing and contrasting the results with those presented in [22]. In Chapter 5 we summarise the benefits and limitations of this more simplified method for analysing linear spin-up/down in a variety of topographic containers.

---

[2] A closed curve C is a geostrophic contour if it has constant total height $z = f + g$ where $z = f(x, y)$ and $z = -g(x, y)$ are the top and bottoms of the container respectively [25].

Chapter 2

Inviscid Fluid Spin-Down in a Half Cone

In this chapter we will set up the spin-down problem as described by Li et al. and make certain assumptions about the fluid flow in order to derive the two-dimensional topographic wave equation. We will detail how to transform the partial differential equation into a generalised eigenvalue problem and then solve it using a spectral method in MATLAB. Following this, we analyse the normal modes of the system describing their behaviour over time. Using orthogonality arguments we are able to incorporate the initial condition that is required to generate spin-down motion and hence fully solve the problem using a superposition of the modes. We then discuss these results and how they compare to a directly integrated time-dependent solution.

2.1 Problem Formulation

Consider an inviscid, incompressible fluid completely filling a closed container of volume $\bar{V}$ in the shape of a half cone with a rigid lid (removing free surface effects). A half cone is defined as one half of a right-circular cone, with apex down, centred on the z-axis having been sliced down an axis of symmetry. A depiction with typical horizontal length and vertical depth scales L and D is plotted in three-dimensional Euclidean space in Figure 2.1a. It is assumed that the fluid is both homogeneous (having the same proportions of its components throughout) and barotropic (density being a function of pressure only, ignoring temperature effects).

The two-dimensional cross section of the half cone is given in Figure 2.1b along with oceanographic cardinal directions to aid the description of fluid movement in later sections. Naturally it makes sense to introduce the cylindrical coordinate system (r, θ, z) in order to simplify calculations required later. Let $x = r\cos(\theta)$, $y = r\sin(\theta)$ and $z = z$ such that $r = \sqrt{x^2 + y^2}$ is the usual Euclidean distance from the origin, $\theta = \arctan(y/x)$ the angle

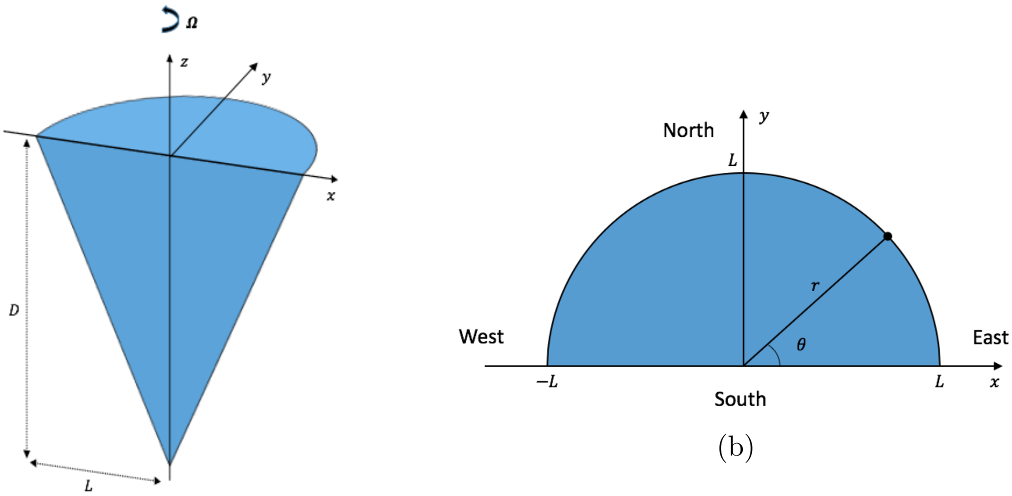

(a)

(b)

Figure 2.1: (a) The three-dimensional view displaying the flat face of the half cone and direction of angular rotation, $\boldsymbol{\Omega}$, above. (b) The horizontal cross-section labelled in both coordinate systems and the four cardinal directions.

between the radial line and the positive x-axis and z the vertical height. This allows us to explicitly define the half cone as

$$r : 0 \leq r \leq L \qquad \theta : 0 \leq \theta \leq \pi \qquad z : -D \leq \; z = D\Big(\frac{r}{L} - 1\Big) \; \leq 0. \tag{2.1.1}$$

This is what we can see in Figure 2.1a. Suppose the container is rotating uniformly counter-clockwise at constant angular velocity $\Omega_0 \hat{\mathbf{z}}$ at time $t \leq 0$ but is instantaneously decreased at $t = 0^+$ to $\Omega_1 \hat{\mathbf{z}}$ where the Rossby number $Ro = (\Omega_1 - \Omega_0)/\Omega_1$ is small and negative. We now diverge from the method presented in [22] where Li et al. opt to solve the governing three-dimensional nonlinear Navier-Stokes equations (2.1.2)[1], with boundary and initial conditions, numerically. In this system $\boldsymbol{u}(x, y, z, t)$ is the velocity vector, Ω_1 the magnitude of the final angular velocity, ρ the constant density, p the reduced pressure and ν the kinematic viscosity of the fluid. With no general analytic solution and numerical solutions being very computationally expensive in three-dimensional space, we approach the problem from another direction.

---

[1] The operator $\frac{D}{Dt}$ denotes the usual material derivative $\frac{D}{Dt} = \frac{\partial}{\partial t} + \mathbf{u} \cdot \nabla$.

$$\frac{D\boldsymbol{u}}{Dt} + (\Omega_1 \hat{\boldsymbol{z}} \times \boldsymbol{u}) = -\frac{1}{\rho}\nabla p + \nu \nabla^2 \boldsymbol{u} \tag{2.1.2a}$$

$$\nabla \cdot \boldsymbol{u} = 0 \tag{2.1.2b}$$

In order to simplify the problem, we make the *shallow water assumption* [20], more specifically, the assumption that the ratio of depth to horizontal length of the container is very small such that

$$\delta := \frac{D}{L} \ll 1. \tag{2.1.3}$$

After conducting the non-dimensional analysis, the vertical pressure derivative balances the gravitational force in the vertical momentum equation above - this is also known as *hydrostatic pressure balance*. It means that the vertical velocity component can be omitted from (2.1.2) by integrating vertically and considering a two-dimensional depth-independent flow. However we must note that the vertical velocity component is *not* necessarily zero because of the spatially changing topography. In summary, this implies that we can consider a 'flattened' half cone that has a wide lid and very shallow depth as shown in Figure 2.2. In doing so, we avoid the need to solve the Navier-Stokes equations and instead are able to use the *rotating Shallow Water Equations* (abbreviated as rSWE henceforth) which have the key property that vertical velocity scale is much smaller than the horizontal velocity scale. Now we state the rSWE and derive a result involving a mass transport streamfunction for the problem.

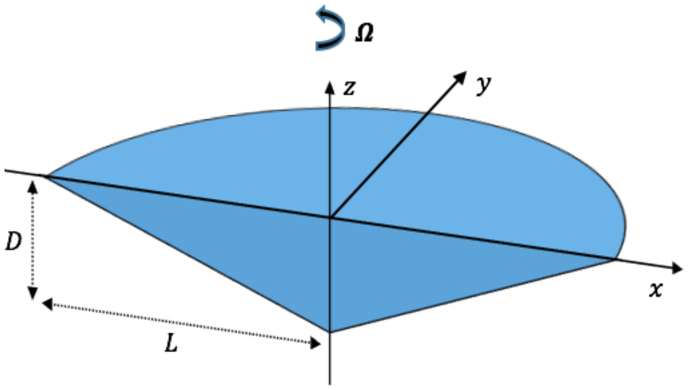

Figure 2.2: The shallow half cone is subject to fluid flow described by the rSWE (2.2.1).

2.2 Derivation of the Topographic Wave Equation

We now derive the governing equation used in the forthcoming analysis, the *Topographic Wave Equation*. This equation is usually solved in ocean basins or lake domain settings but is also perfectly applicable to the finite depth containers we are studying. In order to derive this equation we utilise an important property of the shallow water equations, that is, that potential vorticity is always conserved. In the Cartesian coordinate system we immediately write down the rSWE (2.2.1)[2] that govern fluid flow within the shallow half cone.

$$\frac{Du}{Dt} - fv = -g\frac{\partial h}{\partial x}, \tag{2.2.1a}$$

$$\frac{Dv}{Dt} + fu = -g\frac{\partial h}{\partial y}, \tag{2.2.1b}$$

$$\frac{DH}{Dt} + H\nabla \cdot \mathbf{u} = 0. \tag{2.2.1c}$$

The horizontal velocity vector is now denoted by $\mathbf{u} = (u, v)$, a function of both time and space, $h(x, y, t)$ represents the free surface whilst f and g define the Coriolis parameter and gravitational constant respectively. The $H(x, y, t) = h(x, y, t) - h_b(x, y)$ term is the time-dependent local depth with fixed bottom basin profile $z = h_b(x, y)$. Note that the Coriolis parameter takes a fixed value here, ensuring the fluid is evolving on what is called the f-plane, however in Chapter 3 we will need to allow f to vary in space (specifically the y-direction), working in what is known as the β-plane.

Assuming nonlinear effects are negligible[3], we linearise the rSWE in order to obtain the *linearised Shallow Water Equations* (henceforth lSWE):

$$\frac{\partial u}{\partial t} - fv = -g\frac{\partial h}{\partial x}, \tag{2.2.2a}$$

$$\frac{\partial v}{\partial t} + fu = -g\frac{\partial h}{\partial y}, \tag{2.2.2b}$$

$$\frac{\partial H}{\partial t} + \nabla \cdot (\mathbf{u}H_0) = 0. \tag{2.2.2c}$$

Where $H_0 = -h_b(x, y)$ is the undisturbed depth profile of the container (usually this would be the ocean basin or lake topography). The rigid lid assumption of the half cone container implies that the local depth H is no longer time-dependent so the first term of the continuity equation (2.2.2c) vanishes and we observe that the divergence of the

---

[2] A formal derivation of the rSWE is omitted here but may be found in both [11, p. 107-109] (starting from the hydrostatic approximation) and [20] (starting from the *rotating Euler Equations*).

[3] In other words, convective acceleration is ignored and free surface displacements are taken to be small.

volume transport $\boldsymbol{u}H_0$ equals zero (2.2.3). This important relation allows us to determine a streamfunction for the problem.

$$\underbrace{\frac{\partial H}{\partial t}}_{=0} + \nabla \cdot (\mathbf{u}H_0) = 0 \quad \Rightarrow \quad \nabla \cdot (\mathbf{u}H_0) = 0. \tag{2.2.3}$$

More specifically we introduce the depth-integrated mass transport, or flux, streamfunction $\psi(x, y, t)$ that must obey the horizontal velocity relations[4]

$$uH_0 = -\psi_y \quad \text{and} \quad vH_0 = \psi_x \quad \Rightarrow \quad u = -\frac{1}{H_0}\psi_y \quad \text{and} \quad v = \frac{1}{H_0}\psi_x. \tag{2.2.4}$$

We shall show later how the mass transport streamlines, given by the lines of constant ψ, define closed contours in basins of varying geometry/topography[5].

Rotating fluids on any scale will always exhibit some form of circulation or *vorticity* and hence we need to define what this movement is. The *vorticity*, $\boldsymbol{\zeta}$, is the local spinning motion of a fluid at a given point and time. It is quantified in three dimensions as the curl of the fluid velocity, $\nabla \times \boldsymbol{u}$, however we are working in two spatial dimensions (i.e. $\boldsymbol{u} = \boldsymbol{u}(x, y, t)$) hence vorticity is perpendicular to the flow such that

$$\boldsymbol{\zeta}(x, y, t) = (\frac{\partial v}{\partial x} - \frac{\partial u}{\partial y})\hat{\boldsymbol{z}}. \tag{2.2.5}$$

Using this definition of relative vorticity (relative with respect to the rotating frame) we can write it in terms of the streamfunction ψ as

$$\zeta = \frac{\partial v}{\partial x} - \frac{\partial u}{\partial y} = \frac{\partial}{\partial x}\Big(\frac{1}{H_0}\psi_x\Big) + \frac{\partial}{\partial y}\Big(\frac{1}{H_0}\psi_y\Big) = \nabla \cdot \Big(\frac{\nabla \psi}{H_0}\Big). \tag{2.2.6}$$

Now we utilise the fact that potential vorticity is conserved in shallow water systems, as proved in [26] by Rossby, to write

$$\frac{D}{Dt}\Big(\frac{\zeta + f}{H_0}\Big) = 0. \tag{2.2.7}$$

Expanding (2.2.7) and neglecting nonlinear terms we obtain the following argument

---

[4] Note that ψ_x and ψ_y denote partial differentiation with respect to x and y respectively.

[5] The units of ψ are mass per unit time (kg/s^{-1}).

$$0 = \Big(\frac{\partial}{\partial t} + \mathbf{u}\cdot\nabla\Big)\Big(\frac{\zeta+f}{H_0}\Big) = \frac{1}{H_0}\frac{\partial\zeta}{\partial t} + (\mathbf{u}\cdot\nabla)\frac{f}{H_0} \tag{2.2.8}$$

$$= \frac{\partial\zeta}{\partial t} + H_0\mathbf{u}\cdot\nabla\Big(\frac{f}{H_0}\Big) \tag{2.2.9}$$

$$= \frac{\partial\zeta}{\partial t} + (\hat{\mathbf{z}}\times\nabla\psi)\cdot\nabla\Big(\frac{f}{H_0}\Big). \tag{2.2.10}$$

Noting that the volume transport can be written alternatively as

$$H_0\mathbf{u} = \begin{pmatrix} H_0 u \\ H_0 v \end{pmatrix} = \begin{pmatrix} -\psi_y \\ \psi_x \end{pmatrix} = \hat{\mathbf{z}}\times\nabla\psi. \tag{2.2.11}$$

By substituting (2.2.6) for the potential vorticity in (2.2.10) we obtain

$$\frac{\partial}{\partial t}\nabla\cdot\Big(\frac{\nabla\psi}{H_0}\Big) + (\hat{\mathbf{z}}\times\nabla\psi)\cdot\nabla\Big(\frac{f}{H_0}\Big) = 0, \tag{2.2.12}$$

and finally, permuting terms in the cross product, we obtain the *Topographic Wave Equation* (henceforth TWE)

$$\frac{\partial}{\partial t}\nabla\cdot\Big(\frac{\nabla\psi}{H_0}\Big) + \hat{\mathbf{z}}\cdot(\nabla\psi\times\nabla\frac{f}{H_0}) = 0. \tag{2.2.13}$$

This free wave equation will allow us to determine mass transport streamfunctions in different two-dimensional domains with various topographies. The first term is just the rate of change of potential vorticity and if we consider the steady (time-independent) equation then (2.2.13) becomes

$$\nabla\psi\times\nabla\frac{f}{H_0} = 0. \tag{2.2.14}$$

This equation implies that the mass transport streamlines ψ are parallel to lines of constant f/H_0, named *isotrophes*, and therefore if at some time, in (2.2.13), they are not parallel, then a *Rossby wave* must develop [18]. These Rossby waves are a subset of the *inertial waves* we are looking for. Two other interesting cases of (2.2.13) to consider are:

- $f = 0 \;\Rightarrow \partial_t\nabla\cdot(\nabla\psi/H_0) = 0 \;\Rightarrow\; \psi = 0$ as it must attain its maximum/minimum on the boundary (i.e. trivial solution only, no Rossby waves).

- $f \neq 0$ but $\nabla(f/H_0) = 0 \ \Rightarrow$ depth is constant, which in turn yields only trivial solutions again, *unless* we work in the β-plane instead of the f-plane, in which case we can obtain non-trivial solutions (see Chapter 3).

Following the work of Stocker and Hutter, [27], let us summarise the assumptions we have made in the model so far. It follows that:

1. The process must be adiabatic[6].
2. The fluid must be homogeneous and barotropic (i.e. of constant density).
3. The shallow water assumption (2.1.3) must hold.
4. The pressure is hydrostatic (in the shallow water assumptions).

Notice that we have still made no assumptions regarding the depth profile H_0 and the magnitude of the rotation rate. The TWE will be used to solve an initial value problem on the semi-circular domain given in Figure 2.1b and we must also impose a zero-flux condition on the boundary of the semicircle V such that

$$\psi = \text{constant} \quad \text{on} \quad \partial V. \tag{2.2.15}$$

The boundary ∂V is simply connected so we may choose this constant arbitrarily as zero without loss of generality. The problem, without an initial condition for the moment, can then be written in full as

$$\frac{\partial}{\partial t}\nabla \cdot \left(\frac{\nabla\psi}{H_0}\right) + \hat{\mathbf{z}} \cdot (\nabla\psi \times \nabla\frac{f}{H_0}) = 0 \quad \text{in} \quad V, \tag{2.2.16a}$$

$$\psi = 0 \quad \text{on} \quad \partial V. \tag{2.2.16b}$$

So far we have managed to reduce the rSWE, using a simple argument with potential vorticity, to the TWE with a homogeneous Dirichlet boundary condition. In order to simplify the problem further and learn more about this equation we can now non-dimensionalise the equation appropriately.

2.3 Scale Invariance

To recap, $\psi = \psi(x, y, t)$ is the mass flux streamfunction, $\hat{\mathbf{z}}$ the vertical unit vector, f the Coriolis parameter and $H_0(x, y)$ the depth profile. Problem (2.2.16) is currently in

---

[6] An *adiabatic* process is one where no heat or mass is transferred between the thermodynamic system and its environment.

dimensional form and so we wish to scale out the horizontal length and vertical depth scales as well as the Coriolis frequency f. Let us define the dimensionless variables by scaling x and y by the horizontal length L, the depth profile H_0 by depth D, time t with f^{-1} and the streamfunction with some arbitrary constant ψ_0. The scaled variables are defined as

$$\psi = \psi_0 \bar{\psi}, \quad x = L\bar{x}, \quad y = L\bar{y}, \quad t = f^{-1}\bar{t}, \quad \text{and} \quad H_0 = D\bar{H}_0.$$

After substitution and some cancellation the only change to (2.2.16) is that f has been scaled out of the problem. Dropping the bars above each non-dimensional term we write

$$\frac{\partial}{\partial t}\nabla \cdot \left(\frac{\nabla\psi}{H_0}\right) + \hat{\mathbf{z}} \cdot (\nabla\psi \times \nabla\frac{1}{H_0}) = 0 \quad \text{in} \quad V, \tag{2.3.1a}$$

$$\psi = 0 \quad \text{on} \quad \partial V. \tag{2.3.1b}$$

This leads to a curious property that the boundary value problem is *scale invariant*. This means that the waveforms of the streamfunction ψ are the same regardless of the size of the container. The property arises as a result of the rigid lid assumption within the *rSWE* [27]. To demonstrate this, take the lSWE and perform the following operations

$$\frac{\partial}{\partial t}(2.2.2a) + f(2.2.2b) \quad \Rightarrow \quad \left(\frac{\partial^2}{\partial t^2} + f^2\right)u = -g\frac{\partial^2 h}{\partial t \partial x} - gf\frac{\partial h}{\partial y}, \tag{2.3.2}$$

$$\frac{\partial}{\partial t}(2.2.2b) - f(2.2.2a) \quad \Rightarrow \quad \left(\frac{\partial^2}{\partial t^2} + f^2\right)v = -g\frac{\partial^2 h}{\partial t \partial y} + gf\frac{\partial h}{\partial x}, \tag{2.3.3}$$

$$\text{In vector form} \quad \Rightarrow \quad \left(\frac{\partial^2}{\partial t^2} + f^2\right)\mathbf{u} = -g\nabla\frac{\partial h}{\partial t} + fg(\hat{\mathbf{z}} \times \nabla h). \tag{2.3.4}$$

This gives us the velocity in terms of surface slope and by operating on the continuity equation (2.2.2c) with $(\partial_{tt} + f^2)$ we obtain the following,

$$\left(\frac{\partial^2}{\partial t^2} + f^2\right)\frac{\partial h}{\partial t} - g\nabla \cdot \left(H_0\nabla\frac{\partial h}{\partial t}\right) - fgJ(H_0, h) = 0, \tag{2.3.5}$$

where $J(H_0, h)$ represents the Jacobian of H_0 and h. Notice here that the first term describes the free surface deformation whilst the last two terms are what we see in the *TWE* (2.2.13). This third-order partial differential equation (PDE henceforth) will yield three different wave-type solutions when solved. We now non-dimensionalise again using the same variables as before, as well as letting $f = f_0\hat{f}$ to obtain (dropping hats again),

$$\frac{L^2}{a^2}\Big(\frac{\partial^2}{\partial t^2}+f^2\Big)\frac{\partial h}{\partial t}-g\nabla\cdot\Big(H_0\nabla\frac{\partial h}{\partial t}\Big)-fgJ(H_0,h)=0 \quad \text{where} \quad a:=\frac{\sqrt{gD}}{f}. \tag{2.3.6}$$

The parameter a is defined as the *Rossby radius*: the length scale at which rotational effects become as important as gravity/buoyancy forces [11]. This extra scale on the free surface term is clearly scale variant with L, however the rigid lid assumption is equivalent to taking a very large Rossby radius, in which case the first term vanishes and we arrive back at the original *TWE* (2.2.13) in terms of the free surface [18, p. 11].

2.4 Cylindrical Transform

Now we are in a position to begin solving problem (2.3.1). It is possible to find analytical solutions to this problem in axisymmetric domains, however as we are working within the half cone, we must search for these solutions numerically. In order to do this we need to go back to the cylindrical coordinate system described in Section 2.1 and transform the terms $\psi(x,y,t)=\psi(r,\theta,t)$ and $H_0(x,y)=H_0(r)$. Having used the shallow water assumption there is no z dependence in the equations so technically we only need polar coordinates for this problem. Making use of standard polar derivatives, (2.3.1) becomes

$$\left[\Big(\frac{r}{H_0}\psi_r\Big)_r+\Big(\frac{1}{rH_0}\psi_\theta\Big)_\theta\right]_t+\psi_r\Big(\frac{1}{H_0}\Big)_\theta-\psi_\theta\Big(\frac{1}{H_0}\Big)_r=0 \quad \text{in} \quad V. \tag{2.4.1}$$

Leaving $H_0(r)$ as a generic depth profile for now, we consider harmonic solutions of the form $\psi(r,\theta,t)=\phi(r,\theta)e^{i\omega t}$ with frequency ω. Working within a complete circle would allow us to fully separate variables however as we are working within a semicircle we must combine the r and θ dependence. Substituting the solution into (2.4.1) and simplifying

$$\left[\Big(\frac{r}{H_0}\phi_re^{i\omega t}\Big)_r+\Big(\frac{1}{rH_0}\phi_\theta e^{i\omega t}\Big)_\theta\right]_t+\phi_re^{i\omega t}\underbrace{\Big(\frac{1}{H_0}\Big)_\theta}_{=0}-\phi_\theta e^{i\omega t}\Big(\frac{1}{H_0}\Big)_r=0, \tag{2.4.2}$$

$$\Rightarrow \quad i\omega\left[\Big(\frac{r}{H_0}\phi_r\Big)_r+\Big(\frac{1}{rH_0}\phi_\theta\Big)_\theta\right]-\phi_\theta\Big(\frac{1}{H_0}\Big)_r=0. \tag{2.4.3}$$

Simplifying further we obtain[7],

---

[7] Where $H_0'(r)=\frac{dH_0}{dr}$.

$$i\omega\left[\frac{r}{H_0}\phi_{rr} + \frac{H_0 - rH_0'}{H_0^2}\phi_r + \frac{1}{rH_0}\phi_{\theta\theta}\right] = -\frac{H_0'}{H_0^2}\phi_\theta. \tag{2.4.4}$$

The two-dimensional problem for a general depth profile can then be written

$$irH_0'\phi_\theta = \omega\Big[r^2H_0\phi_{rr} + \big(rH_0 - r^2H_0'\big)\phi_r + H_0\phi_{\theta\theta}\Big] \quad \text{in} \quad V, \tag{2.4.5a}$$

$$\phi = 0 \quad \text{on} \quad \partial V. \tag{2.4.5b}$$

We define the depth profile as $H_0(r) = 1 - sr$ where $s \in [0, 1]$ is the slope of the container bottom, recalling that $H_0(r) = -h_b(r)$ is the original depth profile (i.e. $h_b(r) = sr - 1$). We are clearly interested in the half cone case $s = 1$ given in Figure 2.3 (right) however we make use of the $s = 1/2$ case (left) in order to check the numerical methods in Section 2.5 work correctly. We need to solve a differential eigenvalue problem (2.4.5), with non-constant coefficients, where the frequency ω is the eigenvalue. The easiest way to solve this problem is to use a numerical method, more specifically a spectral method, similar to the one formulated by Johnson and Rodney in [21].

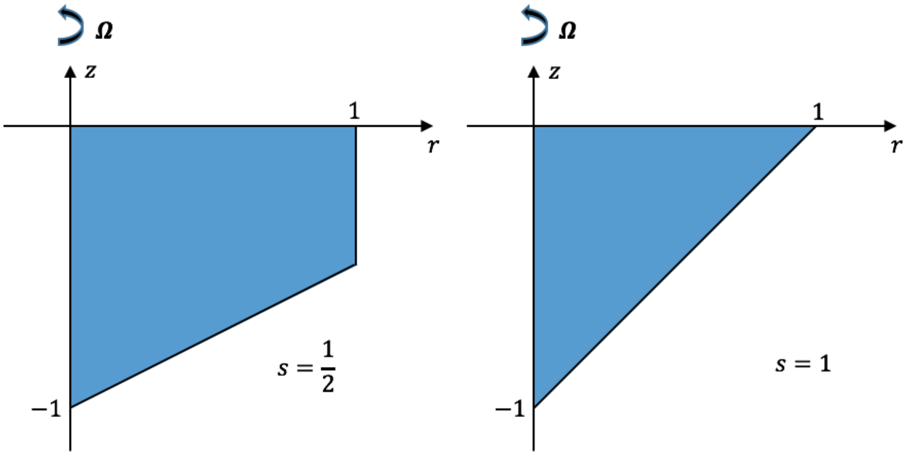

Figure 2.3: Depth profiles $h_b(r)$ for a half cylinder with sloping bottom ($s = 1/2$) and a half cone ($s = 1$).

2.5 The Spectral Method

Spectral methods are one of many different techniques[8] used in the numerical calculation of solutions to ordinary and partial differential equations [29]. Their development traces

---

[8] Significant others include the finite difference, element and volume methods to name but a few.

back to the early 20th century however they were extensively developed for fluid mechanics and meteorology during the 1970's and 1980's by Gottlieb and Orszag [12] and Canuto, Hussaini, Quarteroni and Zang [8]. More recently they have been studied and analysed at length in detailed works by Boyd [5] and, more relevant to this study, in MATLAB® by Trefethen [29].

These methods are very closely related to finite element methods (FEM) in the sense that to solve a differential equation, the solution is expressed as the sum of a set of basis functions (with respect to a particular vector space), multiplied by some coefficients that are to be determined by the method. The FEM requires basis functions to be non-zero over small subdomains (the finite elements) whereas spectral methods take a more global approach by requiring that basis functions be non-zero over the entire domain [29]. The domain still needs to be discretised into a number of points and the method involves the construction of *differentiation matrices* to replace differential operators in equations. Therefore instead of solving a differential, we need only solve a matrix problem, for which many efficient methods exist.

This means they can provide extremely good accuracy when solving ODE and PDE problems in domains where initial data and boundary conditions are sufficiently smooth[9]. They are incredibly straightforward to code up on software packages such as MATLAB which we use for all numerical results in this study.

We have reduced the TWE to a two-dimensional generalised linear eigenvalue problem (2.4.5) of the form $L\phi = \omega M\phi$ where ω is the eigenvalue and L and M are the differential operators given by

$$L = irH_0'\partial_\theta \quad \text{and} \quad M = r^2H_0\partial_{rr} + (rH_0 - r^2H_0')\partial_r + H_0\partial_{\theta\theta}. \tag{2.5.1}$$

Following similar methods presented in [5] and [21] we must carry out the following steps in order to solve the problem using the spectral method.

1. Transform the standard Chebyshev tensor product grid $[-1,1]\times[-1,1]$ into the scaled rectangle $[0,\pi]\times[0,1]$ and scale the Chebyshev differentiation matrices appropriately for this new domain. Then we discretise appropriately in order to utilise the spectral method.

2. Convert the *differential* eigenvalue problem $L\phi = \omega M\phi$ into a generalised *matrix* eigenvalue problem of the form $A\boldsymbol{\phi} = \omega B\boldsymbol{\phi}$ where A and B are discrete matrix operators and $\boldsymbol{\phi}$ is the eigenvector (or mode) corresponding to the eigenvalue ω.

3. Solve this problem using the QZ algorithm[10] in MATLAB to obtain $\boldsymbol{\phi}$ and ω at

---

[9] We do not delve into the accuracy of the method here but for a more detailed insight see [5].

[10] The MATLAB command `[V,E] = eig(A,B,'qz')` implements the QZ algorithm and returns a matrix V whose columns contain the eigenvectors $\boldsymbol{\phi_n}$ and a matrix E with the corresponding eigenvalues ω_n along the diagonal.

a discrete number of modes (plotting modes back on the polar domain, not the rectangle).

4. Filter out the non-physical and numerically spurious eigenvalues that are found as a result of the spectral method.

5. Finally calculate the full superposed solution with an appropriate initial condition that generates spin-down in the container.

Step 1

The current semi-circular domain could be easily discretised using Chebyshev collocation points in both θ and r, however the Chebyshev polynomials are strictly defined over $[-1, 1]$ so we need to transform the usual Chebyshev square $(\hat{\theta}, \hat{r}) \in [-1, 1] \times [-1, 1]$ onto the smaller domain $(\theta, r) \in [0, \pi] \times [0, 1]$. To do this, we apply the following transformations

$$r = \frac{1}{2}(\hat{r} + 1) \quad \text{and} \quad \theta = \frac{\pi}{2}(\hat{\theta} + 1). \tag{2.5.2}$$

Therefore in order to solve the problem in the half circle V, we need only solve it for (θ, r) on the rectangle $\mathcal{D} := [0, \pi] \times [0, 1]$ and plot the results over the corresponding polar coordinates in V. We now discretise $\mathcal{D}$ into a two-dimensional grid of independent Chebyshev points called a *tensor product grid* [29]. In order to do this we use Chebyshev collocation points[11] in both the θ and r directions,

$$\theta_i = \cos\big(\frac{i\pi}{M}\big) \quad \text{for} \quad i = 0, \ldots, M, \tag{2.5.3a}$$

$$r_j = \cos\big(\frac{j\pi}{N}\big) \quad \text{for} \quad j = 0, \ldots, N. \tag{2.5.3b}$$

With $M + 1$ and $N + 1$ points in each direction respectively, we can form a mesh of $(M+1)(N+1)$ points on the rectangle $\mathcal{D}$, Figure 2.4 (left), where we observe clustering at the boundaries and, even more so, the corners. This is an excellent feature of the spectral method as interesting dynamics often occur near boundaries and high spatial accuracy is perfect for capturing this. The corresponding mesh in the semicircular domain V is shown in Figure 2.5 (left) where we can see the clustering near the boundaries once again. Notice that as boundaries in V map to boundaries in $\mathcal{D}$, the boundary condition on ϕ does not change. This will be very useful when we form the matrix operators later.

---

[11] Strictly these are 'Chebyshev-Gauss-Lobatto' points that include the end points $\{-1, 1\}$ as opposed to other such Chebyshev points that do not [5].

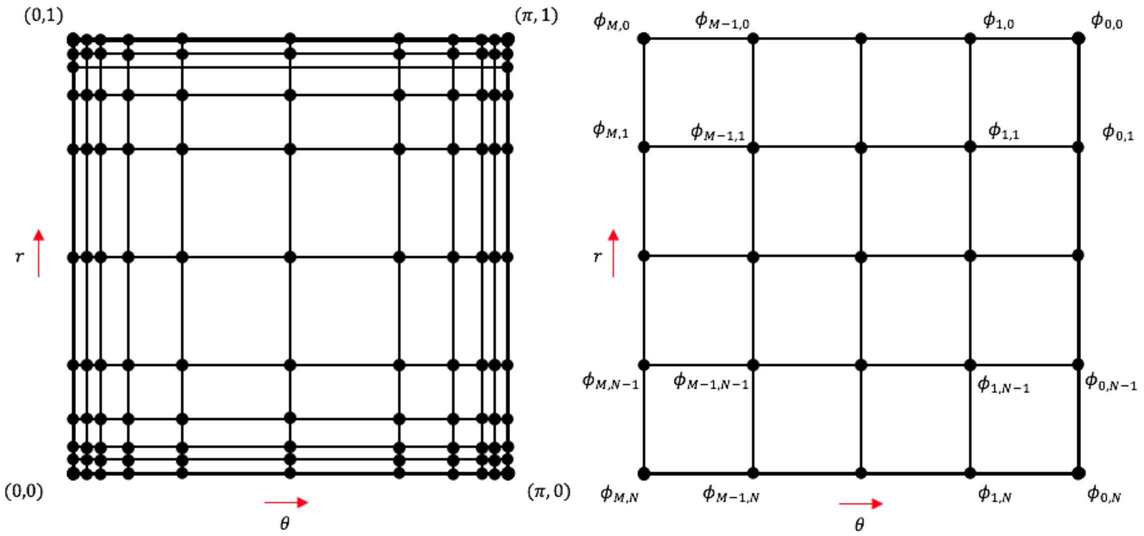

Figure 2.4: The Chebyshev tensor product grid in the rectangular domain $\mathcal{D}$ (left) and node numbering structure (right).

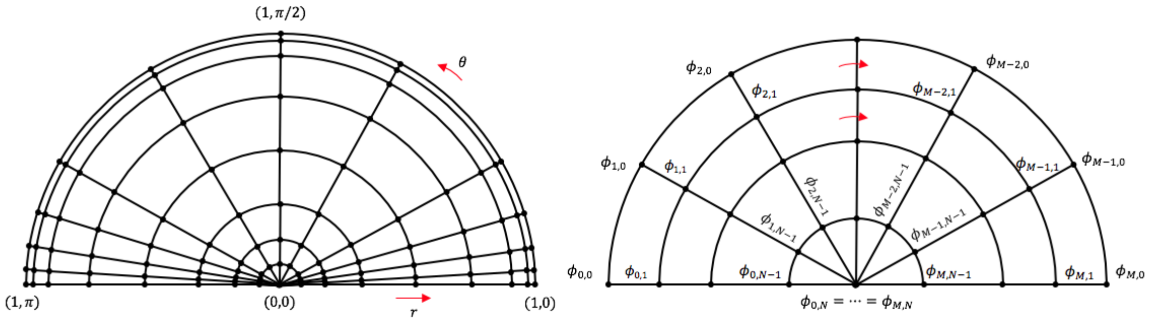

Figure 2.5: The Chebyshev grid in the semi-circular domain V (left) and corresponding node numbering with respect to Figure 2.4 is given (right).

The aim is to evaluate ϕ at each of the nodes in $\mathcal{D}$ so we introduce node numbering from the top right corner, moving left and then repeating row by row, depicted in Figure 2.4 (right). Note however that this figure has not been drawn as a Chebyshev mesh in order to make the node numbering clear to the reader; the actual mesh still looks like the left hand diagram in Figure 2.4 with the same node ordering. The corresponding node ordering once transformed back to V is given in Figure 2.5 (right).

The next task is to calculate the discrete matrix operators that will replace the current differential operators we have in (2.4.5). In order to do this we introduce the *Chebyshev spectral differentiation matrix*. This matrix will allows us to differentiate over the set of discrete Chebyshev points θ_i and r_j [29, pg.53]. The entries of the $(N+1)\times(N+1)$ Chebyshev differentiation matrix for collocation points $x_i \in [-1,1]$ are defined as

$$D_x = \begin{cases} \dfrac{2N^2+1}{6} & i=j=0 \qquad (2.5.4a) \\ -\dfrac{2N^2+1}{6} & i=j=N \qquad (2.5.4b) \\ \dfrac{-x_i}{2(1-x_i^2)} & i=j=1,\dots,N-1 \qquad (2.5.4c) \\ \dfrac{c_i}{c_j}\dfrac{(-1)^{i+j}}{(x_i-x_j)} & i\neq j \quad i,j=0,\dots,N \qquad (2.5.4d) \end{cases}$$

where $c_i = \begin{cases} 2 & i=0,N \\ 1 & \text{otherwise} \end{cases}$.

The function `[D,x] = cheb(N)` has been very helpfully written by Trefethen [29] to produce the first derivative matrix `D` and the vector of collocation points `x` for any $N \geq 1$ (see Appendix B.1). These operate strictly on functions defined over $[-1,1]$ so they need to be adjusted in order to work on the domain $\mathcal{D}$. For the θ matrix this is easily done by scaling such that $D_\theta \to (2/\pi)D_\theta$ and for the r matrix $D_r \to 2D_r$. This follows by using the chain rule with the transformations given in (2.5.2). The matrix for the second derivatives is simply the square of the first derivative matrix, for example, $D_{rr} = D_r^{(2)} = (D_r)^2$.

Step 2

To convert the differential eigenvalue problem into matrix form we must introduce an operator, the *Kronecker product* [17]. The Kronecker product, $A\otimes B$, of matrices A and B, dimensions $p\times q$ and $r\times s$ respectively, is a block matrix of dimension $pq\times rs$ such that

$$A\otimes B = \left[\begin{array}{c|c|c} a_{1,1}B & \dots & a_{1,q}B \\ \hline \vdots & \ddots & \vdots \\ \hline a_{p,1}B & \dots & a_{p,q}B \end{array}\right]. \qquad (2.5.5)$$

In MATLAB the Kronecker product is called with the command `kron(A,B)`. These products allow us to differentiate in the θ and r directions, where the n^{th} derivatives are defined in matrix form as

$$\frac{\partial^{(n)}}{\partial\theta^{(n)}} \longrightarrow I_{N+1}\otimes D_\theta^{(n)} \quad \text{and} \quad \frac{\partial^{(n)}}{\partial r^{(n)}} \longrightarrow D_r^{(n)}\otimes I_{M+1}, \qquad (2.5.6)$$

where I_{N+1} and I_{M+1} are identity matrices of size $N+1$ and $M+1$ respectively [29]. Next we must write the non-constant coefficients in matrix form. Each r, r^2, H_0 and H_0' in (2.4.5) becomes a vector of collocation points in r so for each coefficient we need to calculate a matrix. For example the first coefficient, irH_0', is calculated as `kron(1i*diag_r*diag_H_r),Dt)` where `diag` places the vector on the diagonal of an empty matrix (see Appendix B.2). The other coefficients are calculated similarly and we are almost ready to enter them into the full matrix problem.

We must ensure we enact the homogeneous boundary conditions on $\partial\mathcal{D}$, so we notice that in the solution vector,

$$\begin{aligned}\boldsymbol{\phi} = \big(&\underbrace{\phi_{0,0},\dots,\phi_{M,0}}_{=0}\,\big|\,\underbrace{\phi_{0,1}}_{=0},\phi_{1,1},\dots,\phi_{M-1,1},\underbrace{\phi_{M,1}}_{=0}\,\big|\cdots\cdots\\ &\cdots\big|\,\underbrace{\phi_{0,N-1}}_{=0},\phi_{1,N-1},\dots,\phi_{M-1,N-1},\underbrace{\phi_{M,N-1}}_{=0}\,\big|\,\underbrace{\phi_{0,N},\dots,\phi_{M,N}}_{=0}\big),\end{aligned} \tag{2.5.7}$$

the boundary terms can all be set to zero. Note that the solid lines make the vector more readable and have no mathematical meaning. To include this in the differentiation matrices and coefficient vectors we can just remove the edge rows/columns of all matrices and the first/last elements of all vectors. The final matrix problem to be solved in MATLAB, $A\boldsymbol{\phi} = \omega B\boldsymbol{\phi}$, where the non-constant coefficients are now diagonal matrices not scalars, is written as

$$\begin{aligned}\Big[\text{diag}(irH_0')\otimes D_\theta\Big]\boldsymbol{\phi} = \omega\Big[&\big(\text{diag}(r^2H_0)D_{rr}\otimes I_{M-1}\big)+\dots\\ &\dots\big(\text{diag}(rH_0 - r^2H_0')D_r\otimes I_{M-1}\big)+\big(\text{diag}(H_0)\otimes D_{\theta\theta}\big)\Big]\boldsymbol{\phi}.\end{aligned} \tag{2.5.8}$$

Step 3

Now we are able to solve the problem directly in MATLAB using the function `[V,E,I,T,R] = inviscid_half_cone(M,N,s)` detailed in Appendix B.2. The resolution is set with `M+1` and `N+1` points and the gradient of the topography with `s`. It solves (2.5.8) and produces a matrix `V` of eigenvectors, the corresponding eigenvalues `E`, the eigenvalue ordering vector `I` (in descending absolute frequency ω) and the collocation vectors `T` and `R` in θ and r respectively. The function will evaluate all modes of the system however there will be many that are either physically or numerically spurious and hence we will need to filter these out from the correct modes.

Step 4

Spurious eigenvalues arise when solving generalised eigenvalue problems as a result of the spectral discretisation and will either be numerically inaccurate, due to the spectral scheme, or physically non-existent, due to some unexplained physics of the equation [5]. They occur mostly, if not always, in generalised non-periodic eigenvalue problems such as this one. By computing the eigenvalues at low and high spectral resolutions, (M_1, N_1) and (M_2, N_2), both fine enough to guarantee accuracy, we can order them in decreasing absolute value and then compare which are close enough together to determine the 'good' and 'bad' eigenvalues. This is clearly tedious for large numbers of eigenvalues so Boyd, [5], suggests plotting the reciprocal of the difference between corresponding eigenvalues in the different resolutions on a logarithmic scale. The 'good' eigenvalues will then appear at the top of a plot between the mode number and these differences, see Figure 2.7. Firstly, define the intermodal separation of the low resolution eigenvalues, σ_n, as

$$\sigma_1 = |\omega_1 - \omega_2|, \tag{2.5.9a}$$

$$\sigma_n = \frac{1}{2}\big(|\omega_n - \omega_{n-1}| + |\omega_{n+1} - \omega_n|\big) \quad \text{for} \quad n \geq 2. \tag{2.5.9b}$$

'Good' and 'bad' eigenvalues may become mixed at the two different resolutions so Boyd suggests comparing the n^{th} low resolution eigenvalue with the closest related l^{th} eigenvalue from the high resolution using the following relation[12] (adapted in [21] for two dimensions):

$$\delta_{n,nearest} = \min_{l\in[1,N_2,M_2]} |\omega_n^{(N_1,M_1)} - \omega_l^{(N_2,M_2)}| / \min\{|\omega_n|, \sigma_n, |Re(\omega_n)|, |Im(\omega_n)|\}. \tag{2.5.10}$$

This will ensure that 'good' eigenvalues have large values of $log(1/\delta_{n,nearest})$ whilst the more spurious ones will have a much smaller value. Johnson and Rodney demonstrate that this method is highly accurate by computing the eigenvalues spectrally and analytically for a coastal-trapped trapped wave problem in [21].

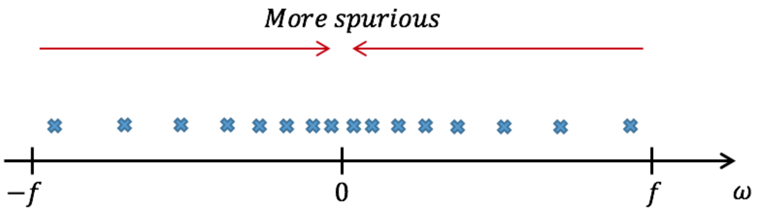

Figure 2.6: An approximate depiction of the spatial distribution of numerical eigenvalues (crosses) produced by `inviscid_half_cone.m`.

In order to verify that the spectral method above is indeed accurate, we show, in Appendix A, that the eigenvalues of the inviscid TWE system are all real and will have

---

[12] Note that the denominator must be changed to $\min\{|\omega_n|, \sigma_n\}$ if the eigenvalues ω_n are purely real, to avoid undefined δ.

corresponding modes with subinertial frequencies $|\omega| \leq f$ only. Note however that f has been scaled with time so $|\omega| \leq 1$ in this case and hence ω has the approximate spatial distribution given in Figure 2.6.

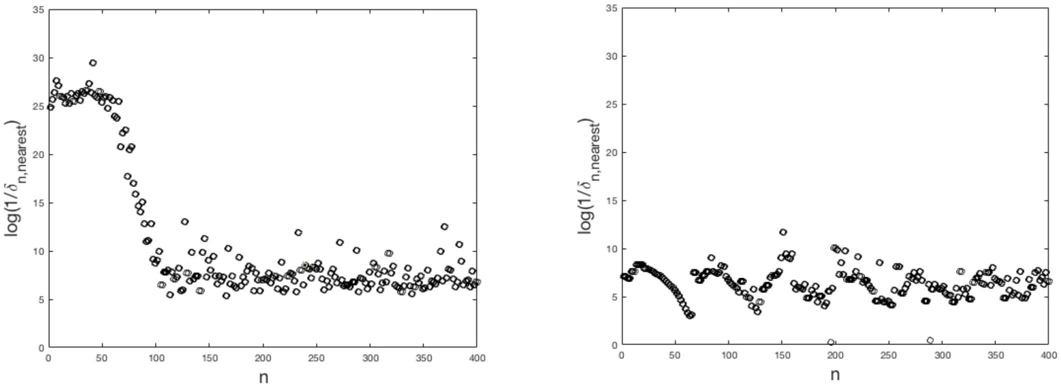

(a) $s = 1/2$

(b) $s = 1$

Figure 2.7: The ratio $log(1/\delta_{n,nearest})$ against mode number n for lower spatial resolution $(M, N) = (70, 70)$ and higher resolution $(75, 75)$ in the topography cases $s = 1/2$ and $s = 1$ (Note: eigenvalues have been sorted into absolute decreasing order).

The 'good' eigenvalues for problem (2.5.8) are determined by running the MATLAB script `spurious_eigenvalues.m` given in Appendix B.3. The plots of $log(1/\delta_{n,nearest})$ against the first 400 mode numbers are plotted in Figure 2.7 for both the $s = 1/2$ and $s = 1$ cases. Choosing 20 as the cutoff value, above which eigenvalues are deemed 'good', we obtain 88 non-spurious modes in the half cylinder, with the first 20 located at the frequencies given in Table 2.1. These frequencies have modulus less than one and are all real, as proved in Appendix A, demonstrating that the numerical method is correct. The results for the half cone geometry are displayed in Figure 2.7b. Initial observation indicates that there is no obviously specific group of 'good' modes that emerge toward the top of the plot. Most exist randomly, potentially periodically, between the values of 0 and 10 meaning that in the limit of $s \to 1$ the system has *no* stable (discrete) set of oscillatory modes. As of yet we cannot say whether this is because of the unique geometry of the half cone or because the depth in the half cylinder tends to zero. However, we can say that the half cone/cylinder vertex *does not* strictly prohibit the existence of oscillatory modes as stated in [22]. Now we discuss the mode structure and introduce the spin-down initial condition.

Mode (n)	ω_n	Mode (n)	ω_n
1	0.0837	11	-0.0438
2	-0.0837	12	0.0438
3	-0.0712	13	0.0414
4	0.0712	14	-0.0414
5	0.0615	15	-0.0402
6	-0.0615	16	0.0402
7	0.0541	17	0.0384
8	-0.0541	18	-0.0384
9	-0.0483	19	0.0371
10	0.0483	20	-0.0371

Table 2.1: The first twenty 'good' numerical eigenvalues, rounded to 4 decimal places, produced by `inviscid_half_cone(70,70,0.5).m`.

2.6 Modes

Plotting the streamlines of the first four modes in the $s = 1/2$ case (Figure 2.8) we observe that the simplest mode ($n = 1$) is formed of two to three main gyres that are cyclonic and anticyclonic alternatively. We can now plot the harmonic solution $\psi_1(r, \theta, t) = \phi_1(r, \theta)e^{i\omega_1 t}$ for mode 1 (as well as other higher 'good' modes) over the time period $T = 2\pi/\omega_1$ in order to observe how the mode propagates through time. In doing so we observe the gyres propagating to the western corner of the container with shallow water on the right as expected (see Figure 2.9). The gyres also shrink in spatial extent as they approach shallower water and the number of gyres is conserved throughout the period of the mode. This is exactly the overall motion that Li et al. find after running their simulations of the (viscous) linear spin-up/down problem. The westward propagation is a major result that Li et al. discover in their experiments and simulations, however in the study of large rotating ocean basins, authors such as Ekman, Stommel, Sverdrup and Munk have already proved that waves always propagate in a westerly direction under the influence of rotation.

We must, however, focus on the half cone case to accurately compare with the observations in [22]. Li et al. state that no modes can exist in the half cone geometry because the vertex of the cone "precludes" their existence and therefore they have no way to form stably. We have confirmed this statement by showing that there is no discrete set of stable eigenvalues for the half cone system however it is not the vertex prohibiting their existence because we know they exist in the $s = 1/2$ case. To further verify that the $s = 1$ eigenvalues are physically spurious and hence unstable we plot the four 'best' four modes from the eigenvalue analysis in Figure 2.10. All four modes (and subsequent others) display no large scale basin modes that would be expected from the analysis in [22], so how do we proceed from here? First we will introduce the initial spin-down condition to fully solve the

$s = 1/2$ case and then integrate the full time-dependent problem to determine a solution for the half cone case, checking the $s = 1/2$ solutions match as we go.

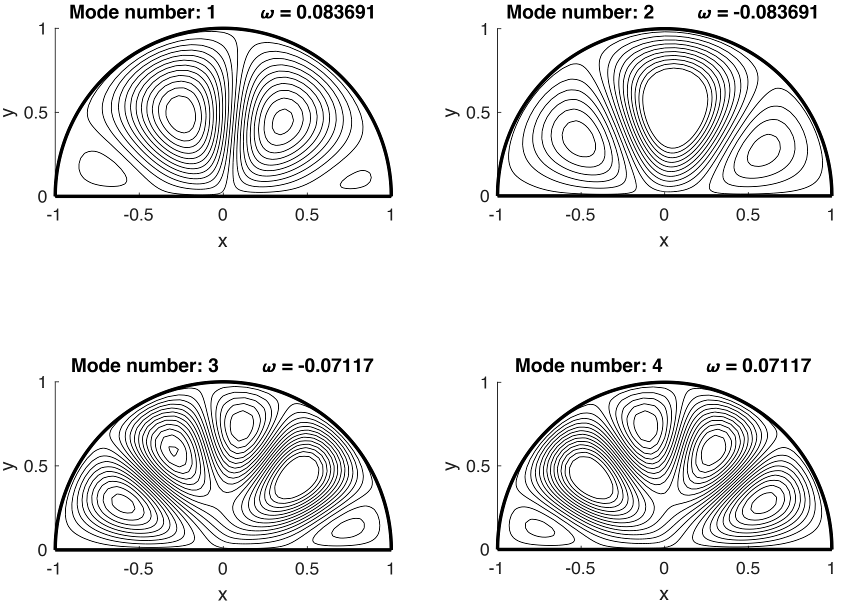

Figure 2.8: Streamline patterns of the first four modes (with largest absolute frequency) in the s = 1/2 case.

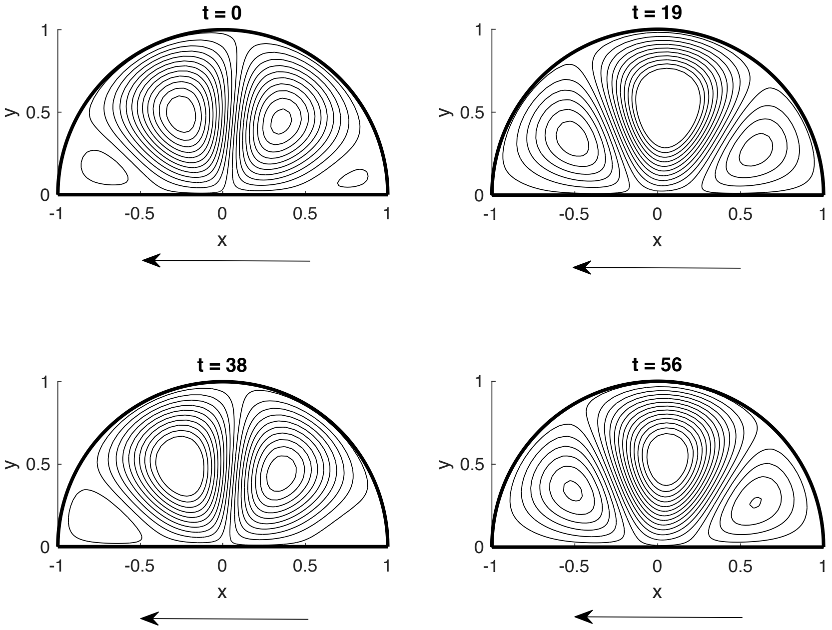

Figure 2.9: Time snapshots of mode 1 (s = 1/2) over quarter intervals of the period T (t = 0, T/4, T/2 and 3T/4) with propagation direction given by arrows.

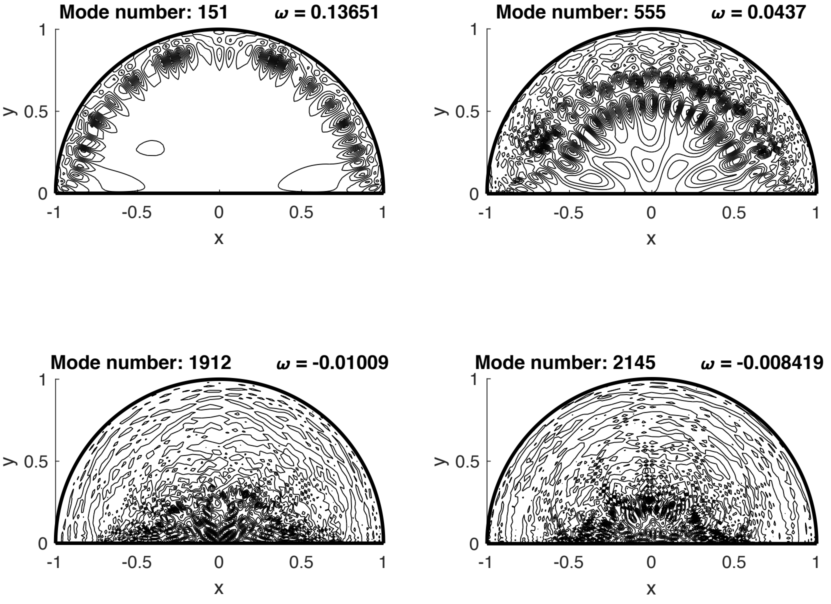

Figure 2.10: The 'best' modes in the $s = 1$ case from Figure 2.7b.

2.7 Initial Condition

Now that we are able to determine the normal modes, we must understand how the system responds to an initial spin-down in the rotation rate of the container. We have assumed that the fluid is in rigid body rotation for $t \leq 0$ (see Section 2.1), which means the that $\boldsymbol{u} = \mathbf{0}$ in the rotating frame and hence the initial vorticity is zero, $\boldsymbol{\zeta} = \nabla \times \boldsymbol{u} = \mathbf{0}$. Spin-down will generate anticyclonic (negative) vorticity close to the side boundaries whilst the interior fluid (initially) will remain at rest in the rotating frame. This is equivalent to introducing cyclonic (positive) vorticity within the interior of the container at $t = 0^+$ and hence we introduce the initial vorticity condition

$$\zeta(r, \theta, 0) = \nabla \cdot \left(\frac{\nabla \psi}{H_0}\right) = \begin{cases} +1 & \text{for spin-down} \\ -1 & \text{for spin-up} \end{cases} \quad \text{at} \quad t = 0^+. \tag{2.7.1}$$

Clearly we select $+1$ for the spin-down case. This will generate a single gyre in the half cone that will spin-down the fluid, see Figure 2.11a, which is calculated by solving (2.9.3)-(2.9.4) in Section 2.9. Whereas the spin-down generates positive vorticity, the spin-up in Figure 2.11b (from [22, Fig.2]) generates negative vorticity. We compare both plots to show that the overall structure of the mass transport is the same. Note that as the Coriolis parameter f stays fixed throughout this problem, what the initial condition really does is instantaneously slow down the container and then return to the previous rotation rate. Whilst not strictly the same problem presented in [22], it contains all the same dynamical effects and corresponds to the linear spin-down case they discuss.

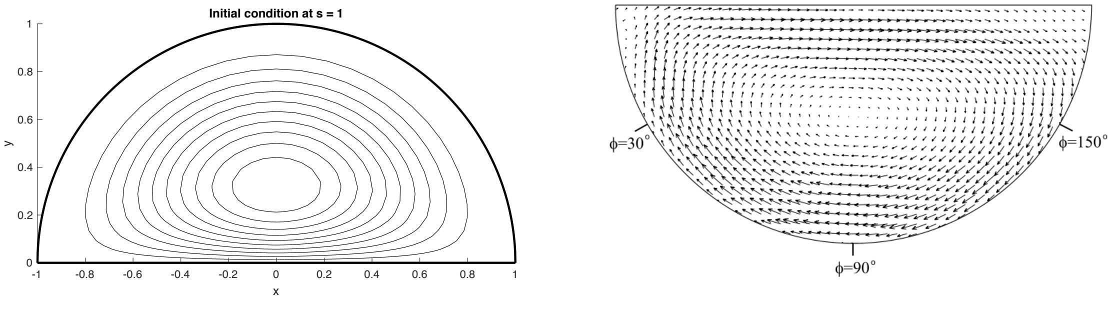

(a) (b)

Figure 2.11: (a) The spin-down streamline pattern generated by the initial vorticity condition given in (2.7.1). (b) The horizontal velocity field generated at $z = 0.9$ by spin-up in [22, Fig.2].

Using the superposed solution (2.7.2) detailed in Appendix A, we are now in a position to introduce the initial condition (2.7.1). Note that $\bar{N}$ is the total number of 'good' modes included in the final solution.

$$\psi = \sum_{n=1}^{\bar{N}} a_n \phi_n(r,\theta) e^{i\omega_n t} \quad \text{where} \quad a_n = \frac{\langle \psi, \phi_n \rangle}{\langle \phi_n, \phi_n \rangle} = \frac{\langle \psi, \phi_n \rangle}{E(\phi_n)}. \tag{2.7.2}$$

The initial condition at $t = 0$ implies that

$$\psi(r,\theta,0) = \sum_{n=1}^{\bar{N}} a_n \phi_n. \tag{2.7.3}$$

Take (2.7.1), multiply by ϕ_m, for any $m \in \{1, ..., \bar{N}\}$, and integrate over V in order to determine the coefficients of the superposed solution. We use the product rule, then the divergence theorem and boundary condition and finally the definition of the inner product from Appendix A to obtain the following argument

$$\sum_{n=1}^{\bar{N}} a_n \int_V \phi_m \nabla \cdot \big(\frac{\nabla \phi_n}{H_0}\big)\ dV = \int_V \phi_m\ dV, \tag{2.7.4}$$

$$\sum_{n=1}^{\bar{N}} a_n \int_V \nabla \cdot \big(\frac{\phi_m}{H_0} \nabla \phi_n\big) - \nabla \phi_m \cdot \frac{\nabla \phi_n}{H_0}\ dV = \int_V \phi_m\ dV, \tag{2.7.5}$$

$$\sum_{n=1}^{\bar{N}} a_n \underbrace{\int_{\partial V} \frac{\phi_m}{H_0} \nabla \phi_n \cdot \hat{\mathbf{n}}\ dS}_{=0} - \int_V \frac{1}{H_0} \nabla \phi_m \cdot \nabla \phi_n\ dV = \int_V \phi_m\ dV, \tag{2.7.6}$$

$$\sum_{n=1}^{\bar{N}} a_n \langle \phi_m, \phi_n \rangle = -\int_V \phi_m\ dV, \tag{2.7.7}$$

$$a_m \langle \phi_m, \phi_m \rangle = -\int_V \phi_m\ dV \quad \Rightarrow \quad a_m = -\frac{\int_V \phi_m\ dV}{\langle \phi_m, \phi_m \rangle}. \tag{2.7.8}$$

The final line follows from the orthogonality of distinct eigenmodes proved in Appendix A. In order to calculate the integral of a specific mode ϕ_m numerically, we employ a relatively simple trick by integrating in the angular, and then radial, direction using the Chebyshev matrices [29]. We can write the integral as a derivative and then use the previously found Chebyshev matrices (2.5.6) to calculate the integral through matrix inversion[13]

---

[13] To invert the Chebyshev matrix the boundary conditions must be enacted (i.e. the first/last rows and columns must be removed) else the matrix will remain singular by definition.

$$I_1 = \int_0^{\pi} \phi_m(r,\theta)\ d\theta \quad \Rightarrow \quad \frac{dI_1}{d\theta} = \phi_m \quad \rightarrow \quad \underbrace{(I_{N-1} \otimes D_\theta)}_{invert} \boldsymbol{I_1} = \boldsymbol{\phi_m}. \tag{2.7.9}$$

In MATLAB this is done using the backslash command \ and the exact same process follows for integrating in the radial direction

$$I_2 = \int_0^{1} I_1\ dr \quad \Rightarrow \quad \frac{dI_2}{dr} = I_1 \quad \rightarrow \quad \underbrace{(D_r \otimes I_{M-1})}_{invert} \boldsymbol{I_2} = \boldsymbol{I_1}. \tag{2.7.10}$$

The MATLAB script built to calculate these coefficients is detailed in Appendix B.4 and is used to calculate the numerator of each coefficient in (2.7.8) and then the denominator $\langle \phi_m, \phi_m \rangle$ is calculated using the exact same method except that the integrand must be found using the Chebyshev matrices and polar derivatives first.

2.8 Full Spectral Solution

The full solution for $s = 1/2$ is calculated by superposing the first 30 modes in (2.7.2) and is plotted in Figure 2.13 at different time snapshots[14]. In this case we clearly see that the solution initially begins with a single large gyre in the centre of the domain, generated by the spin-down. It then proceeds to propagate westward and shrink in spatial extent until it reaches the shallow westward corner. The system is inviscid and hence there is clearly no way for the energy of the system to dissipate and so the large waves keep building on the south-western boundary. The streamline patterns appear non-smooth as a result of the superposition and hence may not be as accurate as we wish.

We know that individual modes are periodic however the superposed solution is not because the periods are not rational multiples of each other. This causes the solution to appear monotonic, modes propagating only westward and not reflected east, hence it could be a bad idea to form the solution as a superposition of modes. We can test how well the finite summation agrees with the true infinite superposition by measuring how much of the variance a superposition of $\bar{N}$ modes accounts for. To do this we quantify the variance by taking the inner product of the full solution ψ such that,

$$\langle \psi, \psi \rangle = \int_V \frac{1}{H_0} |\nabla \psi|^2\ dV = \int_V \frac{1}{H_0} \big(\sum_{n=1}^{\infty} a_n \nabla \phi_n \big) \cdot \big(\sum_{m=1}^{\infty} a_m \nabla \phi_m \big)\ dV, \tag{2.8.1}$$

---

[14] The full MATLAB animations of all the following solutions are located in the file 'Animated Solutions' within the supplementary material. Note that all animations are run at 16 frames per second and hence the propagation of the waves is 16x faster than normal in order to compress and shorten the files.

and then by the orthogonality of distinct modes

$$= \int_V \frac{1}{H_0} \sum_{n=1}^{\infty} a_n^2 |\nabla \phi_n|^2 \, dV = \sum_{n=1}^{\infty} a_n^2 \langle \phi_n, \phi_n \rangle \tag{2.8.2}$$

Therefore the full solution computed with an infinite number of modes will have variance 1 as can be seen in (2.8.3).

$$1 = \sum_{n=1}^{\infty} a_n^2 \frac{\langle \phi_n, \phi_n \rangle}{\langle \psi, \psi \rangle} \quad (\bar{N} = \infty) \tag{2.8.3}$$

$$0.75 = \sum_{n=1}^{30} a_n^2 \frac{\langle \phi_n, \phi_n \rangle}{\langle \psi, \psi \rangle} \quad (\bar{N} = 30) \tag{2.8.4}$$

We are interested in determining what percentage of the variance is captured when we only use the first 30 modes in the solution of ψ, in that case we calculate (2.8.4) meaning that only 75% of the variance is captured from the total of 88 good modes modes generated by `inviscid_half_cone.m`. A plot of the variance against changing summation range $\bar{N}$ is provided in Figure 2.12.

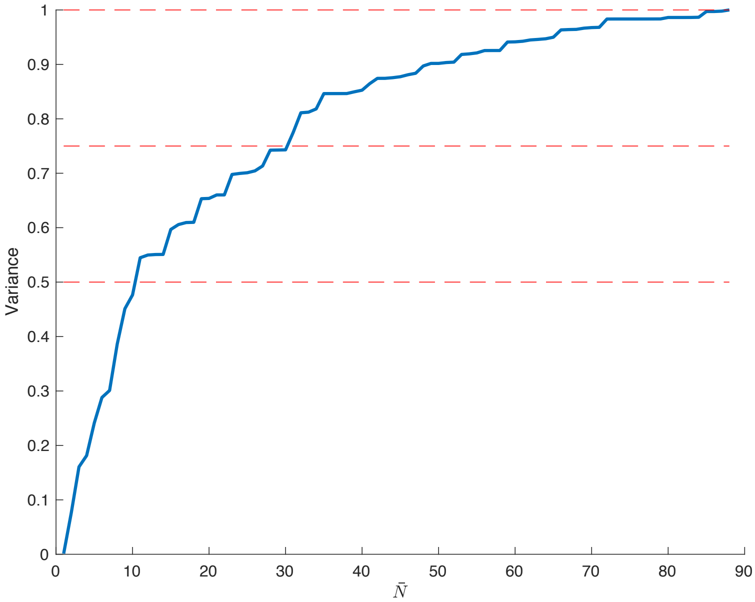

Figure 2.12: The variance against the number of modes used in the superposed solution (blue). Red dashed lines indicate where 50%, 75% and 100% of the variance is captured.

By superposing $\bar{N} = 11$ modes, 50% of the variance is captured, with $\bar{N} = 30$ we capture 75% and it takes a much higher number to reach the full variance. Even is higher modes are identified, by increasing the spectral resolution, we would still not be able to capture the full spin-down process. This means that it may not be such a good idea to find the superposed solutions and instead calculate the fully integrated time-dependent solution. The structure of the $s = 1$ case is still unknown to us as we have no discrete set of large scale basin modes to superpose. Is the transient spin-down motion similar to the $s = 1/2$ case or completely different? To find out what happens we will determine the fully time-dependent solutions to verify the $s = 1/2$ superposed solution and then discover the true $s = 1$ solution.

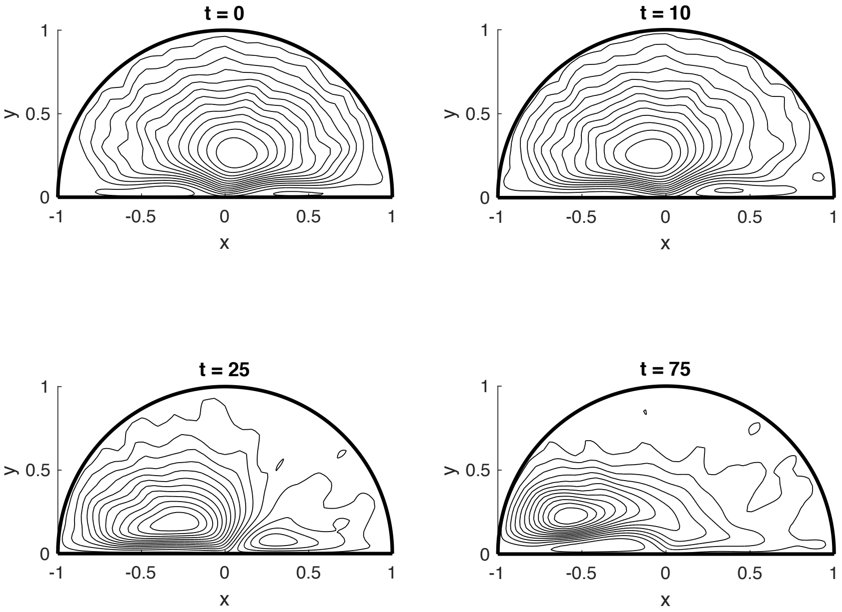

Figure 2.13: Time snapshots of the superposed solution for the $(\bar{N} = 30)$ most accurate modes in the half cylinder with slope. Contours are plotted at 0.01 increments.

2.9 Time-Dependent Solutions

Having been unable to determine modes for the half cone, we now solve the initial-boundary value problem using the time-dependent solution $\psi = \psi(r, \theta, t)$ in the TWE (2.3.1). This yields the following equation that we will need to integrate in both time and space.

$$\frac{\partial}{\partial t}\left(r^2 H_0 \psi_{rr} + (rH_0 - r^2 H_0')\psi_r + H_0 \psi_{\theta\theta}\right) = -rH_0'\psi_\theta. \tag{2.9.1}$$

We discretise the spatial derivatives in the exact same way as before, using the spectral matrices, to obtain a differential matrix problem, (2.9.2), where A and B are both spectral matrix operators we know and $\boldsymbol{\psi}$ is the solution vector that now only depends on time. As A is a linear matrix operator we may rearrange and invert (applying the boundary conditions as before) in order to obtain a simple linear system of first order ODEs that can be solved rapidly in MATLAB using solvers such as `ode15s.m` or `ode45.m`.

$$\frac{d}{dt}A\boldsymbol{\psi} = -B\boldsymbol{\psi} \quad \Rightarrow \quad \frac{d\boldsymbol{\psi}}{dt} = -A^{-1}B\boldsymbol{\psi} \tag{2.9.2}$$

To use `ode45.m` we also need to include an initial condition $\boldsymbol{\psi}_0$. We determine this by writing the initial vorticity condition (2.7.1) as a matrix operator and inverting, following steps (2.9.3)-(2.9.4).

$$\nabla \cdot \left(\frac{\nabla\psi_0}{H_0}\right) = 1 \quad \Rightarrow \quad \frac{1}{H_0}\psi_{0rr} + \frac{H_0 - rH_0'}{rH_0^2}\psi_{0r} + \frac{1}{r^2H_0}\psi_{0\theta\theta} = 1 \tag{2.9.3}$$

$$\text{(matrix form)} \quad \rightarrow \quad I_c\boldsymbol{\psi_0} = \mathbf{1} \quad \Rightarrow \quad \boldsymbol{\psi_0} = I_c^{-1}\mathbf{1}. \tag{2.9.4}$$

Using the ODE solver we obtain a series of vectors $\boldsymbol{\psi}$ at different times selected at regular intervals (every 1 second) and so we can immediately plot this series in an animation as we have done before. First we solve the $s = 1/2$ case using the code in Appendix B.5, see Figure 2.15 for time snapshots. On observation we see that the solutions confirm the general structure and motion of the superposed solution found in Section 2.8. The time-dependent solution however has much smoother streamline patterns and propagates to the west uniformly as expected whereas the modal solution slows and speeds up (see animations in supplementary material). Over time, alternating cells of cyclonic and anticyclonic motion are generated by the lateral eastern and south-eastern boundaries and build up on the south-western wall. As we have not included any viscosity yet, the energy has nowhere to dissipate and so it continually builds on the boundary via the larger modes. Clearly the inclusion of viscosity will cause the vorticity generated by the spin-down to be dissipated over time, reverting the system to rigid body rotation.

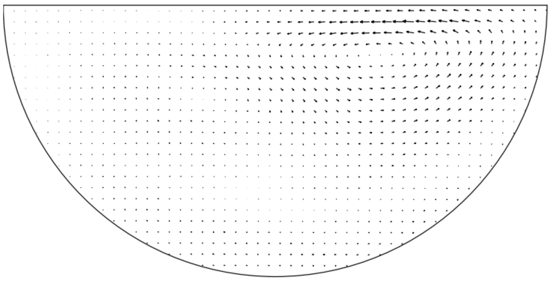

Figure 2.14: Horizontal velocity field at $z = 0.9$ in the half cone for the linear spin-down regime ($Ro = -0.05$) - taken from [22, Fig.3].

The full half cone case, in Figure 2.16, demonstrates very similar behaviour to the sloped half cylinder except that the initial vortex gyre is more compact and centered further into the southern (deeper) part of the cone. The long waves propagate, build up against the south-west wall and then reflect back east in the form of short waves around the shallow part of the half cone. The convergence of mass to the south-west wall occurs at a much faster rate than in the shallower slope case however. This makes sense because the steeper the topography, the faster the fluid is pushed toward the lateral walls. This matches the results found by Li et al. that describe propagation to the west and a high concentration of transport build up on the lateral half cone wall as shown in their two-dimensional simulations of horizontal velocity in [22, Fig.3] (see Figure 2.14). Now we tackle the problem in a rectangular container with and without a linearly sloping bottom to more clearly identify the dynamics and to begin including viscosity, ready to solve the viscous half cone problem.

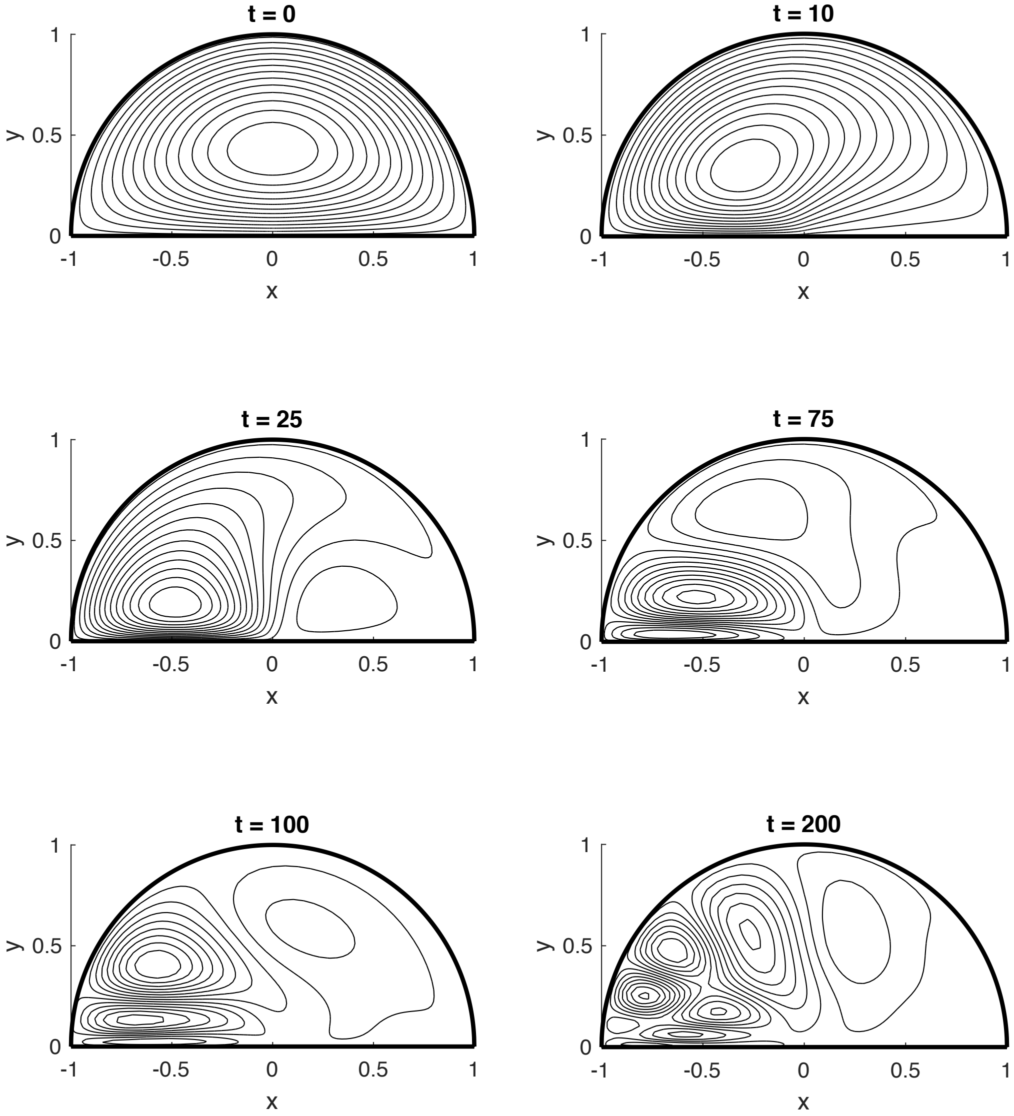

Figure 2.15: Streamline patterns of the time-dependent solution for the half cylinder ($s = 1/2$). The spectral resolution is fixed at $(M, N) = (70, 70)$ and contours are plotted at intervals of 0.005.

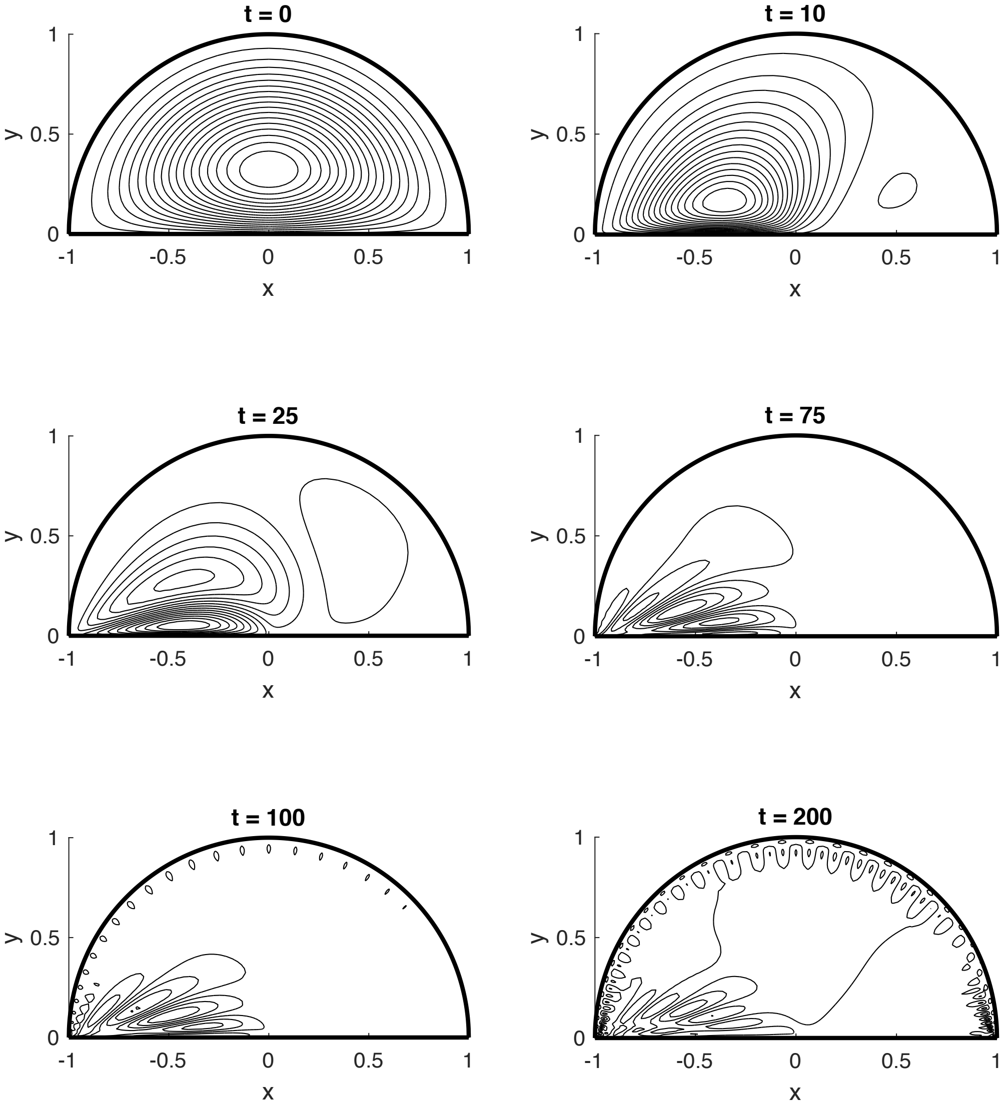

Figure 2.16: Streamline patterns of the time-dependent solution for the half cone ($s = 1$) plotted at intervals of 0.002.

Chapter 3

Spin-Down in a Rectangular Container

Now we consider a similar case to the half cone problem: spin-down in a rectangular container with a linearly sloping bottom profile. Figure 3.1 demonstrates how the rectangular container is essentially a 'stretched out' half cone whose modes, as we shall see, propagate west like the half cone/cylinder modes. First we consider the case in the very small slope limit, on the β-plane, where we can identify explicit analytical solutions for the wave modes of ψ. These solutions can then be used to verify the structure of the modes from the numerical results obtained in the larger slope case where we require the TWE once again. The dynamics produced in the viscous large slope case will give clearer indications of how the vorticity is destroyed, how waves are reflected (or not) and should demonstrate very similar features to the viscous half cone problem solved in Chapter 4.

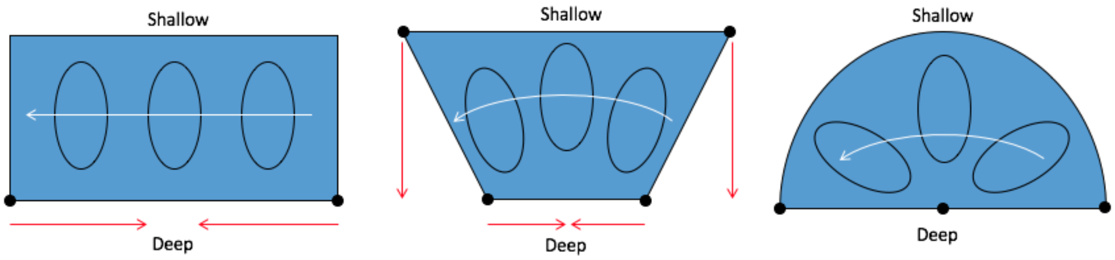

Figure 3.1: Depiction of how the rectangular geometry transforms into a semicircle (red arrows). White arrows show direction of propagation of some (non-real) wave modes.

3.1 Container with small slope (Inviscid)

We consider this case in order to understand the general motion and mode structure in the rectangular container by identifying an explicit analytical solution of the streamfunction. This will help confirm that the numerical results for larger slope are correct in the small slope limit.

Consider a rectangular container $[0, a] \times [0, b]$ of depth D, with very small slope in y, being rotated uniformly at angular velocity $\mathbf{\Omega_0}$ about the centre of the container at time $t \leq 0$, see Figure 3.2. The mass transport can be found by solving the TWE (2.2.13), as we have done previously in Chapter 2. However with the depth $H_0 = constant$, the $\nabla(f/H_0)$ term in the TWE is clearly zero and the Jacobian term drops out. We are left with the first term, the time derivative of potential vorticity, equal to zero, meaning there are no wave-like solutions to be found. The trivial solution is clearly the only one to satisfy this reduced equation due to the zero flux boundary conditions (still in place for this rectangular domain). In order to locate non-trivial solutions for this topography we must consider solutions on the β-plane instead. Recall that on the β-plane we allow the Coriolis parameter f to vary linearly in the northward y-direction such that $f = f_0 + \beta y$, hence the TWE (2.2.13) becomes

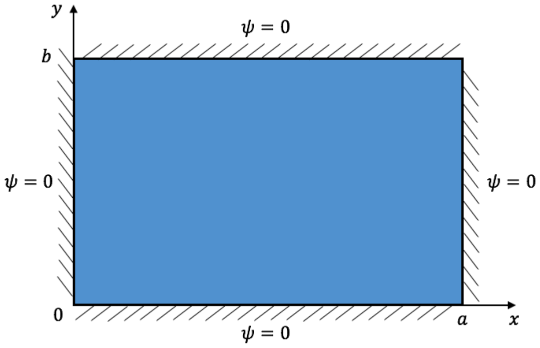

Figure 3.2: Plane view of the rectangular container with zero flux boundary conditions.

$$\frac{\partial}{\partial t}\nabla^2\psi + \beta\psi_x = 0. \tag{3.1.1}$$

The first term represents the rate of change of potential vorticity and the second is what Ekman described in his 1905 paper as the "planetary vorticity" term [10]. This is a classical problem in oceanic circulation modelling and was discussed at length by Stommel and Munk in [28] and [23]. The same zero flux boundary conditions as before also still apply

$$\psi = 0 \quad \text{on} \quad x = 0, a \quad \text{and} \quad y = 0, b. \tag{3.1.2}$$

Given equation (3.1.1) and the basin in Figure 3.2, it is clear that any solution of (3.1.1) must be homogeneous in y so we may plug in the separable solution $\psi = X(x)Y(y)e^{i\omega t}$

and solve using separation of variables. The full solution is written in superposed form, where all constants have been absorbed into D_n, as

$$\psi(x, y, t) = \sum_{m,n=1}^{\infty} D_{m,n} \underbrace{e^{i\frac{\beta x}{2\omega_{m,n}}} \sin\left(\frac{m\pi x}{a}\right) \sin\left(\frac{n\pi y}{b}\right)}_{=:\Phi_{m,n}} e^{i\omega_{m,n}t}. \tag{3.1.3}$$

A plot of the first four modes is given in Figure 3.3. They show a combination of large scale and smaller basin modes that propagate westward periodically with no deviation to the north or south. The superposed solution formed with the initial spin-down condition would consist of an infinite combination of these modes propagating the same direction, with a similar overall structure hence there is no need to include the condition here. Short waves would still be reflected back to the east with this topography however. It is expected that the modes will lose symmetry and deviate from the $y = 0.5$ line once a steeper gradient is introduced into the container, which is what we look at next.

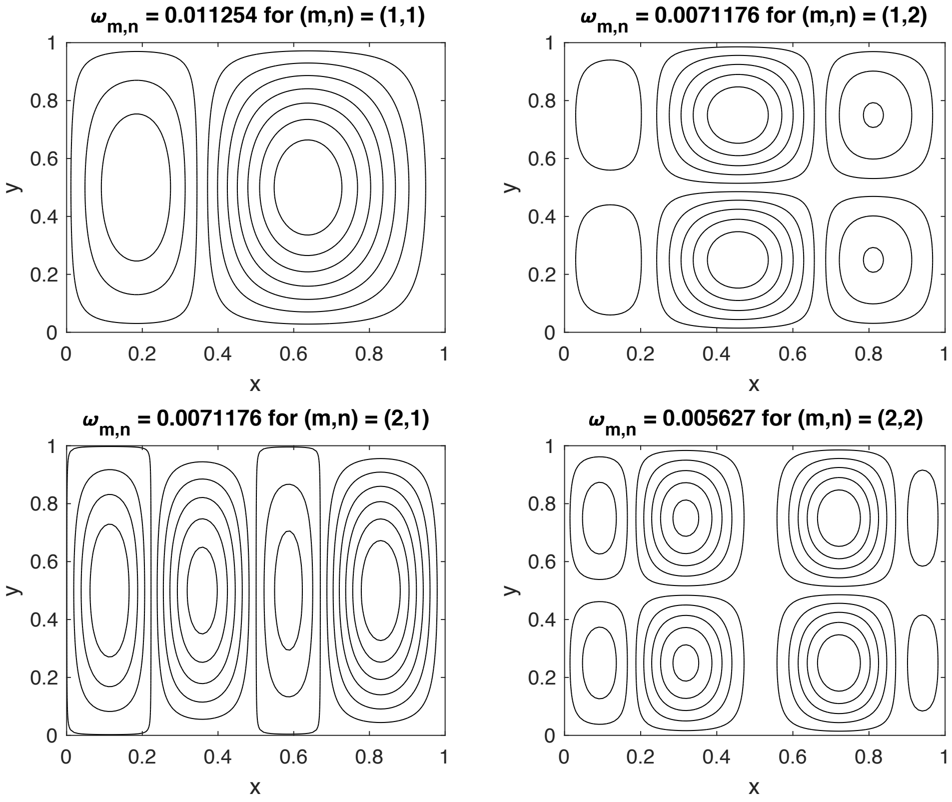

Figure 3.3: The first four modes in the small slope rectangular geometry.

3.2 Container with large slope

Next we introduce a slope that varies linearly in the y-direction in order to determine whether the rectangular shape of the container has a profound impact on the dynamics found in Chapter 2. The modal structure should be highly similar to the small slope case however there will be differences in the way the modes propagate and evolve over time.

3.2.1 Inviscid Case

Reintroducing spatially varying topography into the problem, we can work on the f-plane again and are able to use the TWE from Chapter 2. Again we use a harmonic solution however we note that we are back in the Cartesian frame, so we take $\psi = \phi(x, y)e^{i\omega t}$ in the TWE (2.3.1). Substituting yields the following differential eigenvalue problem on the square $\mathcal{R} := [0, 1] \times [0, 1]$. We work on the square because the lengths have been scaled out of the TWE and can be easily scaled back onto a rectangle if needed.

$$iH_0'\phi_x = -\omega\big[H_0(\phi_{xx} + \phi_{yy}) - H_0'\phi_y\big] \quad \text{in} \quad \mathcal{R}, \tag{3.2.1a}$$

$$\phi = 0 \quad \text{on} \quad \partial\mathcal{R}. \tag{3.2.1b}$$

We will use the same depth profile from Chapter 2 except that it will vary linearly with y instead of r and so we define $H_0(y) = 1 - sy$. The $s = 1/2$ and $s = 1$ cases are considered to determine whether discrete sets of oscillatory modes can exist in either geometry. The geometries we are therefore considering are the two containers depicted in Figure 3.4.

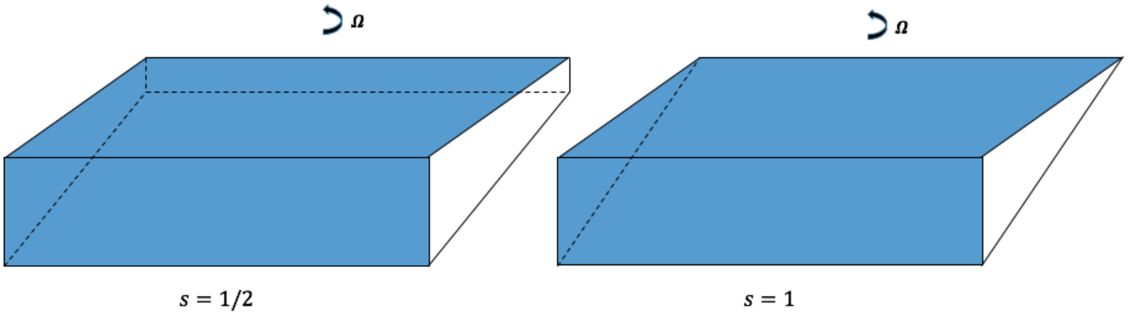

Figure 3.4: The two rectangular containers with differing slopes.

Spectrally discretising as before we obtain the following generalised eigenvalue problem that we can solve in MATLAB.

$$\Big[\text{diag}(iH_0') \otimes D_x\Big]\boldsymbol{\phi} = -\omega\Big[\big(\text{diag}(H_0) \otimes D_{xx}\big) + \dots$$
$$\dots\big(\text{diag}(H_0)D_{yy} \otimes I_{M-1}\big) - \big(\text{diag}(H_0')D_y \otimes I_{M-1}\big)\Big]\boldsymbol{\phi}. \quad (3.2.2)$$

First we run the eigenvalue analysis for the solutions of both cases to determine whether any modes exist in these geometries. The first 500 numerical eigenvalues are plotted in Figure 3.5. Choosing the cutoff value as 20 again the $s = 1/2$ case reveals that over 250 'good' eigenvalues exist so we can proceed with plotting some of these modes (Figure 3.6). They appear to have a very similar structure to the larger modes in the small slope case except that the introduction of a steeper gradient has shifted the streamline pattern from $y = 0.5$ line and into the northward (shallow) direction. This is what was expected and was observed in the half cone case in Chapter 2.

The $s = 1$ case however is very different as it indicates there are many 'good' modes above the cutoff value, however they appear in an almost periodic manner, repeating every 71 modes or so making it difficult to discern a stable set of discrete modes. Recall from Section 2.5 that 71 is the number of collocation points in the spectral discretisation for this problem. It is unclear why this occurs however we plot some of the 'good' modes to determine whether they are truly non-spurious. It would be expected that the larger cells would exist further north in the shallow part of the 'wedge' shaped container however the steep gradient is clearly preventing their existence, see Figure 3.7. The cells do appear to exist in the northern areas however they are very small scale, not large as they should be. Once again we will plot the time-dependent solutions to check these results.

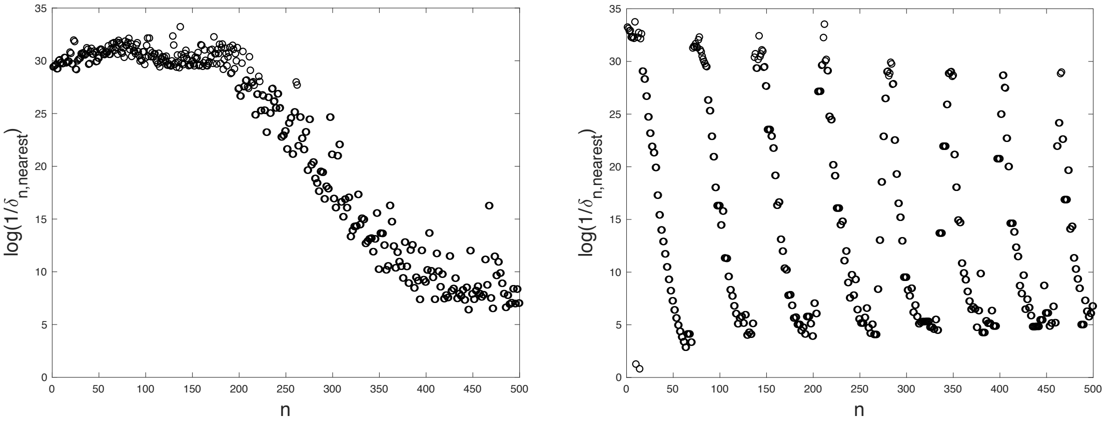

(a) $s = 1/2$ (b) $s = 1$

Figure 3.5: The spurious eigenvalue plots against mode number n for lower spatial resolution $(M, N) = (70, 70)$ and higher resolution $(75, 75)$ in the rectangluar geometries.

As we are still working with the inviscid TWE, the orthogonality relations from Section 2.7 and Appendix A still hold, hence we can construct the superposed solution of 'good' modes in the $s = 1/2$ case. From Chapter 2 we know that in order to plot a solution that captures a high percentage of the total variance, we must superpose a high number of modes. In this case, plotting 50 modes only accounts for 79% of the total variance of all the 'good' modes. Hence we abandon the modal solutions as they do not capture high variance and do not even exist in the $s = 1$ geometry anyway. Instead we compute the time-dependent solutions of (3.2.3) using the same techniques developed before. Plugging $\psi = \psi(x, y, t)$ into (2.3.1) we obtain the following PDE:

$$\frac{\partial}{\partial t}\Big[\frac{1}{H_0}(\psi_{xx} + \psi_{yy}) - \frac{H_0'}{H_0^2}\psi_y\Big] - \frac{H_0'}{H_0^2}\psi_x = 0. \tag{3.2.3}$$

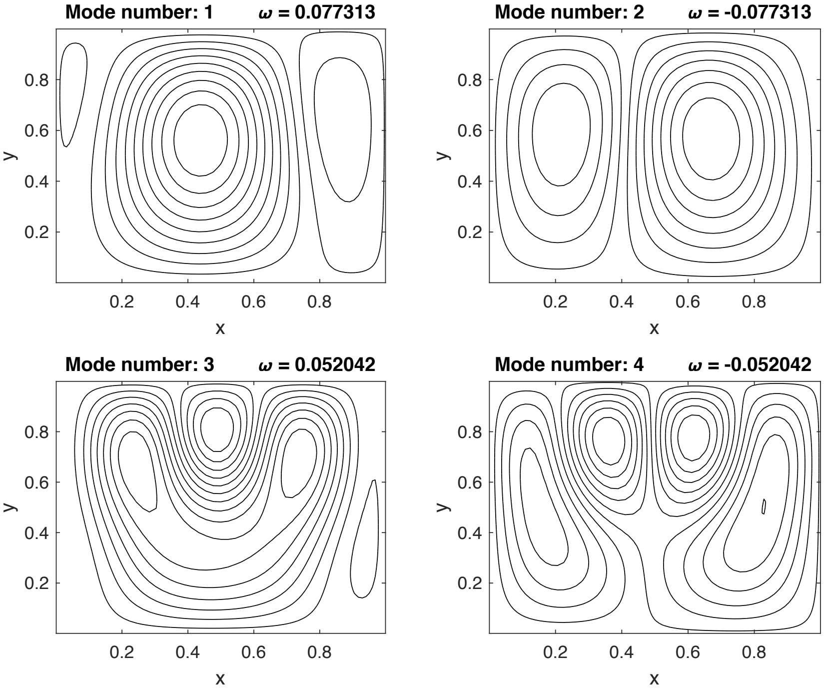

Figure 3.6: The first four modes in the $s = 1/2$ case.

Solving as before, in the $s = 1/2$ geometry, the results in Figure 3.8 show how the initial vortex cell propagates west with a slight bias toward the deeper part of the container. These cells are repeatedly generated near the north-eastern corner and pressed against the south-western lateral walls after propagation. Just as they did in Chapter 2, the cells build on top of each other as the system has no way to dissipate the energy.

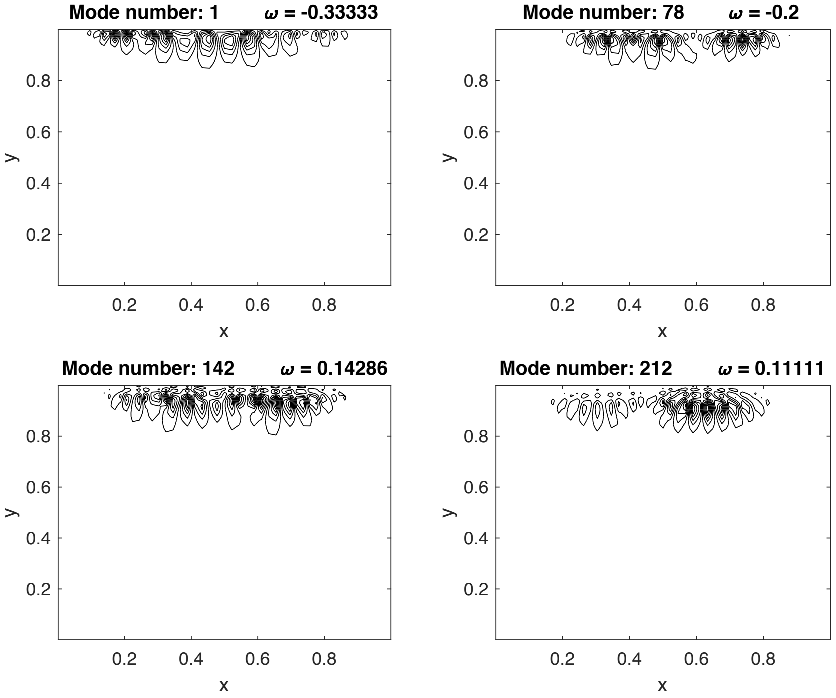

Figure 3.7: Four of the 'best' modes in the $s = 1$ case from the eigenvalue analysis in Figure 3.5b.

The initial gyre in the $s = 1$ case propagates exactly as it does in the $s = 1/2$ case except it sits deeper in the container and converges to the western boundary at a much faster pace due to the steeper slope. The large waves are generated in the north-east corner, propagate to the western wall through deeper fluid before being reflected in the north-west corner as short waves along the shallowest part of the container. This motion periodically repeats as the energy cannot be damped away just as we observed in the inviscid half cone. The reflected wave behaviour is almost identical to that found in the inviscid half cone and occurs as a direct result of the absent viscosity.

This analysis of the inviscid system has shown that the geometry of the container has little to no impact on whether or not a discrete set of normal modes for the system exist. It becomes clear that driving influence derives from taking the gradient of the depth profile to 1. We show in Chapter 4 that because $H_0 = 1 - r$ tends to zero as $r \to 1$, a singularity arises in the integral of the energy function (4.6.2) and hence energy becomes unbounded. No discrete set of modes is able to capture infinite energy and hence no set can exist. This argument holds regardless of the container geometry or whether the problem is inviscid or not, as we shall continue to see.

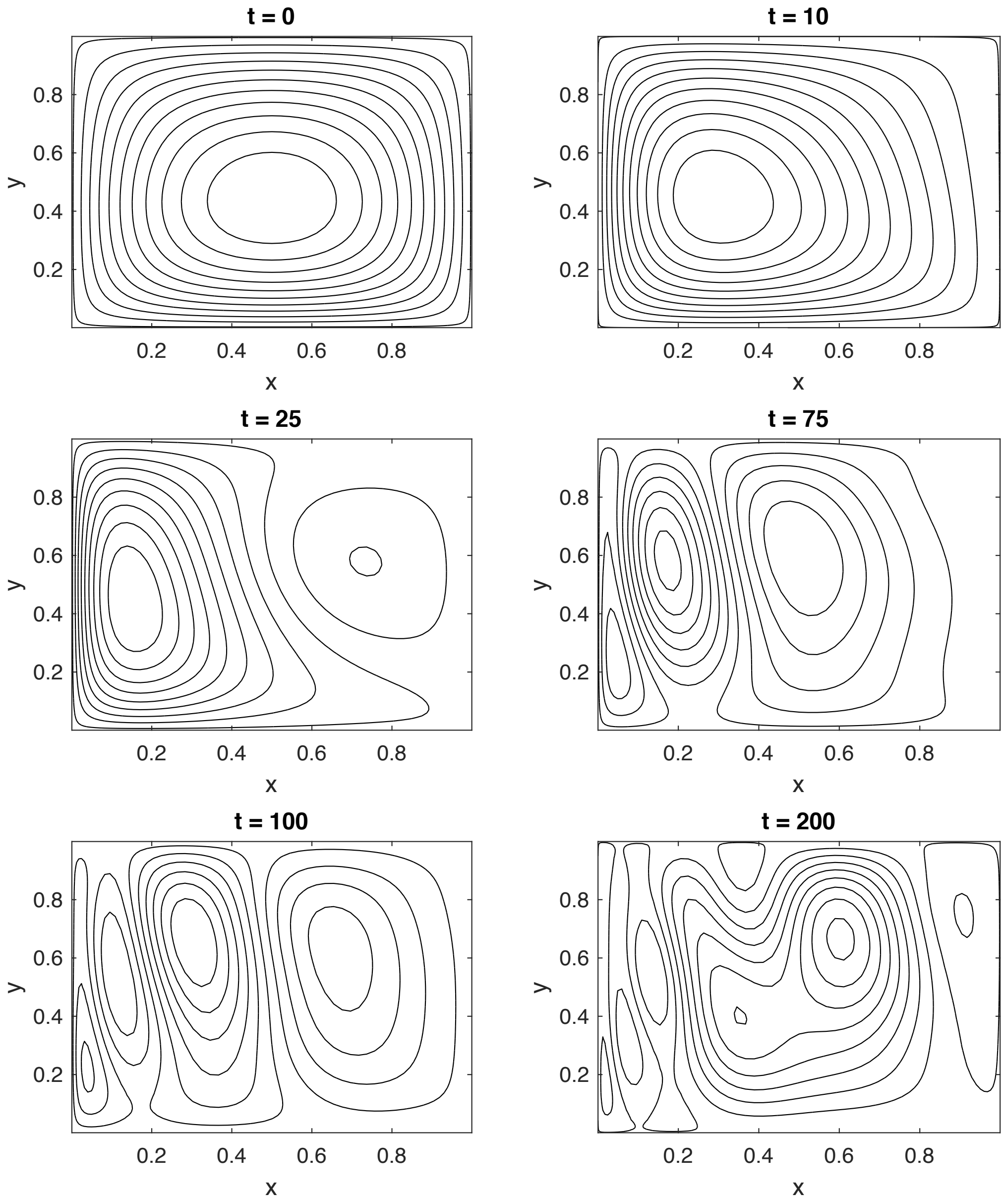

Figure 3.8: Full time-dependent solution for s = 1/2 plotted at contour intervals of 0.005.

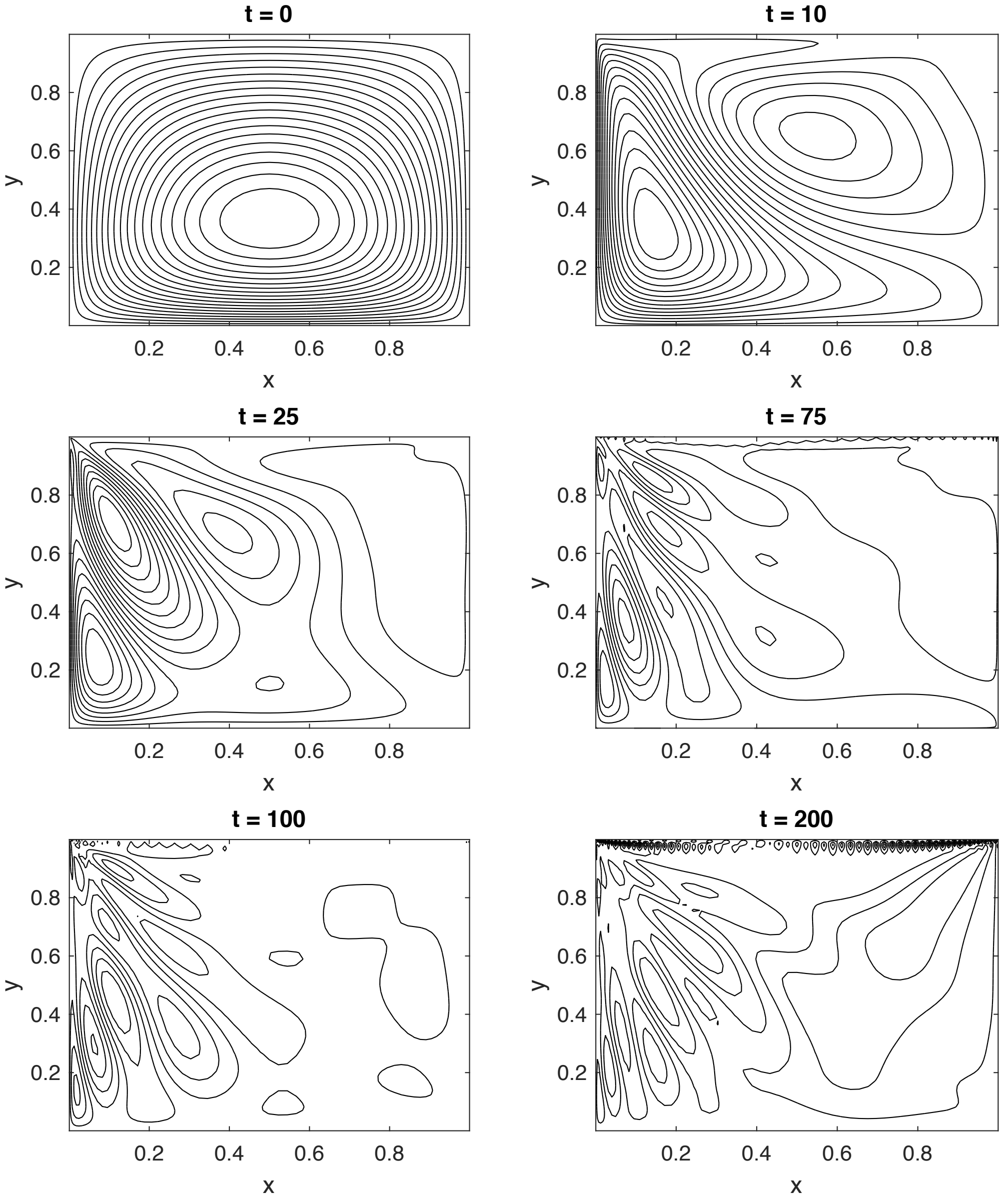

Figure 3.9: Full time-dependent solution for s = 1 plotted at contour intervals of 0.002.

3.2.2 Viscous Case

In this final section we incorporate viscosity into the TWE in order to model how the initial vorticity is destroyed over time by the boundary layers we know to exist near the edges of the container. We test this method in the rectangular container to determine whether it is suitable for the half cone geometry. In order to study the viscous large slope case, we approach the problem as in the previous section but now with the addition of vorticity dissipation in the TWE (2.3.1) derived back in Section 2.3. There are two main ways to approach this:

Approach 1

The simplest method is to include a linear vorticity dissipation term that is proportional to the kinematic viscosity, ν, such that the TWE problem becomes

$$\frac{\partial}{\partial t}\nabla\cdot\left(\frac{\nabla\psi}{H_0}\right)+\hat{\mathbf{z}}\cdot(\nabla\psi\times\nabla\frac{1}{H_0})=-\nu\zeta \quad \text{in} \quad \mathcal{R}, \tag{3.2.4a}$$

$$\psi=0 \qquad \text{on} \quad \partial\mathcal{R}. \tag{3.2.4b}$$

Whilst a valid approach, it would only cause the vorticity generated by the problem in Chapter 2 to decay uniformly across the domain $\mathcal{R}$ at some exponential rate. This is valid, however it would not take into account the geometry of the container in which the vorticity decays. The vorticity should decay faster, almost exclusively, in the boundary layers at the walls and negligibly in the largely inviscid interior of the container. This makes Approach 2 much more appropriate.

Approach 2

A more realistic approach is to scale the damping term by the topography of the container $H_0(y)$. This would mean that dissipation is now stronger toward the shallow end and weaker toward the deeper parts of the container. Adapting (3.2.4), this problem then takes the form

$$\frac{\partial}{\partial t}\nabla\cdot\left(\frac{\nabla\psi}{H_0}\right)+\hat{\mathbf{z}}\cdot(\nabla\psi\times\nabla\frac{1}{H_0})=-\frac{\nu}{H_0}\zeta \quad \text{in} \quad \mathcal{R}, \tag{3.2.5a}$$

$$\psi=0 \qquad \text{on} \quad \partial\mathcal{R}. \tag{3.2.5b}$$

As the TWE is no longer inviscid, the orthogonality results proved in Appendix A no longer hold. Attempting to find similar relations for the viscous equation becomes much more difficult and will most likely be unnecessary as the modal solutions may or may not exist anyway. To check this, we want to identify the non-spurious numerical eigenvalues as before and plot them in Figure 3.10. The kinematic viscosity is set as $\nu=0.01$, large enough to discover the dynamics on a relatively short time scale. It is clear that the $s=1/2$ case is the only one capable of producing non-spurious modes as we have come to expect. The steeper slope once again displays no 'good' modes. Once again, plugging $\psi=\psi(x,y,t)$ into (3.2.5) we obtain:

$$\frac{\partial}{\partial t}\Big[\frac{1}{H_0}(\psi_{xx}+\psi_{yy})-\frac{H_0'}{H_0^2}\psi_y\Big]-\frac{H_0'}{H_0^2}\psi_x=-\nu\Big[\frac{1}{H_0^2}(\psi_{xx}+\psi_{yy})-\frac{H_0'}{H_0^3}\psi_y\Big]. \tag{3.2.6}$$

Before discussing the results we must note that the eigenvalues from both geometries, even though numerically spurious in the $s = 1$ case, now contain a positive imaginary component (see Table 3.1 for the first few eigenvalues). This means that the solutions will now decay over time as required and will do so much more quickly in the $s = 1$ case ($|Im(\omega_n)|$ is larger than in the $s = 1/2$ case). For example if $\omega_n = a_n + ib_n$ for real a and b then

$$\psi=\phi(x,y)e^{i\omega_n t}=\phi(x,y)e^{i(a_n+ib_n)t}=\phi(x,y)e^{ia_nt}e^{-b_nt}. \tag{3.2.7}$$

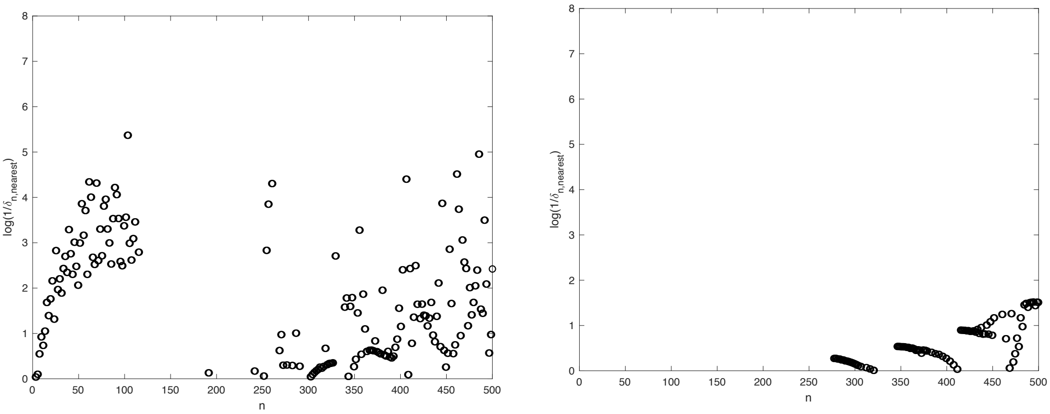

(a) $s = 1/2$

(b) $s = 1$

Figure 3.10: The spurious eigenvalue plots against mode number n for lower spatial resolution $(M, N) = (70, 70)$ and higher resolution $(75, 75)$ in the viscous rectangular container.

Mode (n)	ω_n	Mode (n)	ω_n
1	0.0772 + 0.0144i	1	0.2578 + 19.8943i
2	-0.0772 + 0.0144i	2	-0.2578 + 19.8943i
3	0.0519 + 0.0154i	3	0.2579 + 19.8301i
4	-0.0519 + 0.0154i	4	-0.2579 + 19.8301i
5	0.0471 + 0.0140i	5	0.1519 + 19.8798i
6	-0.0471 + 0.0140i	6	-0.1519 + 19.8798i

Table 3.1: The first six numerical eigenvalues, rounded to 4 decimal places, in the $s = 1/2$ (left) and $s = 1$ rectangular geometries (right).

Once again we solve (3.2.6) using the spectral method and the ODE solvers to create the solutions in Figures 3.11 and 3.12. The resulting flow was categorised by van Heijst et al. for spin-up in non-axisymmetric containers in [16]. They discuss the flow in rectangular containers and determined that:

1. Starting flow has zero absolute vorticity (we know this as the rigid body rotation prior to spin-up/down).

2. Flow separates due to cyclonic vorticity generation at the lateral walls.

3. The flow is organised into regular anticyclonic and cyclonic cell patterns followed by viscous decay due to the Ekman layer at the container base.

Using these stages as a guide we analyse the numerical findings for the $s = 1/2$ and $s = 1$ geometries. The numerical results given in Figures 3.11 and 3.12 show, at $t = 0$, the initial flow taking the form of a large scale cyclonic cell generated by the instantaneous spin-down as expected. Alternating cyclonic and anticyclonic cells are generated at the eastern lateral walls over the next few time steps too. It is unclear in the snapshots (clearer in the animation files) that the cells generated at the walls do not merge at any point during their evolution. Much like the inviscid case, the cells in full slope case propagate much faster to the western wall than in the half slope case. The flow is organised into regular cell patterns as predicted however the viscous decay quickly causes the cells to dissipate and hence the waves are too weak to be reflected at the western wall. It is difficult to explicitly see how the boundary layers on the container bottom are damping the vorticity however it is more than feasible that Ekman pumping causes the majority of the fluid spin-down. A portion of the spin-down is certainly carried out by the vertical boundary layers on the lateral walls however this is difficult to quantify or observe from two-dimensional plots.

From these results and the eigenvalue analysis, it is now clear that the geometry of the container has no impact on whether oscillatory modes exist or not. Both the half cone and rectangular geometries with slope $s = 1/2$ contain modes and yet as we take each slope to $s = 1$ it becomes clear that the determining factor is whether the depth of the container goes to zero at any point. The dynamics observed in the inviscid rectangular container are strikingly similar to the half cone, hence we expect to find similar results in the viscous case.

Next we can directly compare the viscous results for the half cone with those in [22] and determine whether there is anything markedly different using the TWE to simulate linear spin-down.

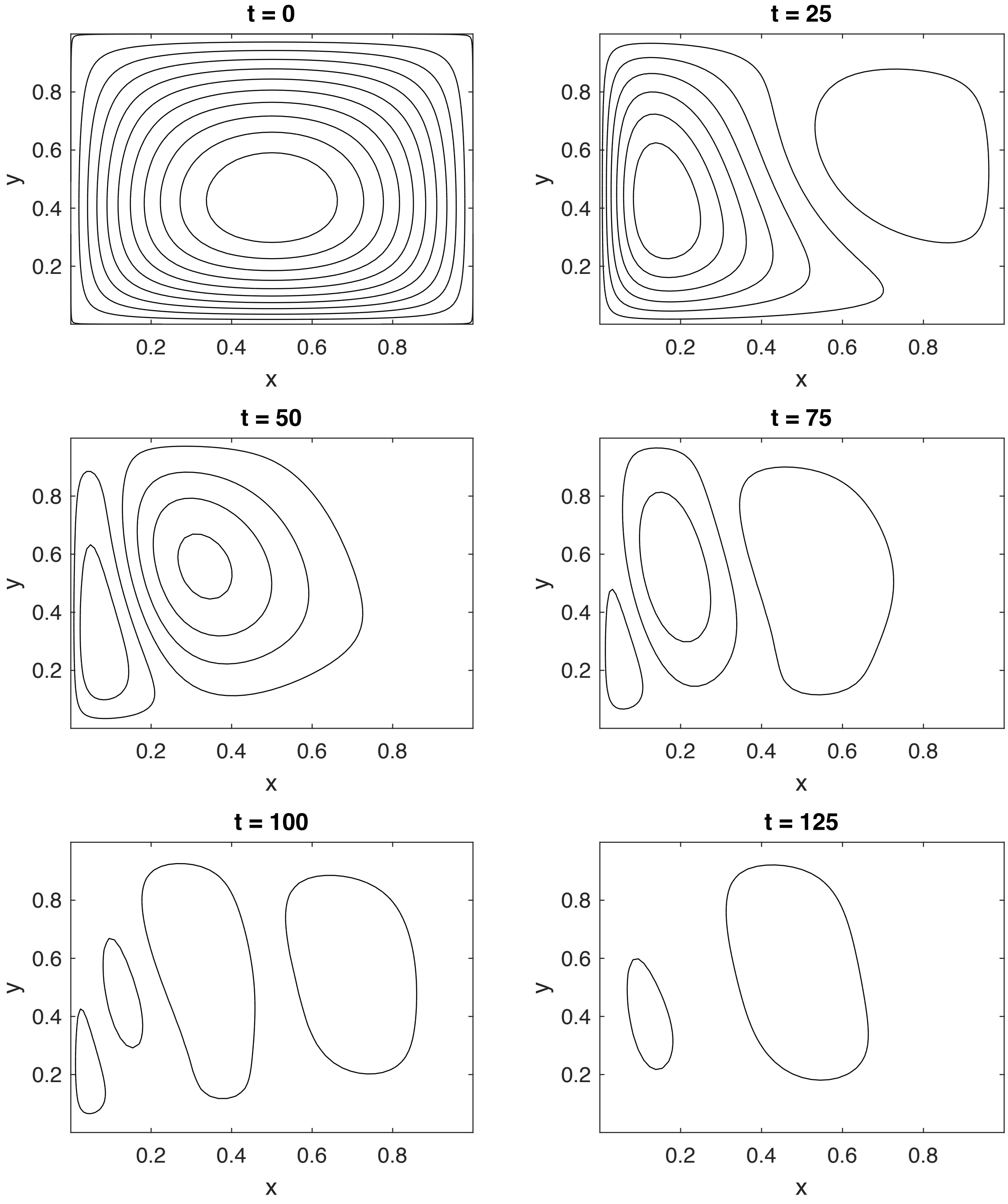

Figure 3.11: Full time-dependent solution for s = 1/2 plotted at contour intervals of 0.005.

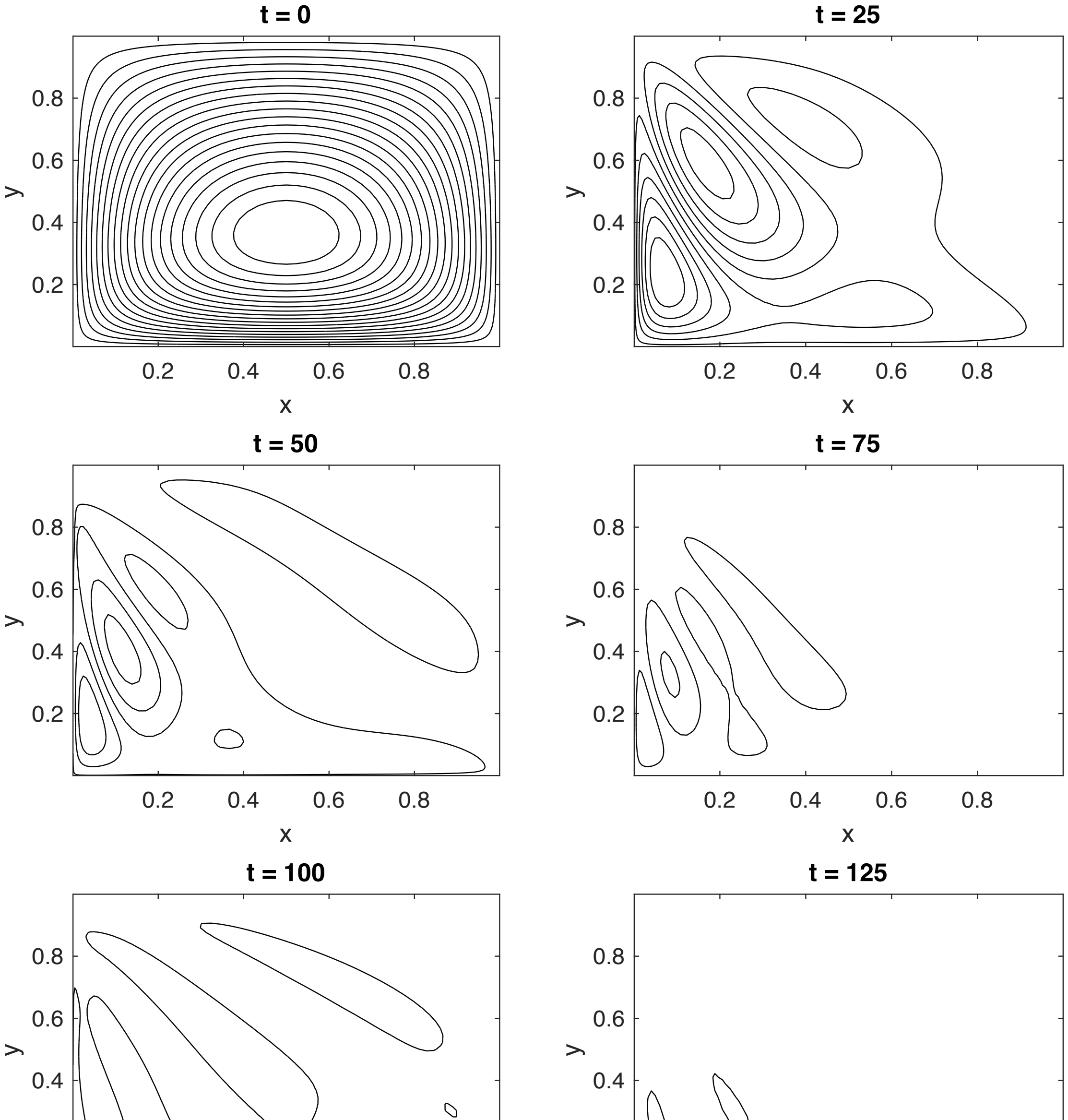

Figure 3.12: Full time-dependent solution for s = 1 plotted at contour intervals of 0.002.

Chapter 4

Viscous Fluid Spin-Down in a Half Cone

We are finally in a position to solve the fully viscous problem in the rotating half cone using the methods outlined in Chapters 2 and 3. Having analysed the comparable rectangular problem in Chapter 3, we have a good understanding of the type of streamline patterns that will emerge from the numerical results in this case. Firstly we form the problem and briefly discuss the eigenvalue analysis. We then move on to simulating the time-dependent solutions and analyse the resulting transient behaviour of the spin-down and its viscous decay. These solutions are then used to determine other properties of the flow such as the kinetic energy and vertical viscosity, ready to compare with the results generated by Li et al. in [22]. We conclude with a discussion on what we have found and any markedly different results.

4.1 Problem Formulation

Looking back to Section 3.2.2 we adopt the same method (Approach 2) to include viscosity in the TWE: scaling the linear decay of vorticity with the topography of the half cone. This creates higher dissipation near the outer rim of the half cone ($r = 1$) and much lower dissipation near the centre ($r = 0$). We take problem (3.2.5) and pose it over the semi-circular domain V instead of the rectangle $\mathcal{R}$ such that

$$\frac{\partial}{\partial t}\nabla \cdot \left(\frac{\nabla\psi}{H_0}\right) + \hat{\mathbf{z}} \cdot (\nabla\psi \times \nabla\frac{1}{H_0}) = -\frac{\nu}{H_0}\nabla \cdot \left(\frac{\nabla\psi}{H_0}\right) \quad \text{in} \quad V, \tag{4.1.1a}$$

$$\psi = 0 \qquad \text{on} \quad \partial V. \tag{4.1.1b}$$

4.2 Spectral Analysis

The differential eigenvalue problem can be converted into the form $A\phi = \omega B\phi$ as before, using the usual spectral discretisation methods[1]. The problem is evaluated with the same number of Chebyshev points as the inviscid problem and we include the same kinematic viscosity value $\nu = 0.01$ for the fluid. The numerical results from the spurious eigenvalue analysis are graphed in Figure 4.1. The half cylinder, again, demonstrates it contains a finite set of normal modes whereas the half cone cannot, as we know, due to the unbounded energy. The eigenvalues now also contain positive imaginary parts, see Table 4.1 for the largest (absolute real part) eigenvalues in both cases, meaning viscous decay is now present in the system. Note that even though the $s = 1$ eigenvalues in Table 4.1 are spurious, their imaginary components are much larger in magnitude than the $s = 1/2$ values indicating that decay in the half cone is much faster than in the half cylinder.

The structure of the 'good' and 'bad' modes in both cases are very similar, if not identical, to those in the inviscid problem except that they now decay. Again, we do not plot any superposed modes and instead study the time-dependent solutions in more detail.

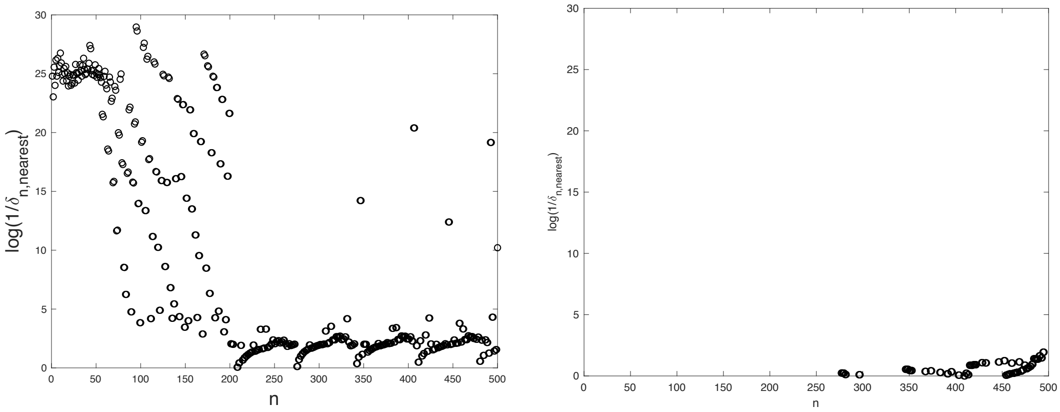

(a) $s = 1/2$

(b) $s = 1$

Figure 4.1: The ratio $log(1/\delta_{n,nearest})$ against mode number n for lower spatial resolution $(M, N) = (70, 70)$ and higher resolution $(75, 75)$ in the topography cases $s = 1/2$ and $s = 1$.

---

[1] The code for the viscous problem is identical to that of the inviscid problem in Appendix B.2 with modifications only to the matrix operators `A` and `B`.

Mode (n)	ω_n	Mode (n)	ω_n
1	-0.0836 + 0.0143i	1	0.1044 + 19.8381i
2	0.0836 + 0.0143i	2	-0.1044 + 19.8381i
3	-0.0711 + 0.0151i	3	0.1044 + 19.8863i
4	0.0711 + 0.0151i	4	-0.1044 + 19.8863i
5	-0.0614 + 0.0157i	5	0.0530 + 19.8546i
6	0.0614 + 0.0157i	6	-0.0530 + 19.8546i

Table 4.1: The first six numerical eigenvalues, rounded to 4 decimal places, in the $s = 1/2$ (left) and $s = 1$ geometries (right).

4.3 Time-dependent Solutions

The viscous time-dependent problem (4.1.1) with initial condition (2.7.1) is solved exactly as before using $\psi = \psi(r, \theta, t)$. This gives the problem

$$\frac{\partial}{\partial t}\big(r^2 H_0^2 \psi_{rr} + (r H_0^2 - r^2 H_0' H_0)\psi_r + H_0^2 \psi_{\theta\theta}\big) = -r H_0' H_0 \psi_\theta - \dots$$
$$\nu\big(r^2 H_0 \psi_{rr} + (r H_0 - r^2 H_0')\psi_r + H_0 \psi_{\theta\theta}\big). \quad (4.3.1)$$

The streamlines at different points in time for both cases are plotted in Figures 4.2 and 4.3. Just as Li et al. observe in [22, Fig.3], we see the starting vortex in both cases migrate toward the western corner of the container - much more rapidly in the half cone case. Note that even though Li et al. plot [22, Fig.3] in the spin-up case, they determine that for linear spin-up/down ($|Ro| \leq 0.05$), the dynamics are the identical except that the signs of the velocity vector (and hence the streamfunction) are reversed. Once on the south-western wall, the cells build on top of each other in quick succession before they are continually spun-down by the Ekman layers, hence no longer reflecting back east. Li et al. state that most of the spin-up/down is caused in the boundary layer located on the sloping bottom of the container however it is difficult to see why the south-western lateral wall was neglected from this argument as it must have an impact on the viscous decay. Again it is difficult to discern this from the two-dimensional plots in Figures 4.2 and 4.3. Although we cannot see it, Li et al. state that there appears to be little to no impact from the horizontal Ekman layer on the rigid lid either.

Using just the streamfunction ψ we now calculate and discuss the vertical vorticity, the energy decay and other features of the flow mentioned in Li et al.

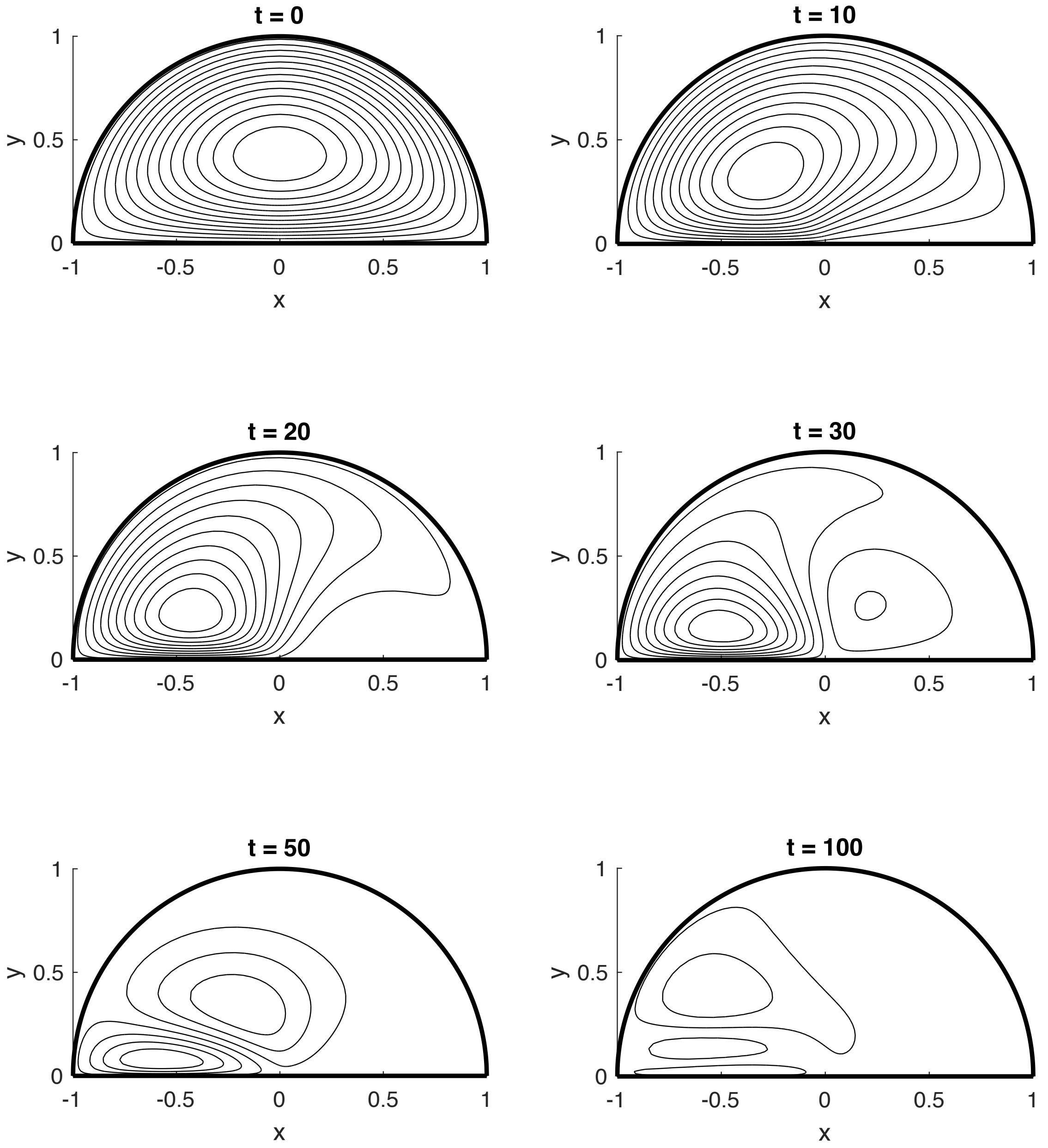

Figure 4.2: Full viscous time-dependent solution for s = 1/2. Contours plotted at a distance of 0.005 from each other.

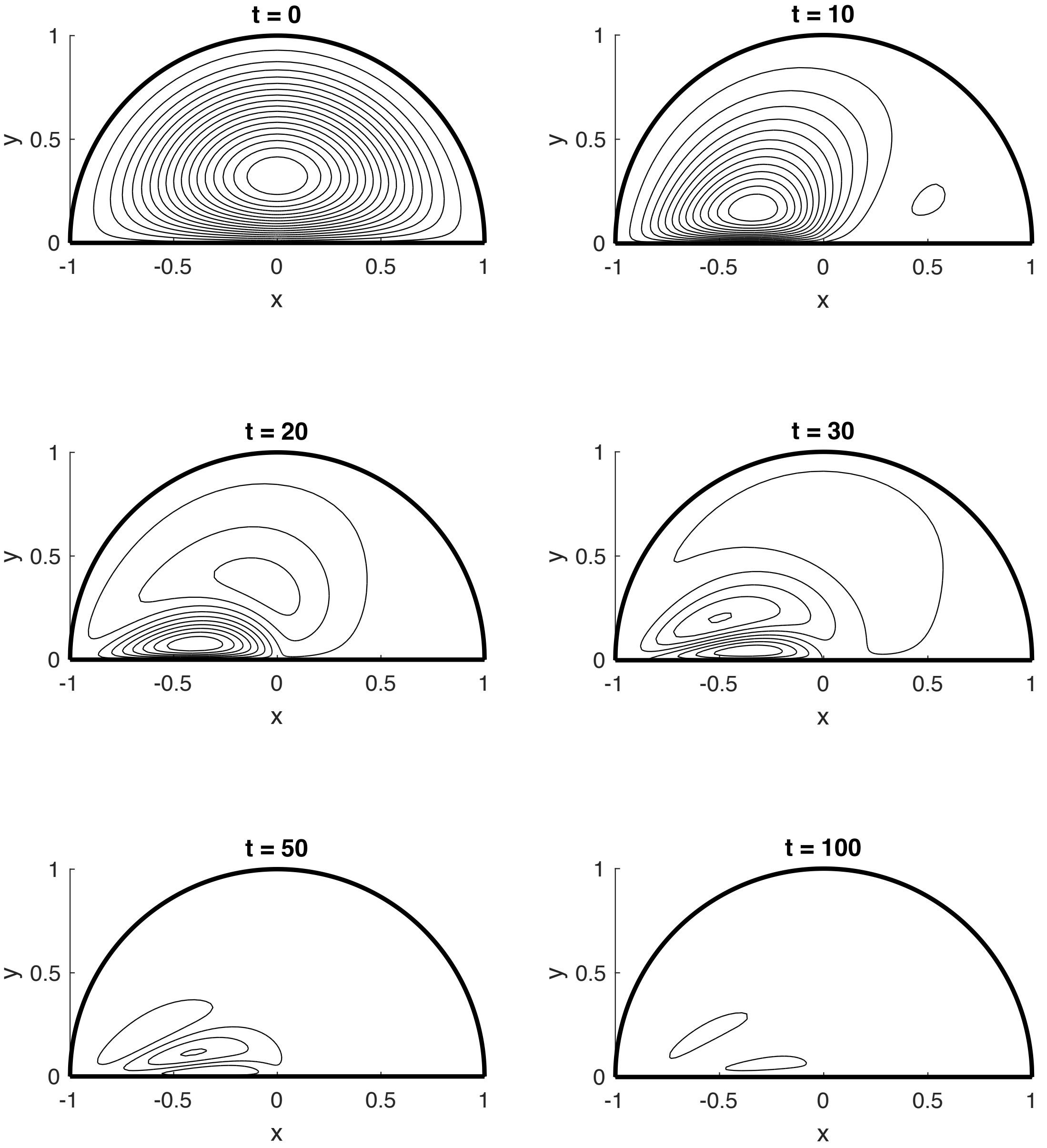

Figure 4.3: Full viscous time-dependent solution for s = 1. Contours plotted at a distance of 0.002 from each other.

4.4 Vertical vorticity

Now that we know the time-dependent solutions for ψ it is simple enough to plot the vertical vorticity ζ over time by differentiating using spectral matrices once again. We know that vertical vorticity is defined as (2.2.6), hence we may write it in terms of polar derivatives and differentiate spectrally at each t such that

$$\zeta(t) = \nabla \cdot \big(\frac{1}{H_0}\nabla\psi\big) = \frac{1}{r}\big(\frac{r}{H_0}\psi_r\big)_r + \frac{1}{r^2 H_0}\psi_{\theta\theta} \quad \rightarrow \quad \boldsymbol{\zeta}(t) = L\boldsymbol{\psi}, \tag{4.4.1}$$

where L is a matrix operator (detailed in Appendix B.6) and $\boldsymbol{\psi}$ is the known streamfunction vector. Solving this system for each time t we plot the vorticity at different times in Figure 4.4 (left). Now we can directly compare these vertical vorticity results generated by the spin-down to the isolines from [22, Fig.13] in Figure 4.4 (right). The half cone displays exactly what we expect to see at time zero: spin-down generating zero (almost negative) vorticity in a thin layer very close to the boundary wall whilst positive cyclonic vorticity is generated as the (largely inviscid) interior of the cone continues to rotate. At $t > 0$ the container is rotating uniformly once again, hence we see the areas of positive vorticity migrate toward the western boundary as expected and build up with smaller areas of negative vorticity. Note that viscosity in [22] is lower than $\nu = 0.01$, hence the convergence and dissipation occur much faster even though the plots are shown at the same time points (except $t = 0$ which is not plotted in [22]). As time progresses further, these areas of cyclonic and anticyclonic vorticity are destroyed by the viscous boundary layers in the system. These results were very straightforward to calculate using minimal computational effort and confirm the results seen in [22]. The spin-up case can be plotted, except that the vorticity would be reversed, initially negative within the interior of the flow, propagating and dissipating in the same way as the spin-down.

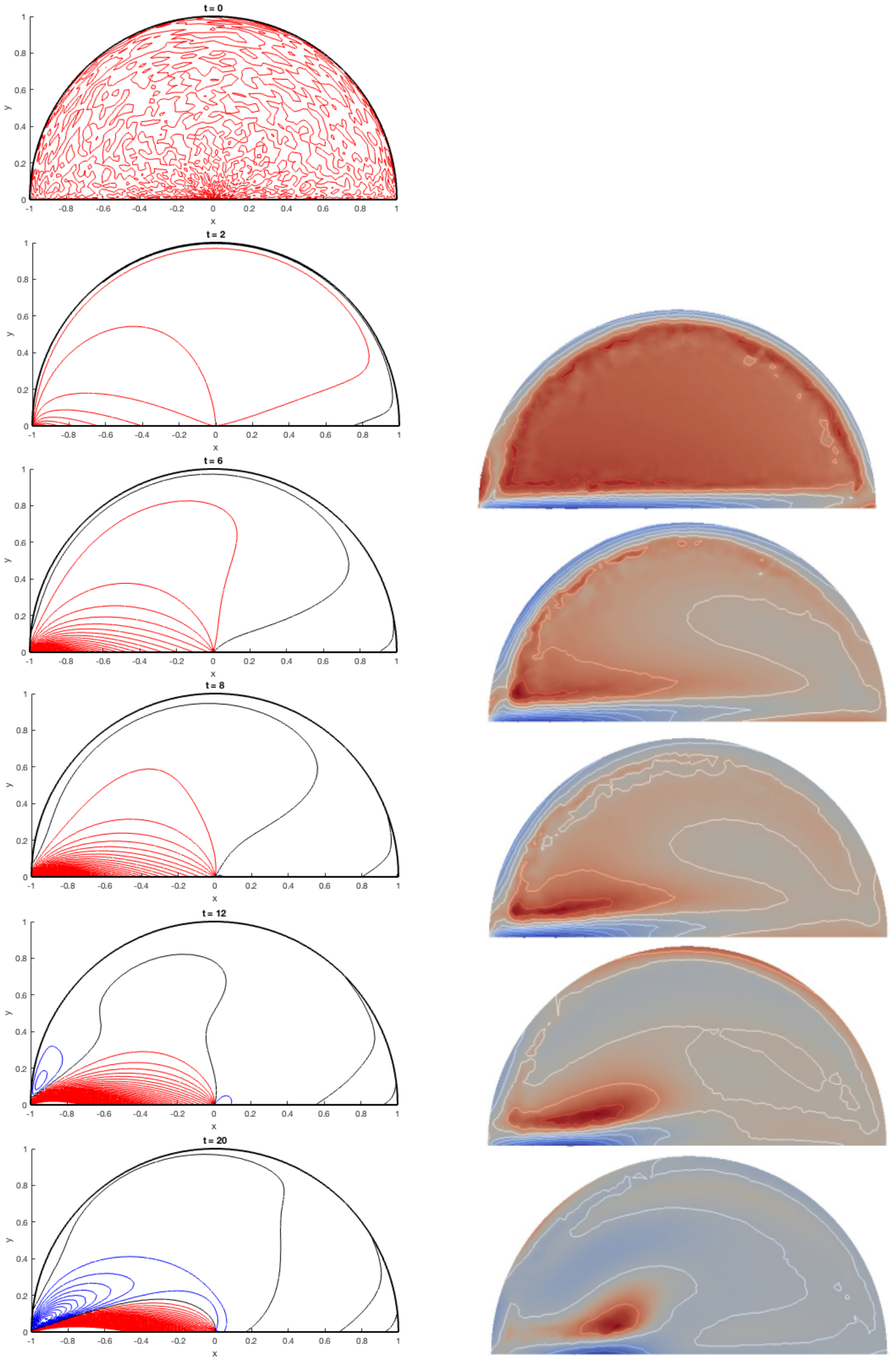

(a) (b)

Figure 4.4: Viscous time-dependent vertical vorticity in the half cone ($s = 1$). Contours of positive, negative and zero vorticity are plotted in red, blue and black (white in (b)) respectively. (a) Results from (4.4.1), values range from $[-25, 25]$ at intervals of 0.2. (b) Isoline results at $z = 0.6$ and $Ro = -0.1$ from [22], values range from $[-21, 9]$.

4.5 Vertical Velocity

Another feature of the flow we can plot is the vertical velocity. As vertical velocity is excluded from the shallow water equations we go back to the governing Navier-Stokes equation and use the continuity equation. The derivation is as follows (where $\boldsymbol{u}$ is the horizontal velocity vector still)

$$u_x + v_y + w_z = 0 \quad \Rightarrow \quad w_z = -\nabla \cdot \boldsymbol{u}, \tag{4.5.1}$$

$$\int_z^0 w_z \, dz = -\int_z^0 \nabla \cdot \boldsymbol{u} \, dz \quad \Rightarrow \quad \underbrace{w(0)}_{=0} - w(z) = -(0 - z)\nabla \cdot \boldsymbol{u}. \tag{4.5.2}$$

The vertical velocity must be zero at $z = 0$ because of the rigid lid assumption and hence we can use some vector calculus rules to manipulate the previous expression to obtain

$$w(z) = -\frac{zH_0}{H_0}\nabla \cdot \boldsymbol{u} \quad \Rightarrow \quad w(z) = \frac{z}{H_0^2}(\hat{\boldsymbol{z}} \times \nabla\psi) \cdot \nabla H_0, \tag{4.5.3}$$

$$w(z) = -z \; \hat{\boldsymbol{z}} \cdot \big(\nabla\psi \times \nabla(\frac{1}{H_0})\big) \quad \Rightarrow \quad w(z) = -z\frac{H_0'}{rH_0^2}\psi_\theta. \tag{4.5.4}$$

Using this final expression we can plot the resulting vertical velocity for the spin-down problem at $z = -0.6$. Recalling that Li et al. show spin-up and spin-down dynamics are the same for $|Ro| \leq 0.05$, we can directly compare with the spin-up vertical velocity from [22, Fig.5], remembering the colours would be reversed for spin-down. These results are plotted in Figure 4.5 at times $t = [0, 2, 6, 8, 12, 20]$ ($t = 0$ not plotted in [22, Fig.5]) and the results appear to show excellent agreement with each other[2].

Initial velocity generated by the spin-down appears perfectly split down the y-axis with equal but opposite sign in each half. As time progresses the areas of positive velocity propagate westward and encroach further and further until the area of negative velocity is surrounded. At the same time, viscous effects are reducing the strength of the velocities toward zero. In the next section we quantify this rate of decay by finding the energy of the systems.

---

[2] The code used is identical to `vertical_vorticity.m` except the linear operator `L` is adapted.

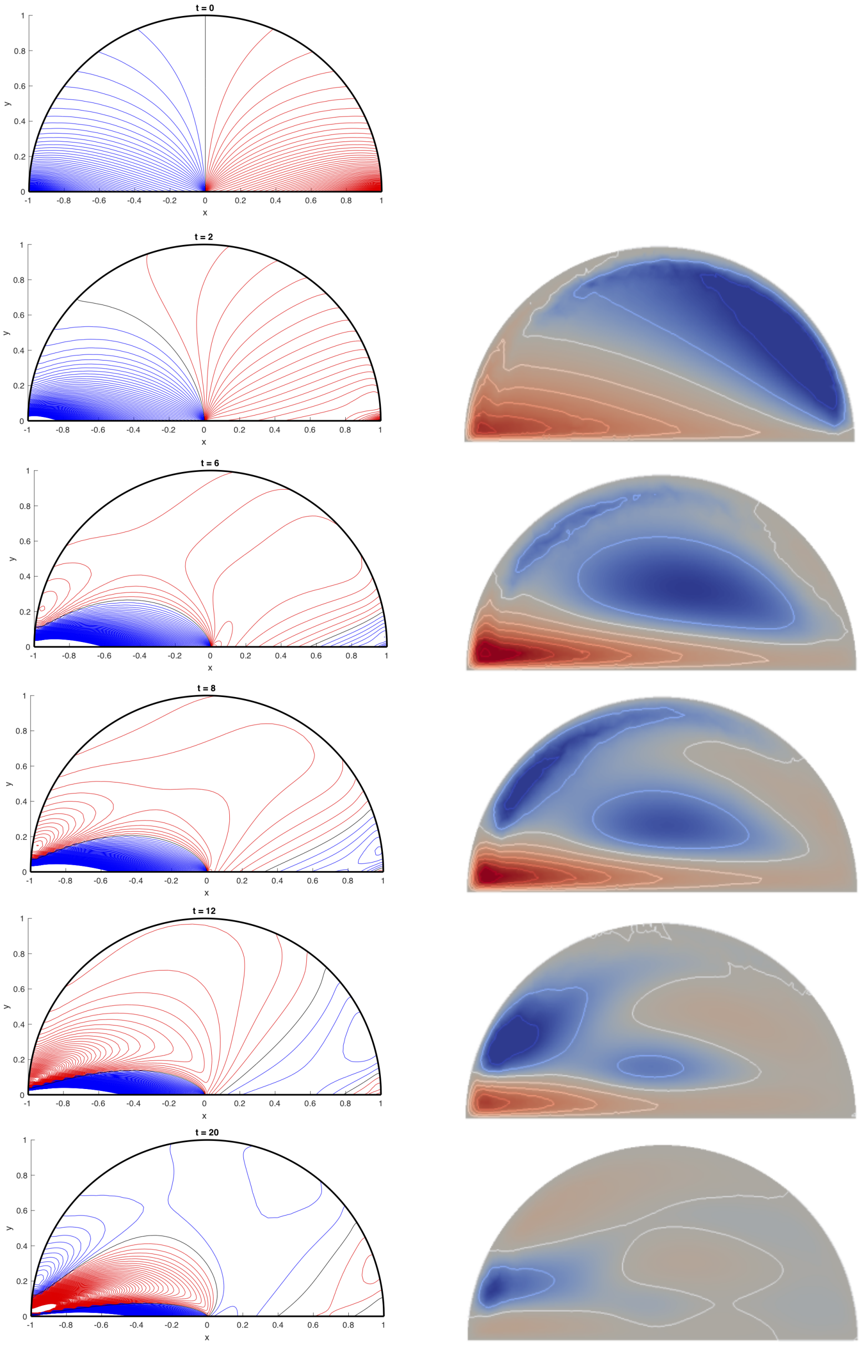

(a) (b)

Figure 4.5: Viscous time-dependent vertical velocity in the half cone ($s = 1$). Contours of positive, negative and zero vorticity are plotted in red, blue and black (white in (b)) respectively. (a) Results from (4.5.4) at $z = -0.6$, values range from $[-1, 1]$ at intervals of 0.01. (b) Isoline results at $z = 0.6$ and $Ro = 0.01$ from [22], values range from $[-0.15, 0.35]$.

4.6 Energy Decay

Li et al. calculate the "speed of adjustment" [22], or the time at which spin-up/down is concluded, as the time taken, t_N, for the kinetic energy of the system to drop to $1/N$th of its initial value. More formally they define the following integral over the full three-dimensional half cone as

$$\frac{\int_{\bar{V}} |\boldsymbol{u}(t_N)|^2 \, d\bar{V}}{\int_{\bar{V}} |\boldsymbol{u}(0)|^2 \, d\bar{V}} = \frac{1}{N}, \tag{4.6.1}$$

where $\boldsymbol{u}$ is the three-dimensional velocity vector and $\bar{V}$ the half cone defined in Section 2.1. They identify a linear relationship between t_N and the Ekman spin-up scale $E^{-1/2}$ and more specifically they find that $t_{100} \approx 0.1520E^{-1/2}$ and $t_{1000} \approx 0.2368E^{-1/2}$, see Figure 4.6. The equivalent integral in the half cone under the shallow water assumption can be simplified by separating the z-derivative from the semi-circular domain V:

$$\int_V \int_{h_b}^{0} |\boldsymbol{u}(t_N)|^2 \, dz dV = \int_V \underbrace{(0 - h_b)}_{=H_0} |\boldsymbol{u}(t_N)|^2 \, dV = \int_V \frac{1}{H_0} |\nabla\psi|^2 \, dV = \langle \psi, \psi \rangle. \tag{4.6.2}$$

Recalling that $H_0(x, y) = -h_b(x, y)$, $\boldsymbol{u} = (-\psi_\theta/r, \psi_r)/H_0$ is two-dimensional in V and the final term $\langle \psi, \psi \rangle$ is just the energy norm from Appendix A. The final integral is straight forward to calculate, however a singularity arises in the integral around the rim of the half cone and hence the energy becomes unbounded. Considering the integral of the following identity we can calculate the energy at any time as a product of the vorticity ζ and the streamfunction ψ. Using just the divergence theorem and the boundary condition on ψ we get

$$\underbrace{\int_V \nabla \cdot \big(\frac{\psi}{H_0} \nabla\psi\big) \, dv}_{=0} = \int_V \psi \nabla \cdot \big(\frac{1}{H_0} \nabla\psi\big) + \frac{1}{H_0} |\nabla\psi|^2 \, dV \quad \Rightarrow \tag{4.6.3}$$

$$-\int_V \psi\zeta \, dV = \int_V \frac{1}{H_0} |\nabla\psi|^2 \, dV = \langle \psi, \psi \rangle. \tag{4.6.4}$$

We plot the value of the energy integrals against (log) time for various values of ν in Figure 4.6. Obviously the higher the kinematic viscosity, the faster the rate of energy decay. The decay times ("speeds of adjustment") are located at the intersections of the red dashed lines and the decay plots. We plot these times against the Ekman decay scale $E^{-1/2}$ in Figure 4.8 for three adjustment times t_2 (black), t_{10} (red) and t_{100} (blue) respectively. The Ekman number with length and Coriolis parameter both equal to one is simply:

$$E = \frac{2\nu}{L^2 f} = 2\nu \quad \Rightarrow \quad E^{-1/2} = \frac{1}{\sqrt{2\nu}}. \tag{4.6.5}$$

Just as Li et al. do, we find there is a linear relationship between the two quantities and hence, by averaging ratios of each slope in $s = 1$ with the corresponding slope in $s = 1/2$, the viscous energy decay in the half cone occurs 4.13 times faster than in the half cylinder with slope. This demonstrates the impact that an increasingly steep slope has on the speed at which the spin-up/down is concluded. Physically, though difficult to show numerically, this shows that Ekman pumping on the base of the container has a greater effect on spin-up/down than on the lateral walls - in which the $s = 1/2$ geometry has a higher proportion of.

Li et al. compare the viscous decay in the half cone with that in the full cone geometry showing that spin-up occurs around 4 times faster in the half cone. The reasoning they give for this is unclear however it is clear the non-axisymmetric nature of the half cone, particularly the south lateral walls, have a dramatic impact on the energy decay. Hence it cannot be excluded when discussing Ekman pumping.

In comparison, the rectangular geometry from Chapter 3 decays approximately 3.43 times faster in the $s = 1$ case than in the $s = 1/2$, see Figure 4.9. This clearly demonstrates that the leading order impact of depth going to zero is the major factor driving the increased rates of viscous decay and shows that container geometry is not as important.

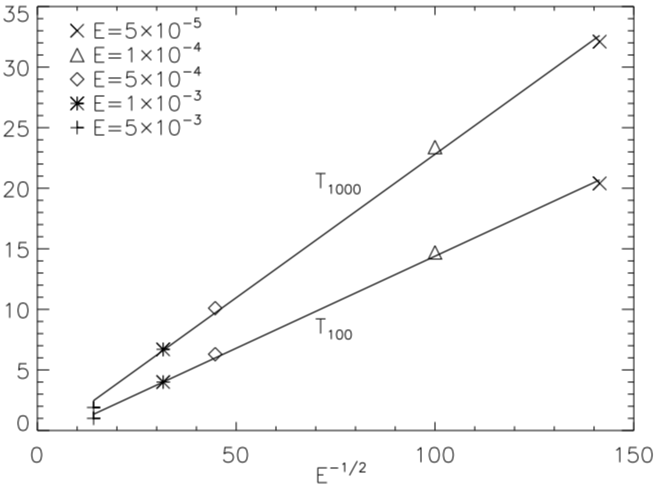

Figure 4.6: Energy decay times against varying Ekman spin-up time $E^{-1/2}$ for t_{100} and t_{1000} - from [22, Fig.6].

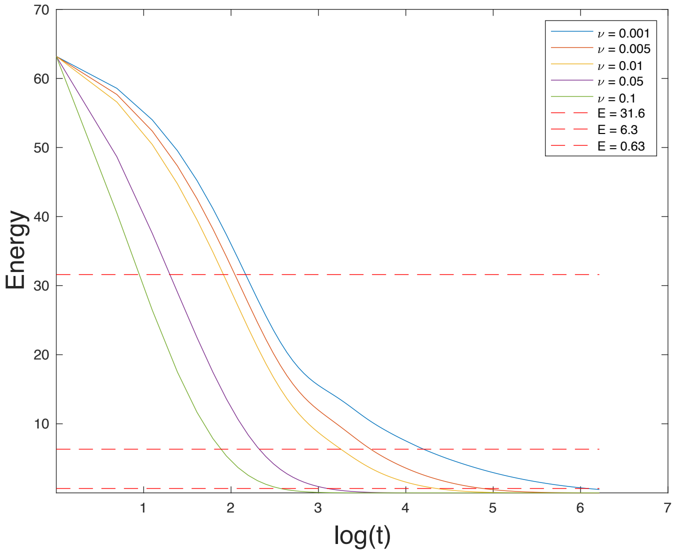

Figure 4.7: The energy decay over time in the viscous half cone, plotted for various $\nu = [0.001, 0.005, 0.01, 0.05, 0.1]$. The dashed red lines indicate the time at which when the energy has dropped to 50% (t_2), 10% (t_{10}) and 1% (t_{100}) of its initial value.

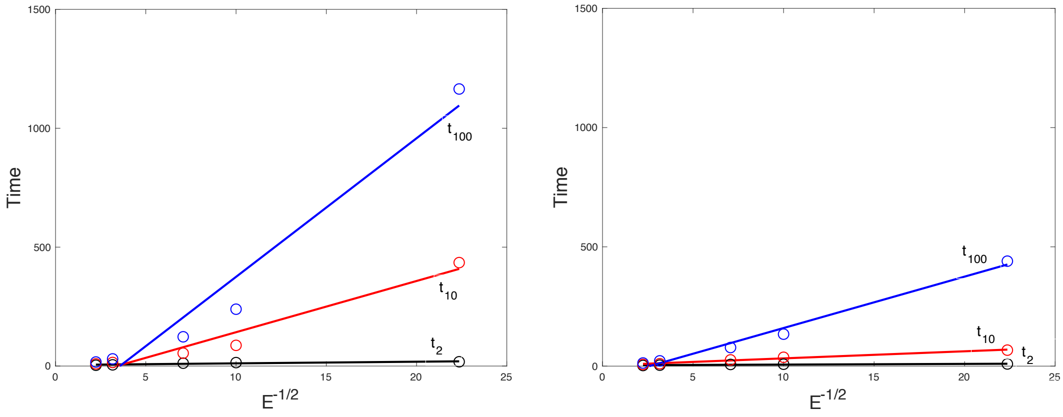

(a) $s = 1/2$

(b) $s = 1$

Figure 4.8: The linear relationship between decay times t_N and increasing $E^{-1/2}$ for $E = [0.002, 0.01, 0.02, 0.1, 0.2]$ in the half cylinder and cone geometries. Straight lines have been fitted against each set of times for t_2, t_{10} and t_{100} respectively.

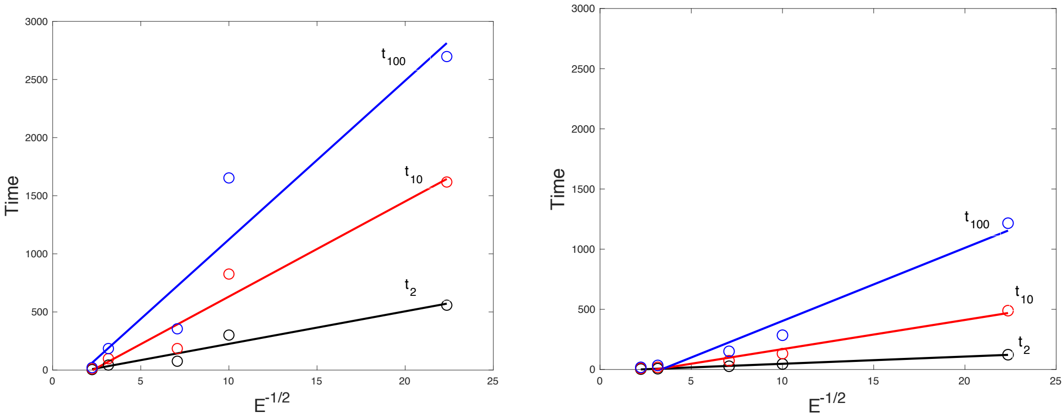

(a) $s = 1/2$ (b) $s = 1$

Figure 4.9: The same plots as 4.8 for the rectangular geometries ($s = 1/2$ and $s = 1$) detailed in Chapter 3.

Chapter 5

Conclusions

To summarise, the main aims of this study were to:

1. Reproduce and confirm the results of linear spin-down from [22] using theory from geophysical fluid dynamics and to reduce the computational effort required to solve the problem.
2. Determine whether any of the results are significantly different from those found in [22] and for what reasons.

In Chapter 2 we derived the governing equations for the problem and introduced the methods needed to solve the inviscid TWE in a half cone as both an eigenvalue problem and via a full integration. We then verified the claim in [22] that no oscillatory modes would exist in the half cone geometry ($s = 1$) however found that they do in the half cylinder with sloping bottom ($s = 1/2$). The numerical results generated via the spectral method (in both cases) then confirmed that topographic waves propagate to the west before being reflected as short waves back round to the east. The energy generated by the initial spin-down vortex has no way of leaving the half cone and hence oscillates periodically around the container.

Moving to Chapter 3, we discussed the same problem in a rectangular container with linearly sloping bottom and found that this geometry follows almost exactly the same dynamics as the cone in the inviscid case. However once viscosity is included the eigenvalues of the system gain an imaginary component and hence the waves generated begin to dissipate over time. The time at which this decay occurred was clearly much faster in the large slope case due to the dominating effect of the steeper topography. The waves no longer reflected at the south-western boundary but instead hit the wall and dissipated shortly after. It was shown that oscillatory modes cannot exist when the depth goes to zero ($s = 1$) and hence system energy becomes unbounded. This countered the claim in [22] that modes do not exist because of the cone vertex when in fact it is directly a result of the depth going to zero on some part of the container boundary.

In Chapter 4 we introduced viscosity into the half cone system and observed topographic waves hitting the south-western wall and dissipating very quickly, much faster than the rectangular geometry. We were able to calculate the vertical vorticity (ζ) and reproduce its evolution over time, confirming that initial positive vorticity is generated, it propagates west and then dissipates in the south-west corner just as in [22]. The vertical velocity results were also confirmed and reproduced. Finally we used the energy decay methodology from [22] to show that the half cone spin-down concluded 4.13 times faster than the half cylinder case and 3.43 time faster in the $s = 1$ rectangular container compared to the $s = 1/2$. Again this demonstrates that the change in geometry is not as influential as a steeper topography when calculating energy decay.

In summary we have managed to accurately reproduce the fundamental dynamics generated by a spin-down process in [22] using well studied existing theory. The dynamics have also been studied to a certain extent in the half cylinder and rectangular geometries. We managed to reduce the governing equations to a generalised linear eigenvalue problem (for modal solutions) and a system of linear ODEs (for time-dependent solutions). Instead of needing high performance computing to solve the fully non-linear Navier-Stokes equations we were able to utilise the spectral method detailed in [21] to reduce computational requirements. We confirmed that the full three-dimensional simulations and experimental results in [22] can in fact be reproduced using the shallow water assumptions with minimal computational effort.

It was also noted that the linear spin-down analysis is easily adapted for spin-up motion by simply reversing the sign ($+1$ to -1) of the initial vorticity in condition (2.7.1). The resulting dynamics would be identical to the spin-down case except that the streamfunctions, velocity vectors and vertical vorticity would have opposite signs. This is also verified in [22] when Li et al. conclude that the dynamics are identical (i.e. "$\boldsymbol{u}(\boldsymbol{r}, t, -Ro) = -\boldsymbol{u}(\boldsymbol{r}, t, Ro)$") in the small linear spin-up/down limit $|Ro| \leq 0.05$.

Li et al. state that the reason for not being able to discern any discrete set of modes in their findings is because the fluid is evolving in the half cone geometry. We have demonstrated that it has nothing to do with the geometry because we discovered that oscillatory modes do in fact exist in the $s = 1/2$ case. The same occurs in the rectangular container and hence it has everything to do with the fact that in the limit of $s \to 1$, the depth goes to zero at some point and hence the energy of the system becomes unbounded. This means that no discernable set of modes can be located in order to capture all of this infinite energy.

5.1 Further Work

Possible extensions to this work include studying the impact of fluid stratification and compressibility on the system dynamics. This methodology could also be used to study other interesting geometries (in the shallow water limit) with varying topographies in the linear spin-up/down cases. Even more challenging would be to include try and incorporate 'spin-over' dynamics where the direction of rotation of the container is reversed instead of altered at $t = 0^+$.

Appendix A

Orthogonality of Inviscid Eigenmodes

In [19], Johnson showed, using energy conservation relations, that the normal modes of the inviscid TWE are orthogonal and have real subinertial eigenfrequencies. We lay out Johnson's argument in detail, with only minor adaptations, beginning with the TWE (2.3.1):

$$\nabla \cdot \left(\frac{\nabla \psi_t}{H_0}\right) + \hat{\mathbf{z}} \cdot (\nabla \psi \times \nabla \frac{1}{H_0}) = 0, \tag{A.0.1}$$

or in the divergence-free form

$$\nabla \cdot \Big[\frac{\nabla \psi_t}{H_0} - \psi \underbrace{(\hat{\mathbf{z}} \times \nabla \frac{1}{H_0})}_{=:\mathbf{K}}\Big] = 0. \tag{A.0.2}$$

Start by multiplying the divergence-free form by ψ

$$\psi \nabla \cdot \Big[\frac{\nabla \psi_t}{H_0} - \psi \mathbf{K}\Big] = 0. \tag{A.0.3}$$

Using the product rule and flipping the signs we obtain

$$- \nabla \cdot \psi \Big[\frac{\nabla \psi_t}{H_0} - \psi \mathbf{K}\Big] + \nabla \psi \cdot \Big[\frac{\nabla \psi_t}{H_0} - \psi \mathbf{K}\Big] = 0. \tag{A.0.4}$$

Expanding and using the product rule again we obtain

$$\nabla\psi\cdot\Big(\frac{\nabla\psi_t}{H_0}\Big)+\nabla\cdot\Big(-\psi\frac{\nabla\psi_t}{H_0}\Big)+\nabla\cdot(\psi^2\mathbf{K})-\nabla\psi\cdot(\psi\mathbf{K})=0, \tag{A.0.5}$$

$$\nabla\psi\cdot\Big(\frac{\nabla\psi_t}{H_0}\Big)+\nabla\cdot\Big(-\psi\frac{\nabla\psi_t}{H_0}\Big)+\psi\nabla\psi\cdot\mathbf{K}=0 \tag{A.0.6}$$

$$\nabla\psi\cdot\Big(\frac{\nabla\psi_t}{H_0}\Big)+\nabla\cdot\Big(-\psi\frac{\nabla\psi_t}{H_0}+\frac{1}{2}\psi^2\mathbf{K}\Big)=0, \tag{A.0.7}$$

Finally we obtain

$$\frac{\partial}{\partial t}\underbrace{\frac{1}{2}\Big(\frac{|\nabla\psi|^2}{H_0}\Big)}_{E}+\nabla\cdot\underbrace{\Big(-\psi\frac{\nabla\psi_t}{H_0}+\frac{1}{2}\psi^2\mathbf{K}\Big)}_{\mathbf{F}}=0, \tag{A.0.8}$$

$$\frac{\partial E}{\partial t}+\nabla\cdot\mathbf{F}=0, \tag{A.0.9}$$

where E represents the vertically integrated local kinetic energy density and $\mathbf{F}$ the energy flux. Energy is conserved where $\mathbf{F}\cdot\hat{\mathbf{n}}=0$ on the boundary and we know the normal modes take the form $\psi=\phi(x,y)e^{i\omega t}$ with $\psi=0$ on ∂V of some small bounded domain V. Define an inner product on V as

$$\langle\phi_0,\phi_1\rangle=\int_V\frac{1}{H_0}\nabla\phi_0\cdot\nabla\phi_1^*\,dV \tag{A.0.10}$$

where ϕ^* is the complex conjugate of ϕ. The energy norm can then be defined as $E(\phi):=\langle\phi,\phi\rangle$. Now sub ψ into (A.0.2), multiply by ϕ^* and integrate over V

$$\int_V\phi^*\nabla\cdot\Big[\frac{\nabla\psi_t}{H_0}-\psi\mathbf{K}\Big]\,dV=0, \tag{A.0.11}$$

$$\int_V\phi^*\nabla\cdot\Big[i\omega\frac{\nabla\psi}{H_0}-\psi\mathbf{K}\Big]\,dV=0, \tag{A.0.12}$$

$$\omega\int_V\phi^*\nabla\cdot(\frac{\nabla\phi}{H_0})+i\int_V\phi^*\nabla\cdot(\phi\mathbf{K})\,dV=0. \tag{A.0.13}$$

Using the product rule, divergence theorem and boundary condition

$$-\omega\int_V\frac{1}{H_0}\nabla\phi^*\cdot\nabla\phi+i\int_V\phi^*\nabla\cdot(\phi\mathbf{K})\,dV=0, \tag{A.0.14}$$

$$\omega E(\phi)-i\int_V\phi^*\nabla\cdot(\phi\mathbf{K})\,dV=0. \tag{A.0.15}$$

Similarly for ω^*

$$\omega^* E(\phi) + i \int_V \phi \nabla \cdot (\phi^* \mathbf{K}) \; dV = 0. \tag{A.0.16}$$

Subtracting (A.0.15) from (A.0.16) we obtain

$$\begin{aligned}(\omega - \omega *) E(\phi) &= i \int_V \phi \nabla \cdot (\phi^* \mathbf{K}) + \phi^* \nabla \cdot (\phi \mathbf{K}) \; dV \\ &= i \int_V \nabla \cdot (\phi \phi^* \mathbf{K}) \; dV = i \int_{\partial V} \phi \phi^* \mathbf{K} \cdot \hat{\mathbf{n}} dS = 0, \end{aligned} \tag{A.0.17}$$

by divergence theorem and the boundary condition again. By the definition of the energy norm we know that $E(\phi) = 0 \iff \phi = 0$, so for non-trivial ϕ, $\omega = \omega^*$. This means the eigenvalues must be real for any modes that exist in V. Adding (A.0.15) and (A.0.16) instead, we obtain

$$\omega E(\phi) = \frac{i}{2} \int_V \phi^* \nabla \cdot (\phi \mathbf{K}) - \phi \nabla \cdot (\phi^* \mathbf{K}) \; dV, \tag{A.0.18}$$

$$= i \int_V \phi^* \nabla \cdot (\phi \mathbf{K}), \tag{A.0.19}$$

$$= i \int_V \phi^* \nabla \phi \cdot \mathbf{K} =: F(\phi), \tag{A.0.20}$$

recalling that $\nabla \cdot \mathbf{K} = 0$. Using some simple vector calculus rules,

$$F(\phi) = i \int_V \phi \nabla \phi^* \cdot \mathbf{K} = i \int_V \frac{1}{H_0} \hat{\mathbf{z}} \cdot (\nabla \phi^* \times \nabla \phi) dV. \tag{A.0.21}$$

This means we can now bound $F(\phi)$ in the following way

$$|F| = \Big| \int_V \frac{1}{H_0} \hat{\mathbf{z}} \cdot (\nabla \phi^* \times \nabla \phi) dV \Big| \le |1| \cdot \Big| \int_V \frac{1}{H_0} |\nabla \phi|^2 dV \Big| = |E|, \tag{A.0.22}$$

$$\Rightarrow \quad |\omega E(\phi)| = |F| \le |E| \quad \Rightarrow \quad |\omega| \le 1. \tag{A.0.23}$$

Having demonstrated the eigenvalues are real and subinertial, we now recall (A.0.17) to show that distinct eigenvalues ω_m and ω_n (with their respective eigenfunctions ϕ_n and ϕ_m) can be written

$$(\omega_n - \omega_m)\langle \phi_n, \phi_m \rangle = 0, \tag{A.0.24}$$

meaning distinct eigenfunctions ($m \neq n$) are orthogonal to one another. We can then superpose $\bar{N}$ eigenmodes as

$$\psi = \sum_{n=1}^{\bar{N}} a_n \phi_n(x, y) e^{i\omega_n t}, \tag{A.0.25}$$

where a_n are some coefficients to be found [5, p.66]. Taking the inner product of ψ with ϕ_m for some m,

$$\langle \psi, \phi_m \rangle = \sum_{n=1}^{\bar{N}} a_n e^{i\omega_n t} \langle \phi_n, \phi_m \rangle, \tag{A.0.26}$$

where all terms on the RHS are zero unless $m = n$ which implies

$$\langle \psi, \phi_m \rangle = a_m \langle \phi_m, \phi_m \rangle \quad \Rightarrow \quad a_m = \frac{\langle \psi, \phi_m \rangle}{\langle \phi_m, \phi_m \rangle}. \tag{A.0.27}$$

This allows us to write the superposed solution of eigenmodes as

$$\psi = \sum_{n=1}^{\bar{N}} a_n \phi_n(x, y) e^{i\omega_n t} \quad \text{where} \quad a_n = \frac{\langle \psi, \phi_n \rangle}{\langle \phi_n, \phi_n \rangle}. \tag{A.0.28}$$

Appendix B

MATLAB Code

B.1 cheb.m

```
function [D,x] = cheb(N)
%Calculates the first Chebyshev derivative matrix for N+1 collocation
% points and the collocation vector x. Original code produced by
% L.Trefethen, located at:
%  https://people.maths.ox.ac.uk/trefethen/spectral.html

%Inputs:
% N = discretise [-1,1] into N+1 Chebyshev points.

%Outputs:
% D  = first Chebyshev derivative matrix, dimensions (N+1)x(N+1).
% x  = vector of Chebyshev collocation points, dimension (N+1)x1.

if N==0, D=0; x=1; return, end
x = cos(pi*(0:N)/N)';                   % vector of Chebyshev points.
c = [2; ones(N-1,1); 2].*(-1).^(0:N)';
X = repmat(x,1,N+1);
dX = X-X';
D  = (c*(1./c)')./(dX+(eye(N+1)));     % off-diagonal entries.
D  = D - diag(sum(D'));                 % diagonal entries.
end
```

B.2 inviscid_half_cone.m

```
%Solves the half cone eigenvalue problem in [0,pi]x[0,1] by using the
```

```
% QZ algorithm in the eig function.

%Inputs:
% M = discretise [-1,1] into N+1 Chebyshev points in horizontal direction.
% N = discretise [-1,1] into M+1 Chebyshev points in vertical direction.
% s = slope of linear depth profile in [0,1].

%Outputs:
% V = matrix whose columns contain eigenvectors/modes of the problem.
% E = column vector of the corresponding eigenvalues.
% I = ordering indices of the sorted (descending) eigenvalues in E.
% T = angular Chebyshev coordinate interval [0,pi].
% R = radial Chebyshev coordinate interval [0,1].

function [V,E,I,T,R] = inviscid_half_cone(M,N,s)

%Calculate the Chebyshev differentiation matrices and the vectors of
% collocation points using cheb.m.
[Dt,t] = cheb(M); %angular matrix
[Dr,r] = cheb(N); %radial matrix

%Rescale the variables for the polar domain [0,pi]x[0,1].
t_min = 0;   t_max = pi;
Dt = 2/(t_max-t_min)*Dt;                          %scale the Chebyshev matrix
Dtt = Dt^2;                                       %second derivative matrix
T = (1/2)*( (t_max-t_min)*t + (t_min + t_max) ); %scale the interval
T = T(2:end-1);                                   %enact boundary condtions

r_min = 0;   r_max = 1;
Dr = 2/(r_max-r_min)*Dr;                          %scale the Chebyshev matrix
Drr = Dr^2;                                       %second derivative matrix
R = (1/2)*( (r_max - r_min)*r + (r_min + r_max) );  %scale the interval
R = R(2:end-1);                                   %enact boundary condtions

%Define the topography H(r).
H   = 1 - s*R;
H_r = -s*ones(length(R),1);  %Derivative of the function

%Define identity matrices for the Kronecker products.
Im = eye(M-1);   In = eye(N-1);
```

```
%Enact BCs on the differentiation matrices by removing edge rows and
% columns.
Dt  = Dt(2:end-1,2:end-1);     Dtt = Dtt(2:end-1,2:end-1);
Dr  = Dr(2:end-1,2:end-1);     Drr = Drr(2:end-1,2:end-1);

%Calculate the non-constant coefficient values at each radial
% collocation point then diagonalise.
diag_r   =  diag(R);    diag_r2  =  diag(R.^2);
diag_H   =  diag(H);    diag_H_r =  diag(H_r);

%Calculate the linear operator matrices using Kronecker products.
A = kron(1i*diag_r*diag_H_r,Dt);
B = kron(diag_r2*diag_H*Drr,Im) + kron(diag_r*diag_H*Dr,Im) - ...
    kron(diag_r2*diag_H_r*Dr,Im) + kron(diag_H,Dtt);

%Solve the eigenvalue problem.
% 'qz' tells eig to use the QZ algorithm.
% 'vector' tells eig to output the eigenvalues in a vector, not a matrix.
[V,E] = eig(A,B,'qz','vector');

%Sort eigenvalues into descending order.
[EE,I] = sort( E , 'descend' );
end
```

B.3 spurious_eigenvalues.m

```
%Filters the 'good' eigenvalues from the 'bad' using the method suggested
% by Boyd and Johnson. Need to have saved inviscid_half_cone.m workspaces
% beforehand.

clear;  close
disp('Locating good eigenvalues...');

%Choose a low (M1,N1), high resolution (M2,N2).
M1 = 70;  N1 = 70;
M2 = 75;  N2 = 75;

%Load the two resolutions and sort the e'values into decreasing order.
```

```
load('M=70_inviscid_half_cone_s=05.mat')
V1 = V; E1 = E; R1 = R; T1 = T;       [EE1,I1] = sort(E1,'descend');
load('M=75_inviscid_half_cone_s=05.mat')
V2 = V; E2 = E; R2 = R; T2 = T;       [EE2,I2] = sort(E2,'descend');

% load('M=70_inviscid_half_cone_s=1.mat')
% V1 = V; E1 = E; R1 = R; T1 = T;       [EE1,I1] = sort(E1,'descend');
% load('M=75_inviscid_half_cone_s=1.mat')
% V2 = V; E2 = E; R2 = R; T2 = T;       [EE2,I2] = sort(E2,'descend');

NE = length(EE1)-1;  %number of modes to compare.
sigma = zeros(NE,1); %spacing between low resolution e'values.
I = zeros(NE,1);     %index where closest e'values in high res list are.
d = zeros(NE,1);     %nearest differences between high and low resolutions.

%Matrix to store difference between each low res and high res e'values.
temp = zeros(NE,NE);
%Used to store the minimum value of each row of temp.
diff = zeros(NE,1);

%Calculate the spacing between e'values of the low resolution.
sigma(1) = abs(EE1(1) - EE1(2));
for i = 2:NE
    sigma(i) = 0.5*(abs(EE1(i) - EE1(i-1)) + abs(EE1(i+1) - EE1(i)));
end

%Calculate minimum difference between each low res and each high res
% e'value ready for scaling by sigma.
for i = 1:NE
    for j = 1:NE
        temp(i,j) = abs( EE1(i) - EE2(j) );
    end
     %Find the minimum value in each row and its index.
    [diff(i),I(i)] = min(temp(i,:));
end

%Finally calculate the delta_nearest for each e'value.
for i = 1:NE
        d(i) = diff(i) / min( [abs(EE1(i)),sigma(i)] );
end
```

```
%Plot the reciprocal of delta on a logarithmic scale against mode number.
plot(1:NE,log(1./d),'ok')
xlabel('n')
ylabel('log(1/\delta_{n,nearest})')
axis([0,400,0,35])
```

B.4 mode_coefficients.m

```
%This script calulates the coefficients for each mode specified in K by
% integrating over the domain D (at the chosen resolution). Enter inputs
% and run the script to obtain the vector of coefficients.

clear; close

%Load the solution.
load('M=70_inviscid_half_cone_s=05.mat')

%Inputs:
M = 70;          %M+1 radial points
N = 70;          %N+1 angular points
s = 0.5;         %slope of topography
K = (1:88);       %modes to calcluate coefficients for

%Define terms for the inner product.
R = [1;R];      %Need to add first value back to start of R
H = 1 - s*R;    %Define the topography H(r).

%Scaled differentiation matrices with BCs enacted on them.
[Dt,~] = cheb(M); Dt = (2/pi)*Dt; Dt = Dt(1:M,1:M); %Angular direction
[Dr,~] = cheb(N); Dr = 2*Dr;      Dr = Dr(1:N,1:N); %Radial direction

%Kronecker product differentiation matrices.
Dt = kron(eye(N),Dt);    Dr = kron(Dr,eye(M));

%Calculate the numerators (integral of the mode phi).
numerators = zeros(length(K),1);   %Solution vector

for i = K
    %Build the solution set.
```

```
    U = zeros(M+1,N+1);
    U(2:M,2:N) = reshape(real(V(:,I(i))),M-1,N-1);
    U = U(1:M,1:N);    %removes end row/column as all have value phi = 0.
    phi = U(:);        %back in vector form

    I1 = Dt\phi;      %integrate over theta
    I2 = Dr\I1;       %integrate over r.
    numerators(i) = sum(I2); %Sum contributions to obtain full integral.
end

%Calculate the denominators (the inner product).
denominators = zeros(length(K),1);

for i = K
    %Build the solution set.
    U = zeros(M+1,N+1);
    U(2:M,2:N) = reshape(real(V(:,I(i))),M-1,N-1);
    U = U(1:M,1:N);    %removes end row/column as all have value phi = 0.
    phi = U(:);        %back in vector form

    inner_product = kron(diag(1./H),eye(M))*( ((Dr*phi).^2) +...
        kron(diag(1./(R.^2)),eye(M))*((Dt*phi).^2) );

    I1 = Dt\inner_product; %integrate over theta
    I2 = Dr\I1;            %inegrate over r
    denominators(i) = sum(I2); %sum contributions to obtain full integral.
end

coeffs = -numerators./denominators;  %final coefficient vector
```

B.5 time_dependent_inviscid_half_cone.m

```
%This code solves the time-dependent TWE problem in the half cone domain.
% Enter inputs and run the script.

clear;  close

%Inputs:
M = 70;          %no. collocation points in theta
N = 70;          %no. collocation points in r
```

```
s = 0.5;           %slope of topography
time_vector = (0:1:2500); %integrate the equation over t = [0,t_final]

%Calculate the matrices/vectors for the spectral method.
[Dt,t] = cheb(M); %theta-direction matrix
[Dr,r] = cheb(N); %r-direction matrix

%Rescale variables for the domain [0,pi]x[0,1].
t_min = 0;   t_max = pi;
Dt = 2/(t_max-t_min)*Dt;                              %scale the Chebyshev matrix
Dtt = Dt^2;                                           %second derivative matrix
T = (1/2)*( (t_max-t_min)*t + (t_min + t_max) ); %scale the interval
T = T(2:end-1);                                       %enact boundary condtions

r_min = 0;   r_max = 1;
Dr = 2/(r_max-r_min)*Dr;                              %scale the Chebyshev matrix
Drr = Dr^2;                                           %second derivative matrix
R = (1/2)*( (r_max - r_min)*r + (r_min + r_max) );  %scale the interval
R = R(2:end-1);                                       %enact boundary condtions

%Define the topography H(r).
H = 1 - s*R;                    %Linearly sloping in r
H_r = -s*ones(length(R),1);  %Derivative of the topography function

%Define identity matrices for the Kronecker products.
Im = eye(M-1);    In = eye(N-1);

%Enact BCs on the differentiation matrices by removing edge rows and columns.
Dt = Dt(2:end-1,2:end-1);     Dtt = Dtt(2:end-1,2:end-1);
Dr = Dr(2:end-1,2:end-1);     Drr = Drr(2:end-1,2:end-1);

%Calculate the non-constant coefficient values at each collocation point
% in r, then diagonalise with Kronecker.
diag_r   =  diag(R);                diag_r2   =  diag(R.^2);
diag_inv_r   =  diag(1./R);         diag_inv_r2   =  diag(1./(R.^2));
diag_H   =  diag(H);                diag_inv_H   =  diag(1./H);
diag_inv_H2   =  diag(1./(H.^2));  diag_H_r =  diag(H_r);

%Linear matrix operators for the TWE.
A = kron(diag_r2*diag_H*Drr,Im) + kron(diag_r*diag_H*Dr,Im) -...
```

```
    kron(diag_r2*diag_H_r*Dr,Im) + kron(diag_H,Dtt);
B = kron(diag_r*diag_H_r,Dt);

C = -inv(A)*B; %calculate linear operator to solve du/dt = C*u

%Initial condition calculation
initial_cond = ones( (M-1)*(N-1),1 ); %positive vorticity (spin-down)

D = kron(diag_inv_H*Drr,Im) + kron(diag_inv_r*diag_inv_H*Dr,Im)...
    - kron(diag_H_r*diag_inv_H2*Dr,Im) + ...
    kron(diag_inv_r2*diag_inv_H,Dtt); %linear operator for the IC

psi_0 = D\initial_cond; %the initial condition vector of streamline pattern

%Finally solve the problem using MATLAB's standard ODE solver.
lin_operator_wrapper = @(t,y) lin_operator(t,y,C);

   %Use ode45 for s = 1/2 as it is non-stiff.
[times,psi] = ode45(lin_operator_wrapper,time_vector,psi_0); psi = psi';
   %Use ode15s for s = 1 as it is stiff.
%[times,psi] = ode15s(lin_operator_wrapper,time_vector,psi_0); psi = psi';

%% lin_operator.m
%This function formulates the linear system of ODEs to be solved by
% ode45.

%Inputs:
% t = not used.
% u = vector of unknowns.
% C = linear matrix operator.

function [dudt] = lin_operator(t,u,C)
dudt = C*u;
end
```

B.6 vertical_vorticity.m

```
%Calculation of the vertical viscosity of the time-dependent solution. Load
%the required solution then run.
```

```
clear; close

%Load required solution
load('M=70_viscous_time_dep_sol_s=1_v=0001.mat')

%Define the solution matrix.
vert_vorticity = psi;

%Matrix operator to obtain vertical vorticity.
L = kron(diag_inv_H*Drr,Im) + kron(diag_inv_r*diag_inv_H*Dr,Im) -...
    kron(diag_H_r*diag_inv_H2*Dr,Im) + kron(diag_inv_r2*diag_inv_H,Dtt);

for i = 1:length(psi(1,:))
    vert_vorticity(:,i) = L*psi(:,i);
end

save('M=70_viscous_time_dep_sol_s=1_v=0001.mat')
```

B.7 energy_decay.m

```
%Code to calculate the total energy of the solution at each time step.
%Load a solution and run for a the time points in K.

clear; close

%Load solution
load('M=70_viscous_time_dep_sol_s=1_v=0001.mat')

%Inputs:
M = 70;         %M+1 radial points
N = 70;         %N+1 angular points
K = (1:length(psi(1,:)));   %time steps to calcluate energy for

%Differentiation matrices with BCs enacted on them.
[Dt,~] = cheb(M); Dt = (2/pi)*Dt; Dt = Dt(1:M,1:M); %Angular direction
[Dr,~] = cheb(N); Dr = 2*Dr;      Dr = Dr(1:N,1:N); %Radial direction

%Kronecker products
Dt = kron(eye(N),Dt);   Dr = kron(Dr,eye(M));
```

```
energy = zeros(length(K),1);
for i = K
%multiply the two vectors to be integrated.
integral = psi(:,i).*vert_vorticity(:,i);

%Enact the boundary condition.
U = zeros(M+1,N+1);
U(2:M,2:N) = reshape(integral,M-1,N-1);
U = U(1:M,1:N);    %Removes end row/column as all have value phi = 0.
integral = U(:); %back in vector form

I1 = Dt\integral; %integrate in the angular direction.
I2 = Dr\I1;       %inegrate in the radial direction.
energy(i) = -sum(I2);  %sum contributions to obtain full integral.
end

save('M=70_s=1_v=0001_energy.mat','energy')
```

Bibliography

[1] G. Amberg and M. Ungarish. Spin-up from rest of a mixture: Numerical simulation and asymptotic theory. *Journal of Fluid Mechanics*, 246:443–464, 1993.

[2] D.L.T. Anderson and A.E. Gill. Spin-up of a stratified ocean, with applications to upwelling. *Deep Sea Research and Oceanographic Abstracts*, 22(9):583–596, 1975.

[3] E. R. Benton and A. Clark. Spin-Up. *Annual Review of Fluid Mechanics*, 6(1):257–280, 1974.

[4] H. Bondi and R. A. Lyttleton. On the dynamical theory of the rotation of the earth. *Mathematical Proceedings of the Cambridge Philosophical Society*, 44(3):345–359, 1948.

[5] J. P. Boyd. *Chebyshev and Fourier Spectral Methods*. Courier Corporation, second edition, 2001.

[6] G. H. Bryan. The Waves on a Rotating Liquid Spheroid of Finite Ellipticity. *Philosophical Transactions of the Royal Society A: Mathematical, Physical and Engineering Sciences*, 180(0):187–219, 1889.

[7] F. Burmann and J. Noir. Effects of bottom topography on the spin-up in a cylinder. *Physics of Fluids*, 30(10):106601, 2018.

[8] C. Canuto, M. Y. Hussaini, A. Quarteroni, and T. A. Zang. *Spectral Methods in Fluid Dynamics*. Springer Verlag, Berlin, Heidelberg, 1988.

[9] P. W. Duck and M. R. Foster. Spin-up of homogeneous and stratified fluids. *Annual Review of Fluid Mechanics*, 33(1):231–263, 2001.

[10] VW Ekman. On the influence of the earth's rotation on ocean-currents. *Arkiv for Matematik, Astronomi och Fysik*, 2(11), 1905.

[11] A.E. Gill. *Atmosphere-Ocean Dynamics*. Academic Press, London, 1982.

[12] D. Gottlieb and S. A. Orszag. *Numerical Analysis of Spectral Methods*. Society for Industrial and Applied Mathematics, 1977.

[13] H.P. Greenspan. *The Theory of Rotating Fluids*. Cambridge U.P, 1968.

[14] H.P. Greenspan and L.N. Howard. On a time-dependent motion of a rotating fluid. *Journal of Fluid Mechanics*, 17(3):385–404, 1963.

[15] G. J. F. Van Heijst. Spin-up phenomena in non-axisymmetric containers. *Journal of Fluid Mechanics*, 206:171–191, 1989.

[16] G. J. F. Van Heijst, L. R. M. Maas, and C. W. M. Williams. The spin-up of fluid in a rectangular container with sloping bottom. *Journal of Fluid Mechanics*, 265:125–159, 1994.

[17] R.A. Horn and C.R. Johnson. Matrix equations and the Kronecker product. In *Topics in Matrix Analysis*, chapter Four, pages 239–297. Cambridge University Press, Cambridge, 1991.

[18] K. Hutter, Y. Wang, and I.P. Chubarenko. *Physics of Lakes. Volume 2: Lakes as Oscillators*. Springer, 2011.

[19] E. R. Johnson. Topographic waves in open domains. Part 1. Boundary conditions and frequency estimates. *Journal of Fluid Mechanics*, 200(-1):69, 1989.

[20] E. R. Johnson. Unpublished lecture notes. Geophysical Fluid Dynamics - University College London, 2019.

[21] E. R. Johnson and J. T. Rodney. Spectral methods for coastal-trapped waves. *Continental Shelf Research*, 31(14):1481–1489, 2011.

[22] L. Li, M. D. Patterson, K. Zhang, and R. R. Kerswell. Spin-up and spin-down in a half cone: A pathological situation or not? *Physics of Fluids*, 24(11):116601, 2012.

[23] W. H. Munk. On the Wind-Driven Ocean Circulation. *Journal of Meteorology*, 7(2):80–93, 1950.

[24] J.S. Park and J.M. Hyun. Review on open-problems of spin-up flow of an incompressible fluid. *Journal of Mechanical Science and Technology*, 22(4):780–787, 2008.

[25] J. Pedlosky and H. P. Greenspan. A simple laboratory model for the oceanic circulation. *Journal of Fluid Mechanics*, 27(2):291–304, 1967.

[26] C.-G. Rossby. Dynamics of steady ocean currents in the light of experimental fluid mechanics. V(I), 1936.

[27] T. Stocker and K. Hutter. *Topographic Waves in Channels and Lakes on the f-Plane*. Springer-Verlag, New York, 1987.

[28] H. Stommel. The westward intensification of wind-driven ocean currents. *Transactions, American Geophysical Union*, 29(2):202, 1948.

[29] L.N. Trefethen. *Spectral Methods in MATLAB*. SIAM, Philadelphia, 2000.

[30] J. A. van de Konijnenberg, H. I. Andersson, J. T. Billdal, and G.J.F. van Heijst. Spin-up in a rectangular tank with low angular velocity. *Physics of Fluids*, 6(3):1168–1176, 1994.

[31] J. A. van de Konijnenberg and G. J. F. van Heijst. Spin-up in a rectangular tank with a discontinuous topography. *Physics of Fluids*, 8(11):2943–2952, 1996.

[32] J. A. van de Konijnenberg and G.J.F. van Heijst. Nonlinear spin-up in a circular cylinder. *Physics of Fluids*, 7(12):2989–2999, 1995.

[33] J. A. van de Konijnenberg, T. L. Wessels, and G.J.F. van Heijst. Spin-up in a circular tank with a radial barrier. *Physics of Fluids*, 8(8):2048–2059, 1996.

[34] G. J.F. van Heijst, P. A. Davies, and R. G. Davis. Spin-up in a rectangular container. *Physics of Fluids A*, 2(2):150–159, 1990.

[35] W. B. Watkins and R. G. Hussey. Spin-up from rest in a cylinder. *Physics of Fluids*, 20(10):1596–1604, 1977.

[36] E. H. Wedemeyer. The unsteady flow within a spinning cylinder. *Journal of Fluid Mechanics*, 20(3):383–399, 1964.

[37] P. D. Weidman. On the spin-up and spin-down of a rotating fluid. Part 1. Extending the Wedemeyer model. *Journal of Fluid Mechanics*, 77(04):685, 1976.

[38] C. S. Yogananda and A Einstein. The cause of the formation of meanders in the courses of rivers and of the so-called Baer's law. *Resonance*, 5(3):105–108, 2000.

[39] K. Zhang, P. Earnshaw, X. Liao, and F. H. Busse. On inertial waves in a rotating fluid sphere. *Journal of Fluid Mechanics*, 437:103–119, 2001.

[40] K. Zhang, X. Liao, and P. Earnshaw. On inertial waves and oscillations in a rapidly rotating spheroid. *Journal of Fluid Mechanics*, 504:1–40, 2004.